LEAST-SQUARES AND OTHER RESIDUAL BASED TECHNIQUES FOR RADIATION TRANSPORT CALCULATIONS

A Dissertation

by

WEIXIONG ZHENG

Submitted to the Office of Graduate and Professional Studies of
Texas A&M University
in partial fulfillment of the requirements for the degree of

DOCTOR OF PHILOSOPHY

Chair of Committee,	Ryan G. McClarren
Committee Members,	Jim E. Morel
	Marvin L. Adams
	Jean-Luc Guermond
Head of Department,	Yassin Hassan

December 2016

Major Subject: Nuclear Engineering

ABSTRACT

In this dissertation, we develop several novel methods based on or related to least-squares transport residual for solving deterministic radiation transport problems. For the first part of this dissertation a nonlinear spherical harmonics (P_N) closure (TP_N) was developed based on analysis of the least-squares residual for time-dependent P_N equations in 1D slab geometry. The TP_N closure suppresses the oscillations induced by Gibbs phenomenon in time-dependent transport calculations effectively. Simultaneously, a nonlinear viscosity term based on the spatial and temporal variations is realized and used in the extension to filtered P_N method (NFP_N). NFP_N determines the angular viscosity on the fly and potentially fixed the issue existed in linear FP_N that filtering strength needs to be predefined by iteratively solving the problem. We further developed another type of NFP_N and demonstrate both of the two NFP_N preserve the thick diffusion limit for thermal radiative transfer problems theoretically and numerically.

We also developed several novel methods along with error analyses for steady-state neutron transport calculations based on least-squares methods. Firstly, a relaxed L_1 finite element method was developed based on nonlinearly weighting the least-squares formulation by the pointwise transport residual. In problems such as void and near-void situations where least-squares accuracy is poor, the L_1 method improves the solution. Further, a non-converged RL_1 still can present comparable accuracy. We then developed a least-squares method based on a novel contiguous-discontinuous functional. A proof is provided for the conservation preservation for such a method, which is significant for problems such as k-eigenvalue calculations. Also, a second order accuracy is observed with much lower error magnitudes in several quantities of interest for heterogeneous problems compared with self-adjoint angular flux (SAAF) solution. Lastly, we extended the CD methodology

with $1/\sigma_{\mathrm{t}}$-weighted least-squares functional to derive a CD-SAAF method and developed a S_N-P_N angular hybrid scheme. The hybrid scheme can employ high order S_N in regions with strong transport feature to couple with low order P_N in regions with diffusive flux. In k-eigenvalue calculations, it shows superb accuracy with low degrees of freedom.

DEDICATION

To my family.

ACKNOWLEDGMENTS

I would like to thank my adviser, Dr Ryan G. McClarren, for his guidance and tremendous amount of support. I would also like to thank my committee members, Dr. Morel, Dr. Adams and Dr. Guermond, for the helps on discussing the theoretical aspects of the work in this dissertation.

Appreciation also goes to my friends and colleagues, such as Dr. Yunhuang Zhang, Vincent Laboure, James Tompkins, Simon Bolding and Daniel Holladay, for making my life at Texas A&M a wonderful experience. I would specially thank Hans Hammer and Jacob Landman for running codes and friendship.

I would also like to thank Dr. Wolfgang Bangerth from State University of Colorado and Dr. Bruno Turkins from Oak Ridge National Laboratory (ORNL) for invaluable discussions on deal.II implementation; Dr. Cory Hauck from ORNL for the visiting chance with learning a lot of mathematical sides for my research; and of course Dr. Yaqi Wang from Idaho National Laboratory (INL) for the precious internship chance and allowing me to introduce bugs to Rattlesnake.

Finally, I would thank my mother, my grandmother and my sister for their encouragement and my wife for her love.

TABLE OF CONTENTS

Page

LIST OF FIGURES

FIGURE Page

LIST OF TABLES

TABLE Page

1. INTRODUCTION

The dissertation is mainly composed of works on two topics in radiation transport calculations. The first topic is about a spherical-harmonics-based angular discretization method for solving the time-dependent transport equation and thermal photon transport problems coupled with material heating. The second topic regards solving the steady state neutron transport equation based on least-squares or related finite elements methods.

For the first half of this dissertation, we will introduce an angular viscosity for the spherical harmonics method for solving time-dependent radiation transport and thermal radiative transfer problems inspired by the least-squares transport residual. The second half of this dissertation is the application of innovations based on the least-squares residual of finite element methods for solving steady-state neutron transport equation.

Specifically, this dissertation will present discoveries in the following aspects of radiation transport:

- A nonlinear P_N closure in general dimension implied by least-squares transport residual in moment variable space
- The first two nonlinear filtered P_N formulations for time-dependent linear transport and thermal radiative transfer
- A proof for asymptotic preservation of the filtering methods
- A fully implicit solving procedure for the filtered spherical harmonics
- A relaxed L_1 finite element method for solving steady-state neutron transport problems
- A nonlinear weak boundary condition compatible with L_1 finite element method

- A contiguous-discontinuous least-squares (CDLS) finite element solving neutron transport
- A proof of conservation preservation for CDLS
- A contiguous-discontinuous self-adjoint angular flux (CD-SAAF) differencing scheme for solving neutronics problems
- A multi-angular coupling scheme based on CD-SAAF

1.1 Deterministic Radiation Transport Methods

There are two common approaches to solving radiation transport problems. Stochastic or Monte Carlo methods compute the transport of particles with a classical statistical procedure that samples particle paths that are consistent with the physics. Particles move continuously in angle. On the other hand, one can employ deterministic methods which solve the transport equation, a partial differential equation (PDE) defined in seven-dimensional phase space. In such a case, discretization is necessary for all dimensions in the phase space. In the work of this dissertation, we restrict ourselves to the deterministic method.

As one of the best known deterministic methods, discrete ordinates method (S_N) has been actively heavily studied in the past decades for discretization and efficient solving. In essence, S_N relies on solving the transport equation in specific directions given by angular quadrature and coupling the separated directional information by the scattering process. However, it has issues when the radiation field possess strong anisotropy and little scattering. Therein, particle information transmits dominantly in directions defined in the quadrature causing the flux oscillations in angle. As a consequence, the radiation field behaves as ray-like distributions in space[1] and thusly it is called “ray-effects". Increasing number of directions would not necessarily effectively damp the ray-effects, which also attracts people to develop mitigation techniques to alleviate the solution[2, 3].

On the other hand, expanding the angular flux with the truncated spherical harmonics functions constitutes the spherical harmonics (P_N) method. As the spherical harmonics preserves rotational invariance, it is free from the curse of ray-effects. Also, as a spectral finite element in angle, it possess the exponential angular convergence when the flux is smooth in angle. However, with truncating spherical harmonics at a finite order, the transport equation is approximated by a system of wave equations moving at multiple distinct speeds, also known as wave-effects[4], which brings challenges for solving it and induces numerous works on the solution techniques[5, 6, 7, 8, 9, 10, 11, 12, 13]. Also, the solution from P_N might suffer from Gibbs phenomenon if angular discontinuities are present. Consequently, negative angular flux occurs before introducing any spatial approximation to the P_N equations[1]. The focus, of the relevant work herein, is then on finding remedies to improve the P_N solution.

1.2 Filtered Spherical Harmonics

Many previous studies have focused on mitigation of P_N negative solution[14, 15, 16, 1, 17, 18, 19]. Among the methods developed, the filtering is specially appealing due to its robustness, moderate computational cost, easy implementation and plausible accuracy[17, 20]. P_N can be derived by minimizing the L_2 norm of angular flux error in moment variable space. By defining a P_N minimization problem with the constraint of an artificial diffusion in angle, one obtains the prototypical filtered spherical harmonics (FP_N) method[17]. Since then, numerous different types of FP_N are proposed and examined[20, 21, 22]. Despite the success of the FP_N method, however, angular diffusion needs to be predefined, which is cumbersome and requires knowledge of the solution.

In this dissertation, we will first develop nonlinear P_N closures developed from measuring the transport residual in moment variable space. During the study of such closures, we further realize the viscosity part has the same unit as a cross section. What is more im-

portant is that the viscosity is nonlinear and defined by the solution, inspiring us to develop a FP_N method based upon it.

We will see the test results demonstrating the accuracy of such a nonlinear FP_N (NFP_N) method. Moreover, a proof for asymptotic preservation for the proposed methods will be provided. Last but not least, a Newton-Picard nonlinear time stepping method is developed and tested with the 2D Marshak wave radiative transfer problem.

1.3 Second Order Forms and Least-Squares Finite Element Methods

In many situations the transport problems are discretized in space by the discontinuous finite element method (DFEM) because it can robustly handle contact discontinuities in the solution and it behaves well in diffusive problems. However, DFEMs introduce extra degrees of freedom (DoF) and are difficult for implementation on unstructured mesh[23]. On the other hand, in order to enable the use of continuous finite element method (CFEM), a recasting from the transport equation, a first-order PDE, to a second-order PDE is convenient[19] to get stability of the scheme. We will call these recast equations second-order forms, which include the well-known even parity (EP) equation[23, 24], self-adjoint angular flux (SAAF) equation[25] and the more recently developed least-squares transport equation (LSTE) [26].

Specifically, we are interested in SAAF and LSTE. With CFEM discretization, we will prove: solving transport equation with least-squares finite element method is equivalent to CFEM-LSTE and that solving the transport equation with $1/\sigma_{\mathrm{t}}$-weighted least-squares finite element method is equivalent to CFEM-SAAF.

1.4 Issue and Remedy in Void and Absorber Transport Problems

It is natural to solve transport equation with DFEM in void. Essentially, it is to solve linear advection equation with a specific flow direction. Void problems can be difficult with many second-order forms (including SAAF and EP) due to the presence of the inverse

cross section. LSTE was then developed to provide a better treatment in void. Yet, it does not necessarily mean an accurate solution would be produced. In fact, solving multi-D transport equation in void can be erroneous and solution can be oscillatory and negative even with DFEM[27]. Solving transport with least-squares finite element using continuous basis functions can also induce negative flux. We will show that even with fine mesh in multi-D, angular flux produced with such a method can be negative.

As in data fitting, L_2 performs well only when the data is smooth. When discontinuity happens, least-squares generate spurious oscillations by trying to best fit every single datum[28, 29]. In transport problems this occurs when large residual contributions are over-corrected by a least-squares discretization. To address this problem, we develop a method that approximately solves the transport equation using L_1 finite element method. Though L_1 has been explored in fluid dynamics area, it has never been employed in neutral particle transport.

The L_1 method developed in this dissertation is based upon a simpler formulation than the one given by Guermond[30]. Further, we will provide a scheme compatible with source iteration process, which is necessary since S_N angular scheme is used with the L_1 method. The other novelty is that a L_1 boundary condition is developed, to enable incident-boundary problems.

1.5 Second-Order Form Accuracy in Contact Problem

The transport process is mono-directional between collisions. Casting the transport equation to a second order form, or using least-squares finite element methods, symmetrizes the streaming operator and transforms it to a directional Laplacian operator. Indeed, continuous basis functions can be used to solve the recast equation. However, it breaks the particle transport causality that how particles move depends on both what is behind and what is in front of the particles. As a consequence, with the presence of material

interface with cross section changes, solutions in thin side can be affected and distorted by the thick material, without local mesh refinements around the interface.

An intuition to resolve this issue is to introduce discontinuity on those interfaces. We will derive such a method by defining a new functional with weakly imposing angular flux continuity on the interface. Specifically, we will demonstrate such a method conquers the non-conservative issue of least-squares method in heterogeneous radiation transport. We further apply the method with $1/\sigma_{\mathrm{t}}$-weighted least-squares method, which resembles SAAF formulation within subdomains with doing upwinding on the interfaces. Lastly, an angular coupling scheme is provided to enable the usage of S_N-P_N coupling at the interface.

1.6 Outline

The reminder of this dissertation is organized as the following: In Section 2, we review the governing equations for time-dependent transport, thermal radiative transfer and steady-state neutron transport equations. We discuss the applications which those equations fit in. Section 3 developed a P_N closure for solving time-dependent transport equation nonlinearly based on the spatial and temporal variations of the scalar flux. Thereby, we develop a nonlinear angular viscosity. Section 4 applies the viscosity in solving transport equation with P_N method. From Section 6 through 9, we will focus on developing methods for solving steady-state neutron transport equation. Specifically, Section 6 derives the CFEM spatial discretization for LSTE and SAAF. Further, discretizations with (weighted) least-squares finite element methods will also be introduced. Section 7 developed a nonlinear method based L_1 norm minimization of transport residual to improve the solution of least-squares discretization, especially in void and absorber situations. Section 8 will develop a contiguous-discontinuous least-squares method to address the conservation issue existing in least-squares method. Inspired by the high accuracy by introducing disconti-

nuity on material interface, we will develop a similar method based on SAAF formulation in Section 9. What is more interesting is we will present a S_N-P_N angular discretization scheme therein. Section 10 comprises our conclusions on the work presented herein and outlines our recommendations for the future work in this area.

2. PROBLEM DEFINITIONS

2.1 Boltzmann Transport Equation For Neutral Particles

When describing the neutral particle transport phenomena, the Boltzmann transport equation can be written as:

$$\frac{1}{\mathcal{V}(E)}\frac{\partial\psi(\vec{r},\vec{\Omega},E,t)}{\partial t}+\vec{\Omega}\cdot\nabla\psi(\vec{r},\vec{\Omega},E,t)+\sigma_{\mathrm{t}}(\vec{r},E,t)\psi(\vec{r},\vec{\Omega},E,t)=q(\vec{r},\vec{\Omega},E,t), \tag{2.1}$$

where $\mathcal{V}(E)$ is the moving speed of the particle (length/time) for the particle with kinetic energy of E; angular flux ψ[1] is a function of position $\vec{r}=(x,y,z)$, direction $\vec{\Omega}(\mu,\varphi)$ and time t. In total, for a spatially 3D transport problem, the solution lives in a seven-dimensional phase space. σ_{t} is the macroscopic total cross section (length^{-1}) as a function of $\vec{r}$ and E. q represents the total volumetric source rate (particles (energy)/area-time-energy-steradian), which could consist of fixed source, fission source (neutronics), scattering source, Planckian source (thermal radiative transfer), etc.

To be complete, an incident boundary condition is applied for incident directions that $\vec{n}\cdot\vec{\Omega}<0$ where $\vec{n}$ the outward normal on the boundary $\partial\mathcal{D}$

$$\psi(\vec{r},\vec{\Omega},E,t)=\psi^{\mathrm{inc}}(\vec{r},\vec{\Omega},E,t),\quad \vec{r}\in\partial\mathcal{D}, \tag{2.2}$$

along with an initial condition (IC) for $t=0$ s

$$\psi(\vec{r},\vec{\Omega},E,0)=\psi^{\mathrm{IC}}(\vec{r},\vec{\Omega},E). \tag{2.3}$$

[1]Note that we use the same notation for both neutron angular flux (particles/area-time-energy-steradian) and photon intensity (energy/area-time-energy-steradian)

2.2 Steady State Neutronics Problems

In the neutronics part of this dissertation, we specifically focus on steady state problems, for which $\partial_t(\cdot) = 0$. In neutronics, the source term q can usually be separated into fission source, scattering source and fixed source.

2.2.1 Continuous energy equation

With all the sources specified, the Boltzmann equation for neutron transport is expressed as:

$$\begin{aligned}
&\vec{\Omega} \cdot \nabla \psi(\vec{r}, \vec{\Omega}, E) + \sigma_{\mathrm{t}}(\vec{r}, E)\psi(\vec{r}, \vec{\Omega}, E) \\
&= \int_0^\infty dE' \int_{4\pi} d\Omega' \, \sigma_{\mathrm{s}}(\vec{r}, \vec{\Omega}' \to \vec{\Omega}, E' \to E)\psi(\vec{r}, \vec{\Omega}, E) \\
&+ \frac{\boldsymbol{\chi}(E)}{4\pi} \int_0^\infty dE' \, \nu\sigma_{\mathrm{f}}(\vec{r}, E')\phi(\vec{r}, E') + \frac{Q(\vec{r}, E)}{4\pi},
\end{aligned} \tag{2.4}$$

where the scalar flux $\phi(\vec{r}, E, t)$ is defined by:

$$\phi = \int_{4\pi} d\Omega \, \psi. \tag{2.5}$$

$\boldsymbol{\chi}$ is the fission spectrum (energy^{-1}) and a probability function so that:

$$\int_0^\infty dE \, \boldsymbol{\chi}(E) = 1. \tag{2.6}$$

$\nu(\vec{r}, E)$ stands for mean number of neutron produced per fission reaction event and the $\sigma_{\mathrm{f}}(\vec{r}, E)$ represents the macroscopic fission cross section (length^{-1}). They are normally combined as a single variable $\nu\sigma_{\mathrm{f}}$ denoting the average number of fission-induced neu-

trons produced per collision event[3]. $\sigma_{\rm s}$ is scattering cross section which somehow represents the likelihood of a neutron getting scattered in a collision event (length^{-1}/energy-steradian). Scattering plays a crucial rule in neutronics that it transfers energy and momentum of a neutron without absorbing it and the physics behind it is quite complicated, especially in the thermal neutron energy range in thermal neutron reactors[31, 32, 33, 34]. The fixed volumetric source (particles/volume-energy) is denoted by Q.

2.2.2 Multigroup and one-group approximation

Deterministic transport methods require discretizing every component in the seven-dimensional phase space, including energy. The multigroup treatment is a commonly used technique to discretize the transport equation in energy[35]. Essentially, the whole energy range is divided into several groups with energy boundaries $E_0, \cdots, E_{\rm G}$ starting from the highest neutron energy (E_0) accounted in the calculations, where G is the user-defined total group number. Integrating Eq. (2.4) over the g$^{\rm th}$ group range ($E_{\rm g+1}, E_{\rm g}$], one finds:

$$\vec{\Omega}\cdot\nabla\psi_{\rm g}+\sigma_{\rm t,g}\psi_{\rm g}=\sum_{\rm g'=0}^{\rm G}\int_{4\pi}d\Omega'\;\sigma_{s,g'\to g}(\vec{r},\vec{\Omega}'\to\vec{\Omega})\psi'_{\rm g}(\vec{r},\vec{\Omega}') + \frac{\boldsymbol{\chi}_{\rm g}}{4\pi}\sum_{\rm g'=0}^{\rm G}\nu\sigma_{\rm f,g}\phi_{\rm g'}+\frac{Q_{\rm g}}{4\pi} \tag{2.7}$$

where

$$\psi_{\rm g}=\int_{E_{\rm g+1}}^{E_{\rm g}}dE\;\psi, \tag{2.8}$$

$$\boldsymbol{\chi}_{\rm g}=\int_{E_{\rm g+1}}^{E_{\rm g}}dE\;\boldsymbol{\chi}, \tag{2.9}$$

$$Q_{\mathrm{g}} = \int_{E_{\mathrm{g}+1}}^{E_{\mathrm{g}}} dE\, Q, \tag{2.10}$$

and

$$\phi_{\mathrm{g}} = \int_{E_{\mathrm{g}+1}}^{E_{\mathrm{g}}} dE\, \phi. \tag{2.11}$$

And ideally, the cross sections are defined as:

$$\sigma_{\mathrm{t,g}} = \frac{\int_{E_{\mathrm{g}+1}}^{E_{\mathrm{g}}} dE\, \sigma_{\mathrm{t}}\psi}{\psi_{\mathrm{g}}}, \tag{2.12}$$

$$\nu\sigma_{\mathrm{f,g}} = \frac{\int_{E_{\mathrm{g}+1}}^{E_{\mathrm{g}}} dE\, \nu\sigma_{\mathrm{f}}\phi}{\phi_{\mathrm{g}}}, \tag{2.13}$$

and

$$\sigma_{s,g'\to g} = \frac{\int_{E_{\mathrm{g}+1}}^{E_{\mathrm{g}}} dE \int_{E_{\mathrm{g}'+1}}^{E_{\mathrm{g}'}} dE'\, \sigma_{\mathrm{s}}(E' \to E)\psi(E')}{\psi_{\mathrm{g}'}}. \tag{2.14}$$

However, these definitions rely on the solution, ψ, which is undesired. Instead, one would replace the ψ with the weighting function ω well approximating the solution[36, 33, 37,

38]. Thereby, we have:

$$\sigma_{\mathrm{t,g}} = \frac{\int_{E_{\mathrm{g}+1}}^{E_{\mathrm{g}}} dE\ \sigma_{\mathrm{t}}\omega(E)}{\omega_{\mathrm{g}}}, \tag{2.15}$$

$$\nu\sigma_{\mathrm{f,g}} = \frac{\int_{E_{\mathrm{g}+1}}^{E_{\mathrm{g}}} dE\ \nu\sigma_{\mathrm{f}}\omega(E)}{\omega_{\mathrm{g}}}, \tag{2.16}$$

and

$$\sigma_{s,g'\to g} = \frac{\int_{E_{\mathrm{g}+1}}^{E_{\mathrm{g}}} dE \int_{E_{\mathrm{g}'+1}}^{E_{\mathrm{g}'}} dE'\ \sigma_{\mathrm{s}}(E'\to E)\omega(E')}{\omega_{\mathrm{g}'}}. \tag{2.17}$$

where

$$\omega_{\mathrm{g}} = \int_{E_{\mathrm{g}+1}}^{E_{\mathrm{g}}} dE\ \omega(E) \tag{2.18}$$

A further approximation is the one-group approximation where there is only one group in the whole energy range (G=1), i.e.

$$\vec{\Omega}\cdot\nabla\psi(\vec{r},\vec{\Omega}) + \sigma_{\mathrm{t}}(\vec{r})\psi(\vec{r},\vec{\Omega}) = \int_{4\pi} d\Omega'\ \sigma_{\mathrm{s}}(\vec{r},\vec{\Omega}'\to\vec{\Omega})\psi(\vec{r},\vec{\Omega})$$
$$+\frac{1}{4\pi}\nu\sigma_{\mathrm{f}}(\vec{r})\phi(\vec{r}) + \frac{Q(\vec{r})}{4\pi}. \tag{2.19}$$

2.2.3 Operator forms

The transport equation is composed of different operators on the solution. Therein, the equation shrinks to a form of several operators. For simplicity, we restrict the derivations to one-group neutron transport equation

$$\mathcal{L}\psi = \mathcal{S}\psi + \mathcal{F}\psi + \frac{Q}{4\pi}, \tag{2.20}$$

where

$$\mathcal{L} = \vec{\Omega} \cdot \nabla + \sigma_{\mathrm{t}}, \tag{2.21}$$

$$\mathcal{S}\psi(\vec{\Omega}) = \int\limits_{4\pi} d\Omega' \; \sigma_{\mathrm{s}}(\vec{\Omega}' \rightarrow \vec{\Omega})\psi(\vec{\Omega}'), \tag{2.22}$$

and

$$\mathcal{F}\psi = \frac{1}{4\pi}\nu\sigma_{\mathrm{f}} \int\limits_{4\pi} d\Omega \; \psi. \tag{2.23}$$

The operator form for non-fissile materials is given by

$$\mathcal{L}\psi = \mathcal{S}\psi + \frac{Q}{4\pi}. \tag{2.24}$$

2.2.4 k-eigenvalue calculations

In steady-state eigenvalue calculations for fission reactors, it is common to include an effective multiplication constant k_{eff}[39], which measures the equilibrium between neutrons produced and removed[40].

$$\vec{\Omega} \cdot \nabla \psi(\vec{r}, \vec{\Omega}, E) + \sigma_{\text{t}}(\vec{r}, E)\psi(\vec{r}, \vec{\Omega}, E) = \tag{2.25}$$
$$\int_0^\infty dE' \int_{4\pi} d\Omega' \, \sigma_{\text{s}}(\vec{r}, \vec{\Omega}' \to \vec{\Omega}, E' \to E)\psi(\vec{r}, \vec{\Omega}, E) + \frac{1}{k_{\text{eff}}} \frac{\boldsymbol{\chi}(E)}{4\pi} \int_0^\infty dE' \, \nu\sigma_{\text{f}}(\vec{r}, E')\phi(\vec{r}, E').$$

The corresponding multigroup approximation is expressed as:

$$\vec{\Omega} \cdot \nabla \psi_{\text{g}} + \sigma_{\text{t,g}}\psi_{\text{g}} = \frac{1}{k_{\text{eff}}} \sum_{\text{g}'=0}^{\text{G}} \int_{4\pi} d\Omega' \, \sigma_{s,g' \to g}(\vec{r}, \vec{\Omega}' \to \vec{\Omega})\psi'_{\text{g}}(\vec{r}, \vec{\Omega}') + \frac{\boldsymbol{\chi}_{\text{g}}}{4\pi} \sum_{\text{g}'=0}^{\text{G}} \nu\sigma_{\text{f,g}}\phi_{\text{g}'}. \tag{2.26}$$

Moreover, when G=1, we have the one group approximation:

$$\vec{\Omega} \cdot \nabla \psi(\vec{r}, \vec{\Omega}) + \sigma_{\text{t}}(\vec{r})\psi(\vec{r}, \vec{\Omega}) = \int_{4\pi} d\Omega' \, \sigma_{\text{s}}(\vec{r}, \vec{\Omega}' \to \vec{\Omega})\psi(\vec{r}, \vec{\Omega}) + \frac{1}{k_{\text{eff}}} \frac{1}{4\pi} \nu\sigma_{\text{f}}(\vec{r})\phi(\vec{r}), \tag{2.27}$$

or equivalently, the operator form:

$$\mathcal{L}\psi = \mathcal{S}\psi + \frac{1}{k_{\text{eff}}}\mathcal{F}\psi. \tag{2.28}$$

2.3 Thermal Radiative Transfer

2.3.1 Thermal radiative transfer (TRT)

For TRT, the thermal photon is strongly coupled with the material. In such a situation, the source q is a Planckian source. The problem is described by a radiation transport equation for the radiation intensity ψ (energy/area-time-energy-steradian) and a material energy equation[7, 19, 4] for the material temperature T (keV):

$$\frac{1}{c}\frac{\partial \psi}{\partial t} + \vec{\Omega}\cdot\nabla\psi + \sigma_{\mathrm{t}}\psi = \frac{1}{4\pi}\sigma_{\mathrm{s}}\phi + \sigma_{\mathrm{a}}\mathcal{B}, \tag{2.29a}$$

$$C_v\frac{\partial T}{\partial t} = \int_0^\infty dE\ \sigma_{\mathrm{a}}\left(\phi - 4\pi\mathcal{B}\right), \tag{2.29b}$$

where c is the speed of light (length). C_v is the specific heat capacity (energy/volume-temperature). $\mathcal{B}$ is the Planckian (energy/-area-time-energy-steradian) and expressed as:

$$\mathcal{B} = \frac{2E^3}{h^3c^2}\left[\exp\left(E/kT\right) - 1\right]^{-1} \tag{2.30}$$

Integrating the radiation transport equation over all the energy leads to the gray (one-group) approximation[41]. The gray approximation is applied to all the TRT problems in this dissertation. By integrating the Planckian $\mathcal{B}$ over all the energies, we will have:

$$\int_0^\infty dE\ \mathcal{B} = \frac{acT^4}{4\pi}. \tag{2.31}$$

Then the gray radiative transfer equation with material equations is

$$\frac{1}{c}\frac{\partial \psi}{\partial t} + \vec{\Omega}\cdot\nabla\psi + \sigma_{\mathrm{t}}\psi = \frac{1}{4\pi}\sigma_{\mathrm{s}}\phi + \frac{1}{4\pi}\sigma_{\mathrm{a}}acT^4, \tag{2.32a}$$

$$C_v \frac{\partial T}{\partial t} = \int_0^\infty dE \; \sigma_{\mathrm{a}} \left(\phi - acT^4 \right). \tag{2.32b}$$

Often, due to the insignificance of the scattering in TRT problems[42], we neglect the scattering to further simplify the radiation equation in Eq. (2.32a):

$$\frac{1}{c}\frac{\partial \psi}{\partial t} + \vec{\Omega} \cdot \nabla \psi + \sigma_{\mathrm{a}} \psi = \frac{1}{4\pi} \sigma_{\mathrm{a}} acT^4 \tag{2.33}$$

2.3.2 Linear time-dependent transport equation

Radiation transport itself in TRT is difficult even without the material coupling[43]. The time-dependent linear radiation transport equation is usually used as a substitute to TRT by introducing scattering and fixed sources:

$$\frac{1}{\mathcal{V}}\frac{\partial \psi(\vec{r}, \vec{\Omega}, t)}{\partial t} + \vec{\Omega} \cdot \nabla \psi(\vec{r}, \vec{\Omega}, t) + \sigma_{\mathrm{t}}(\vec{r}) \psi(\vec{r}, \vec{\Omega}, t) = \frac{Q(\vec{r}, t)}{4\pi} + \frac{1}{4\pi} \sigma_{\mathrm{s}}(\vec{r}) \phi(\vec{r}, t). \tag{2.34}$$

2.4 Angular Approximations for Deterministic Transport

2.4.1 Legendre expansion of scattering

Though the scattering depends on both the incident and outgoing angles, we usually assumes the dependence is only on the scattering angle $\mu_0 = \vec{\Omega}' \cdot \vec{\Omega}$. The double scattering cross section is azimuthally isotropic[36] so the cross section can be expanded using Legendre moments of the cross section:

$$\sigma_{\mathrm{s}}(\vec{r}, \vec{\Omega}' \to \vec{\Omega}) = \frac{\sigma_{\mathrm{s}}(\vec{r}, \mu_0)}{2\pi} = \sum_{l=0}^{N_{\mathrm{s}}} \frac{2l+1}{4\pi} \sigma_{\mathrm{s},l}(\vec{r}) P_l(\mu_0), \tag{2.35}$$

where N_{s} is the truncated order of maximum anisotropy of scattering used in transport calculations.

With the Legendre expansion, it is straightforward to prove that Legendre moments of the cross section σ_l and spherical harmonics Y_l^m is the eigenpair of the scattering operator[25], i.e.:

$$\mathcal{S}Y_l^m = \sigma_l Y_l^m. \tag{2.36}$$

2.4.2 Truncated spherical harmonics (P_N) method

By expanding the angular flux as a linear combination of a series of spherical harmonics with the expansion coefficients, also called moments ϕ_l^m, the angular flux in general dimensions can be written as:

$$\psi(\vec{r}, \vec{\Omega}) = \sum_{l=0}^{\infty} \sum_{m=-l}^{l} \phi_l^m Y_l^m(\vec{\Omega}), \tag{2.37}$$

where $\phi_l^m = \int\limits_{4\pi} d\Omega \; \bar{Y}_l^m(\vec{\Omega})$. The above expansion is exact in angle. The expansion in real-world calculations, however, goes along with a truncation approximation with involving spherical harmonics to a certain order. Generically assuming truncation occurs to $l = N$, then the P_N expansion is re-expressed as:

$$\psi(\vec{r}, \vec{\Omega}) \approx \sum_{l=0}^{N} \sum_{m=-l}^{l} \phi_l^m Y_l^m(\vec{\Omega}). \tag{2.38}$$

In 3D, $|m| \leq l$ and there are $(N+1)(N+2)$ moments in total involved in the P_N expansion. In 2D, there are $(N+1)(N+2)/2$ relevant moments[5, 6, 7, 19]. In 1D, total moment number is $N+1$. By introducing the expansion into the transport equation, one could derive the P_N equations, as introduced in Appendix A. One could also derive second-order forms of transport equations in moment forms, such SAAF-P_N equation, as briefly described in Appendix B.

2.4.3 Discrete ordinates (S_N) method

The other angular discretization scheme we consider is the S_N method, which essentially approximate the angular integration over the whole sphere by using numerical quadrature rules. Specifically, as a collocation method in angle[2], all the directions are located as the quadrature abscissae. Namely[3]:

$$\int_{4\pi} d\Omega\ f(\vec{\Omega}) \approx \sum_{\mathrm{m}=1}^{M} w_{\mathrm{m}} f(\vec{\Omega}_{\mathrm{m}}). \tag{2.39}$$

Further, in S_N approximation, the scattering operation turns into the following form for a specific direction[3]:

$$\mathcal{S}\psi = \sum_{l=0}^{N_{\mathrm{s}}} \frac{2l+1}{4\pi} \sigma_l \sum_{m=-l}^{l} \phi_l^m Y_l^m(\vec{\Omega}_m), \tag{2.40}$$

and the moments are approximated using the quadrature rule.

3. RESIDUAL INDICATED MOMENT CLOSURES IN CARTESIAN GEOMETRY*

3.1 Background and Motivations

Though P_N has the spectral convergence in angle for smooth data and is ray-effect proof, it suffers from negative radiation densities, which is prohibited in TRT problems that it will drive material temperature to be negative and crash the simulation[17]. The reason is that such a spectral method suffers from Gibbs phenomenon when simulating angular flux discontinuous in angle[17]. It is actually true not only for P_N, but also for any other linear closure, such as D_N closure. In order to mitigate the negativity, nonlinear closure must be developed[12, 7]. Examples include the entropy based closures[15, 44] and positive P_N closure[14]. While eliminating the negative radiation densities, those methods, however, are computationally intensive due to solving dual problems from the nonlinear process every time step.

As a matter of fact, no analysis has been put on the closure effects on the transport residual in the moment variable space. The section, therefore, starts off exploring the effects of the angular closures on the least-squares measure of transport residual in moment space. Thereby, two nonlinear closures will be derived. The resulting closures are more damp the oscillatory solution nonlinearly based on the solution while remains relatively computational effective.

*Part of this section is adapted from "Moment Closures Based on Minimizing the Residual of the P_N Angular Expansion in Radiation Transport" by Weixiong Zheng and Ryan G. McClarren, 2016. *Journal of Computational Physics*[1] Copyright 2016 Elsevier. The author exercises his right granted by the copyright agreement to use the published journal article for inclusion in the dissertation as scholarly use.

3.2 Derivation of the Method

3.2.1 Error functional derivation of the P_N equations

To simplify the analysis, we begin with an energy-independent transport equation for neutral particles in slab geometry given by [35]

$$\frac{1}{v}\frac{\partial\psi(x,\mu,t)}{\partial t}+\mu\frac{\partial}{\partial x}\psi(x,\mu,t)+\sigma_{\mathrm{t}}\psi(x,\mu,t)=\frac{Q}{2}+\frac{\sigma_{\mathrm{s}}\phi}{2}. \tag{3.1}$$

In this equation the angular flux of particles is given by $\psi(x,\mu,t)$ with units of particles per area per time. Our notation is standard with $x\in\mathbb{R}$ being the spatial variable, $\mu\in[-1,1]$ as the cosine of the angle between the slab normal and the direction of flight, and t as the time variable. The macroscopic total and scattering interaction cross-section with units of inverse length is given by σ_{t} and σ_{s}, respectively. The scalar flux, $\phi(x,t)$, defined as

$$\phi(x,t)=\int_{-1}^{1}d\mu\,\psi(x,\mu,t). \tag{3.2}$$

In order to solve Eq. (3.1) one needs to apply discretizations in space, angle, and time. In this work we focus on the angular discretization, in particular we will expand the angular dependence in Legendre polynomials as

$$\psi(x,\mu,t)=\sum_{l=0}^{\infty}C_l\phi_l(x,t)P_l(\mu), \tag{3.3}$$

where the Legendre polynomials are given by

$$P_l(\mu)=\frac{1}{2^l l!}\frac{d^l}{d\mu^l}\left[(\mu^2-1)^l\right]. \tag{3.4}$$

Here, $\phi_l(x,t)$ is an expansion function, and C_l is a normalization constant given by

$$C_l = \left(\int_{-1}^{1} d\mu \, P_l(\mu) P_l(\mu) \right)^{-1}. \tag{3.5}$$

This technique is known as the P_n method, and generalizes to general three-dimensional geometries by making the expansion functions spherical harmonics [35].

The typical way that the expansion functions and normalization constants are generated is via a Galerkin procedure where one assumes a Legendre expansion of the angular flux, plugs it into the transport equation, and integrates the result against different Legendre polynomials. An alternative derivation involves defining a error functional measuring the difference of angular flux, ψ and the spherical-harmonics-reconstructed angular flux using an expansion that is truncated beyond the $l = N$ moment, $\bar{\psi}_N$ [17]. We define the errror functional as the integrated square of the difference between the true angular flux and the truncated expansion:

$$\Gamma_1(\mu) = \int_{-1}^{1} d\mu \, (\psi - \bar{\psi}_N)^2, \tag{3.6}$$

where

$$\bar{\psi}_N(\mu) = \sum_{l=0}^{N} C_l \phi_l(x,t) P_l(\mu). \tag{3.7}$$

In order to minimize the functional in Eq. (3.7), one forces $\partial \Gamma_1 / \partial \phi_l = 0$, leading to the expansion coefficients being given by

$$\phi_l = \int_{-1}^{1} d\mu \, \psi(x,\mu,t) P_l(\mu). \tag{3.8}$$

Using this definition for the expansion coefficients, we take a certain Legendre poly-

nomial and integrate it with the transport equation, Eq. (3.1), over μ to get:

$$\frac{1}{v}\frac{\partial}{\partial t}\phi_l + \frac{l}{2l+1}\frac{\partial \phi_{l-1}}{\partial x} + \frac{l+1}{2l+1}\frac{\partial \phi_{l+1}}{\partial x} + (\sigma_t - \sigma_{\mathrm{s}}\delta_{l,0})\phi_l = Q\delta_{0,l},\ l = 0, 1, \cdots N \quad (3.9)$$

This system is not closed in the sense that the equation for the Nth moment includes the $N+1$ moment, which is not included in our truncated expansion. A common closure is to set $\phi_{N+1} = 0$. Thereafter, the closed P_N equation system can be described as:

$$\frac{1}{v}\frac{\partial}{\partial t}\phi_l + \frac{l}{2l+1}\frac{\partial \phi_{l-1}}{\partial x} + \frac{l+1}{2l+1}\frac{\partial \phi_{l+1}}{\partial x}(1 - \delta_{N,l}) + (\sigma_{\mathrm{t}} - \sigma_{\mathrm{s}}\delta_{0,l})\phi_l = Q\delta_{0,l},\ l = 0, 1, \cdots, N. \quad (3.10)$$

These equations are the standard P_N equations. We will now change the derivation to use a functional that minimizes the residual in the transport equation given a particular expansion.

3.2.2 A functional based on the squared-residual

Rather than basing the functional on the squared difference between the expansion and the true solution, one could also measure the squared residual of the P_N approximation as:

$$\Gamma(\{\phi_{l'} : l' = 0, \cdots\}) = \int_{-1}^{1} d\mu\ R^2, \quad (3.11)$$

where R is the residual computed when the expanded flux to order N is plugged into the transport equation with an isotropic source. For simplicity, we consider the pure absorber problem (though removing this restriction leads to the same results) leading to the

definition of residual as

$$R = \left(\frac{1}{v}\partial_t + \mu\partial_x + \sigma_{\mathrm{t}}\right)\sum_{l'=0}^{N}\frac{2l'+1}{2}\phi_{l'}P_{l'}(\mu) - \frac{Q}{2}. \tag{3.12}$$

In order to minimize the functional Γ, we focus on finding moment sets which make $\partial\Gamma/\partial\phi_l = 0$ for all l. Through this path, we could gain an insight into the impact on the residual due to the closure.

Taking the functional derivative of Eq. (3.11) leads to:

$$\frac{\partial\Gamma}{\partial\phi_l} = (2l+1)\sigma_{\mathrm{t}}\int_{-1}^{1} d\mu\; RP_l(\mu) \; + (2l+1)\frac{\partial}{\partial\phi_l}\left[\frac{\partial}{\partial x}\phi_l\right]\int_{-1}^{1} d\mu\; R\mu P_l(\mu) + \\ (2l+1)\frac{1}{v}\frac{\partial}{\partial\phi_l}\left[\frac{\partial}{\partial t}\phi_l\right]\int_{-1}^{1} d\mu\; RP_l(\mu). \tag{3.13}$$

Note that for $l \leq N$, the following identity holds

$$\int_{-1}^{1} d\mu\; RP_l(\mu) = \frac{1}{v}\partial_t\phi_l + \frac{l}{2l+1}\frac{\partial\phi_{l-1}}{\partial x}(1-\delta_{0,l}) + \sigma_t\phi_l + \frac{l+1}{2l+1}\frac{\partial\phi_{l+1}}{\partial x} - Q\delta_{0,l}. \tag{3.14}$$

Comparing Eq. (3.14) with Eq. (3.10), one sees that the integral is equal to zero, i.e.

$$\int_{-1}^{1} d\mu\; RP_l(\mu) = 0, \qquad l \leq N. \tag{3.15}$$

Also, by using recurrence relation of Legendre polynomial, one has:

$$\int_{-1}^{1} d\mu\; R\mu P_l(\mu) = \frac{l}{2l+1}\int_{-1}^{1} d\mu\; \mu P_{l-1}(\mu)R + \frac{l+1}{2l+1}\int_{-1}^{1} d\mu\; \mu P_{l+1}(\mu)R. \tag{3.16}$$

Therefore, Eq. (3.13) can be rewritten as:

$$\frac{\partial \Gamma}{\partial \phi_l} = (2l+1)\left(\sigma_{\mathrm{t}} + \frac{1}{v}\frac{\partial}{\partial \phi_l}\left[\frac{\partial}{\partial t}\phi_l\right]\right)\int_{-1}^{1} d\mu\; RP_l(\mu) + \frac{\partial}{\partial \phi_l}\left[\frac{\partial}{\partial x}\phi_l\right]\left(l\int_{-1}^{1} d\mu\; RP_{l-1}(\mu) + (l+1)\int_{-1}^{1} d\mu\; RP_{l+1}(\mu)\right). \quad (3.17)$$

When $l < N$, plugging Eq. (3.15) back into Eq. (3.17) leads to:

$$\frac{\partial \Gamma}{\partial \phi_l} = 0, \qquad l < N. \quad (3.18)$$

That is, all of the P_N equations minimize the squared-residual for ϕ_l for all $l < N$. This is why the omission of the scattering term does not affect our results: the scattering term only appears in the $l = 0$ equation. It is in the $l = N$ equation where the closure enters. We will now explore what that equation tells us.

For $l = N$, the same substitution, omitting the algebraic process, results in:

$$\frac{\partial}{\partial \phi_N}\left[\frac{\partial}{\partial x}\phi_N\right]\left(\int_{-1}^{1} d\mu\; RP_{N+1}(\mu)\right). \quad (3.19)$$

Therefore, expanding the integral term in Eq. (3.19) gives us the final expression for the N^{th} order functional derivative:

$$\frac{\partial \Gamma}{\partial \phi_N} = (N+1)\frac{\partial}{\partial \phi_N}\left[\frac{\partial}{\partial x}\phi_N\right]\left(\frac{1}{v}\partial_t \phi_{N+1} + \frac{N+1}{2N+3}\frac{\partial \phi_N}{\partial x} + \sigma_t \phi_{N+1} + \frac{N+2}{2N+3}\frac{\partial \phi_{N+2}}{\partial x}\right). \quad (3.20)$$

This equation can tell us the impact of a closure on the residual: to this equation we can substitute in a closure and see how it effects the derivative of the squared residual.

3.2.3 Discussion on two conventional closures

Zero closure

Introducing the zero closure ($\phi_{\mathcal{M}} = 0,\ \mathcal{M} > N$) into Eq. (3.20) gives the following:

$$\frac{\partial \Gamma}{\partial \phi_N} = (N+1)\frac{\partial}{\partial \phi_N}\left[\frac{\partial}{\partial x}\phi_N\right]\frac{N+1}{2N+3}\frac{\partial \phi_N}{\partial x}. \tag{3.21}$$

This equation indicates that the squared-residual will be minimized only if the spatial derivative of ϕ_N is zero. This restriction is not expected to be satisfied in general problems.

Diffusive closure

Levermore et al. suggested a diffusive closure which takes a form similar to Fick's law for the relationship between ϕ_{N+1} and ϕ_N[45]:

$$\phi_{N+1} = -\frac{1}{\sigma_{\mathrm{t}}}\frac{N+1}{2N+3}\partial_x \phi_N. \tag{3.22}$$

They, therein, name the corresponding system D_N in the sense that the closure is essentially taking the definition of diffusion to a high-order closure. Also, Oh and Holloway independently derived a low order D_2 method for transient problem by assuming the closed moment ϕ_{N+1} is time-independent such that one could directly gain the Fick's law-like relationship in Eq. (3.22)[46]. They name the method P_3QS, short for P_3 quasi static, because of the approximation used to find the closure.

Substituting Eq. (3.22) into Eq. (3.20), we get:

$$\frac{\partial \Gamma}{\partial \phi_N} = (N+1)\frac{\partial}{\partial \phi_N}\left[\frac{\partial}{\partial x}\phi_N\right]\left(-\frac{N+2}{2N+3}\frac{1}{v}\partial_t\left(\frac{1}{\sigma_{\mathrm{t}}}\partial_x \phi_N\right) + \frac{N+2}{2N+3}\frac{\partial \phi_{N+2}}{\partial x}\right). \tag{3.23}$$

This result indicates where the D_N closure might be accurate. It will minimize the squared-residual when the time derivative of ϕ_N is zero and when the spatial derivative

of the ϕ_{N+2} is zero. We cannot know for a general problem what the derivative of ϕ_{N+2} will be. Nevertheless, we can predict when transients have died out in a particular problem. In such an occasion we predict that the D_N closure will be superior to the zero closure because the derivative of the ϕ_{N+2} moment impacts the residual, rather than the ϕ_N moment in the zero closure.

3.2.4 Two new closures

Approximations on higher moments

Equation (3.20) indicates that we should seek a closure such that:

$$\frac{1}{v}\partial_t\phi_{N+1} + \frac{N+1}{2N+3}\frac{\partial\phi_N}{\partial x} + \sigma_t\phi_{N+1} + \frac{N+2}{2N+3}\frac{\partial\phi_{N+2}}{\partial x} = 0, \tag{3.24}$$

which is equivalent to introducing a higher order P_N approximation without changing the truncation order. The closure, leading to zero functional derivative in moment space, would potentially lead to a minimized residual of the P_N approximation. However, this is not feasible practically since truncating at a certain order N would lead to the loss of information of higher orders, e.g. ϕ_{N+2}. The value of Eq. (3.24) is that it indicates how one could close the system to minimize the residual in moment space.

Formally, we can rewrite Eq. (3.24) to implicitly define a closure as

$$\phi_{N+1} = -\frac{1}{\sigma_\mathrm{t} + \dfrac{\partial_t\phi_{N+1}}{v\phi_{N+1}} + \dfrac{(N+2)}{(2N+3)\phi_{N+1}}\partial_x\phi_{N+2}}\frac{N+1}{2N+3}\partial_x\phi_N. \tag{3.25}$$

A moment-limited closure

The closure indicated by Eq. (3.25) shares a similar form with diffusive closure, except, there are additional terms added to correct the closure. Though it is still a formal closure since it depends on the value of ϕ_{N+1} and ϕ_{N+2}, it implies adding spatial and temporal

flux limiters to the diffusive closure could help minimize $\partial\Gamma/\partial\phi_N$. Therefore, we propose the following closure:

$$\phi_{N+1} = -\frac{1}{\sigma_\mathrm{t} + \left|\frac{\partial_t\phi_0}{v\phi_0}\right| + \left|\frac{\alpha\partial_x\phi_N}{\phi_0}\right|}\frac{N+1}{2N+3}\partial_x\phi_N. \tag{3.26}$$

A desirable feature is that if a proper α is used, one could prove that this form limits the magnitudes of the closure as follows:

$$\begin{aligned}|\phi_{N+1}| &= \frac{1}{\sigma_\mathrm{t} + \left|\frac{\partial_t\phi_0}{v\phi_0}\right| + \alpha\left|\frac{\partial_x\phi_N}{\phi_0}\right|}\frac{N+1}{2N+3}\left|\partial_x\phi_N\right| \\ &\leq \frac{1}{\alpha\left|\frac{\partial_x\phi_N}{\phi_0}\right|}\frac{N+1}{2N+3}\left|\partial_x\phi_N\right| = \frac{N+1}{\alpha(2N+3)}|\phi_0|\end{aligned} \tag{3.27}$$

For instance, fixing α at $(N+1)/(2N+3)$ would result in:

$$|\phi_{N+1}| < |\phi_0| \tag{3.28}$$

That is similar to the situation of limiting current to the scalar flux to stabilize the system in moment space. We, therefore, name this approach the moment-limited diffusive (MLD) closure.

A modification: transient $\mathbf{P}_N$ closure

The moment limited closure could be modified to use ϕ_0, instead of ϕ_N in the closure. Specifically, the modified closure is expressed as:

$$\phi_{N+1} = -\frac{1}{\sigma_\mathrm{t} + \left|\frac{\partial_t\phi_0}{v\phi_0}\right| + \left|\frac{\alpha\partial_x\phi_0}{\phi_0}\right|}\frac{N+1}{2N+3}\partial_x\phi_N \tag{3.29}$$

There are two motivations for this choice. On one hand, this selection is to make a form similar to a high order extension of flux-limited diffusion with an additional constraint on the temporal evolution of the solution (i.e. the $\partial_t \phi_0$ term). Moreover, in multidimensional problems ϕ_0 is the only moment that is a scalar, making the extension to full spherical harmonics closures straightforward. In contrast, extending MLD_N to multi-D requires individual estimates of the spatial limiters for each single $(N+1)^{\text{th}}$ moment equation. For instance, for MLD_3 in 2D with moments generated from complex-value spherical harmonics, four different spatial limiters need estimating, and the situation is worse as N is increased. This is another motivation for the simpler closure in Eq. (3.29).

To minimize the residual, the parameter α would depend on the unknown angular flux distribution. For simplicity, we fix the α in Eq. (3.29) to a constant. Though the central theme is similar to the MLD model in that one adjusts the diffusivity nonlinearly based on the solution, we have not been able to prove that the closure limits the magnitude of ϕ_{N+1} to be less than the scalar flux.

The test results in the following sections demonstrate this modification improves the accuracy in the transients that arise when a majority of the particles in the system have not had a collision. We, therefore, name the model the transient P_N closure (TP_N).

Closure effects on residual functional derivative

By introducing the MLD_N or TP_N closures, the functional derivative in Eq. (3.20) can be written as:

$$\frac{\partial \Gamma}{\partial \phi_N} = \frac{(N+1)(N+2)}{2N+3} \frac{\partial}{\partial \phi_N} \left[\frac{\partial}{\partial x} \phi_N \right] \left(-\frac{1}{v} \partial_t \left(\frac{1}{\sigma_{\text{t}} + \nu} \partial_x \phi_N \right) + \frac{\nu}{\sigma_{\text{t}} + \nu} \partial_x \phi_N + \partial_x \phi_{N+2} \right) \tag{3.30a}$$

$$\text{MLD}_N : \quad \nu = \left| \frac{\partial_t \phi_0}{v \phi_0} \right| + \left| \frac{\alpha \partial_x \phi_N}{\phi_0} \right| \tag{3.30b}$$

$$\mathrm{TP}_N: \quad \nu = \left|\frac{\partial_t \phi_0}{v\phi_0}\right| + \left|\frac{\alpha \partial_x \phi_0}{\phi_0}\right|. \tag{3.30c}$$

Adding flux or moment limiters does not necessarily minimize the residual functional. In fact, Eq. (3.30) automatically adjusts the functional derivative based upon the solution. In occasions where the spatial derivative of the solution tends to be large, $1/(\sigma_\mathrm{t} + \nu)$ goes to be zero while $\nu/(\sigma_\mathrm{t}+\nu)$ limits to one. Eq. (3.30) has the limit of P_N's functional derivative. When the solution is smooth and slowly varying in time, ν tends to be small and Eq. (3.30) limits to D_N. In effect, the closures improve the D_N method during transients and preserve the beneficial properties of that closure in the steady limit.

Generalization of TP_N models

The form of the TP_N closure is similar to the Larsen-type flux limited correction to radiation diffusion[47] with an additional time derivative term. The form of a Larsen flux limiter allows the impact of the limiter to be adjusted by making the terms in the closure weighted by a power, rather than using a linear sum. We can perform the same adjustment to our model by writing

$$\phi_{N+1} = -\frac{1}{\tilde{\sigma}} \frac{N+1}{2N+3} \partial_x \phi_N \tag{3.31a}$$

$$\tilde{\sigma} = \left(\sigma_\mathrm{t}^n + \left|\frac{1}{v\phi_0}\partial_t \phi_0\right|^n + \left|\frac{\alpha \partial_x \phi_0}{\phi_0}\right|^n\right)^{\frac{1}{n}} \tag{3.31b}$$

Typically, the value of n is set to be one or greater, though recent work has demonstrated that there are problems where $n < 1$ can give improved solutions [48]. It is then of interest to test the effects from different powers n on our closure.

3.2.5 Multi-D extension of TP_N closure

D_N equations

The D_N model is identical to P_N up to the $(N-1)^{\mathrm{th}}$ moment equations. Dropping off the time derivative terms of the $(N+1)^{\mathrm{th}}$ moment equations of P_{N+1} system, one can

easily find:

$$\phi^m_{N+1} = -\frac{1}{\sigma_{\mathrm{t}}} \sum_{\chi=x,y,z} \sum_{l',m'} \mathbf{A}^{l',m'}_{\chi,N+1,m} \partial_\chi \phi^{m'}_{l'}, \quad |m| \leq N+1 \tag{3.32}$$

Plugging Eq. (3.32) into the relevant moment equations up to Order N will then lead to the D_N system. Note that Eq. (3.32) illustrates that D_N is equivalent to adding a diffusive correction to the P_{N-1} system[45].

TP_N closure

It is straightforward to extend modify the D_N model to be TP_N by adding a correction term ν to the denominator of Eq. (3.32):

$$\phi^m_{N+1} = -\frac{1}{\sigma_{\mathrm{t}} + \nu} \sum_{\chi=x,y,z} \sum_{l',m'} \mathbf{A}^{l',m'}_{\chi,N+1,m} \partial_\chi \phi^{m'}_{l'}, \quad |m| \leq N+1 \tag{3.33a}$$

$$\nu \equiv \left(\left| \frac{\partial_t \phi^0_0}{v \phi^0_0} \right| + \alpha \frac{\|\nabla \phi^0_0\|}{|\phi^0_0|} \right). \tag{3.33b}$$

3.3 Numerical Details

The 1D MLD_N and TP_N closures are implemented with the diamond difference for spatial discretization and a semi-implicit scheme as detailed below. At present only TP_N closure is extended to multi-D applications with discontinuous Galerkin finite element method (DFEM) in space and semi-implicit scheme in time.

3.3.1 1D implementation

For our closures the highest order moment we keep in our system is N with N even. With N even, there are N first-order PDEs and one second-order PDE. This requires $N+2$ total boundary conditions or $N/2+1$ conditions on each boundary in 1-D. We can use the

standard Marshak conditions in this case where on the left boundary we satisfy

$$\int_0^1 d\mu\, \psi_{\text{inc}}^{\text{L}}(\mu) P_l(\mu) = \sum_{i=0}^{N} c_i \phi_i - \frac{c_{N+1}}{\sigma_{\text{t}} + \left|\frac{\partial_t \phi_0}{v\phi_0}\right| + \alpha \left|\frac{\partial_x \phi_k}{\phi_0}\right|} \frac{N+1}{2N+3} \partial_x \phi_N,$$

$$l = 1, 3, .., N+1, , \tag{3.34}$$

where k is equal to 0 or N, and $c_i = \int_0^1 d\mu\ P_l(\mu) P_i(\mu)$. The conditions at the right boundary are the same except the integral is over $\mu \in [-1, 0]$.

For a spatial discretization we use the diamond difference method with unknowns that live at cell edges. For a uniform mesh with cell width h, the semi-discrete equations become

$$\frac{h}{v}\partial_t \phi_{l,i} + \frac{l}{2l+1}\left(\phi_{l-1,i+1/2} - \phi_{l-1,i-1/2}\right) + \frac{l+1}{2l+1}\left(\phi_{l+1,i+1/2} - \phi_{l+1,i-1/2}\right)$$
$$+ h\left(\sigma_{\text{t},i} - \sigma_{\text{s,i}}\delta_{0,l}\right)\phi_{l,i} = Q_{l,i}\delta_{0,l}h, \quad l = 0, \cdots, N-1 \tag{3.35a}$$

$$\frac{h}{v}\partial_t \phi_{N,i} + \frac{N}{2N+1}\left(\phi_{N-1,i+1/2} - \phi_{N-1,i-1/2}\right) + h\sigma_{\text{t},i}\phi_{N,i}$$
$$- \frac{N(N+1)}{(2N+1)(2N+3)}\left(\frac{\partial_x \phi_{N,i+1/2}}{\tilde{\sigma}_{i+1/2}} - \frac{\partial_x \phi_{N,i-1/2}}{\tilde{\sigma}_{i-1/2}}\right) = 0 \tag{3.35b}$$

$$\tilde{\sigma}_i = \sigma_{\text{t},i} + \left|\frac{\partial_t \phi_{0,i}}{v\phi_{0,i}}\right| + \alpha\left|\frac{\phi_{k,i+1/2} - \phi_{k,i-1/2}}{h\phi_{0,i}}\right|, \tag{3.35c}$$

where k is either 0 or N, and

$$\partial_x \phi_{l,i+1/2} = \frac{\phi_{l,i+1} - \phi_{l,i}}{h}, \tag{3.36a}$$

$$\phi_{l,i} = \frac{1}{2}\left(\phi_{l,i+1/2} + \phi_{l,i-1/2}\right), \quad l = 0, \cdots, N, \tag{3.36b}$$

$$\tilde{\sigma}_{i+1/2} = \frac{1}{2}\left(\tilde{\sigma}_{i+1} + \tilde{\sigma}_i\right). \tag{3.36c}$$

The time discretization we use is semi-implicit that we evaluate all terms in Eq. (3.35) at time level $n+1$ (i.e., backward Euler) except $\tilde{\sigma}$, which is evaluated explicitly at level n. This makes each time step a linear solve. If we implicitly update $\tilde{\sigma}$, each step would require a nonlinear solve.

3.3.2 2D TP$_N$ implementation

Previously, D$_N$ has been discretized in space by the streamline diffusion continuous finite element method[45] and finite volume method[46, 49] in space. We choose a variant of the DFEM finite element method in this work mainly for its preservation of the asymptotic diffusion limit. In particular, we apply the local discontinuous Galerkin (LDG) method, which was developed for time dependent convection-diffusion equation[50]:

$$\frac{\partial u}{\partial t} + \nabla \cdot \mathrm{F}(u) + \nabla a(x,y,z)\nabla u = 0. \tag{3.37}$$

In the LDG method, one introduces an auxiliary variable $\vec{q}$, such that Eq. (3.37) can be rewritten as:

$$\frac{\partial u}{\partial t} + \nabla \cdot \mathrm{F}(u) + \nabla \cdot \vec{q} = 0, \tag{3.38a}$$

$$\vec{q} = a(x,y,z)\nabla u. \tag{3.38b}$$

3.4 Numerical Results

All 1D tests in this section are performed with MATLAB[51]. The 2D TP$_N$ closure is implemented with the C++ open source finite element library deal.II[52]. The results for the plane source problem, two-beam problem and the Reed's problem will be presented for 1D closures and 2D TP$_N$ test results will be presented with line source problem.

3.4.1 Plane source test problem

The medium in the plane source problem is a pure scatterer ($\sigma_{\mathrm{t}} = \sigma_{\mathrm{s}} = 1$). At time $t = 0$, there is a pulsed source in the middle of an infinite slab. The initial condition is

$$\psi(z, \mu, 0) = \frac{\delta(z)}{2}. \tag{3.39}$$

An analytic solution to the transport equation for this problem is available in the benchmark suite AZURV1[53]. The solution has a wavefront at $z = \pm vt$. The number of particles in the wavefront decays over time so that after enough time the wavefront has a negligible magnitude. Therefore, late in time the solution is a smooth due to the scattering of particles from the initial pulse. Also, both the D_N and P_N methods approximate the transport solution well at late times (e.g., $t = 10$ in Figure 3.1a), whereas early on in the transient neither can capture the analytic solution. This is predicted by the analysis in Section 3.2.3 because early in time the spatial and time derivatives of the solution are not small. At $x = 0$ the D_6 solution is closer to the analytic solution than the P_7.

In the solution at earlier times (see Fig. 3.1b) there are spikes that are the numerical representation of waves of uncollided particles. Since the time dependent P_N system is a hyperbolic wave equation system, particles moves in several discrete wave speeds. The consequence is that the solutions will have $N + 1$ spikes, analytically represented by a Dirac delta function. These artifacts from the P_N (and D_N) discretization are known as wave effects[4].

Comparison of MLD$_N$ and linear closures

In the results below, unless otherwise noted, we use a value of $\alpha = 2/3$. Later, we discuss this choice.

In Figure 3.2 we compare MLD and the diffusive closure on the plane source problem.

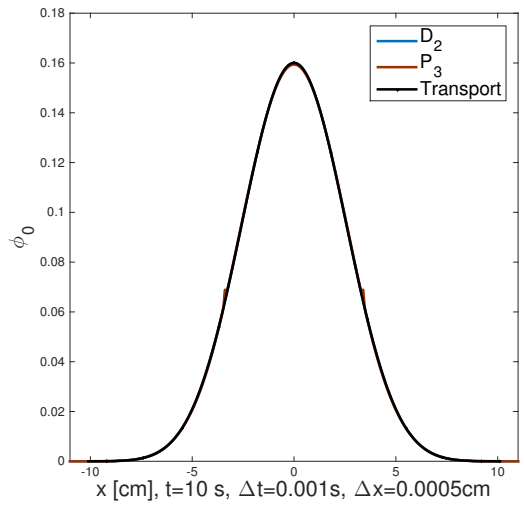

(a) Late time solutions ($t = 10$)

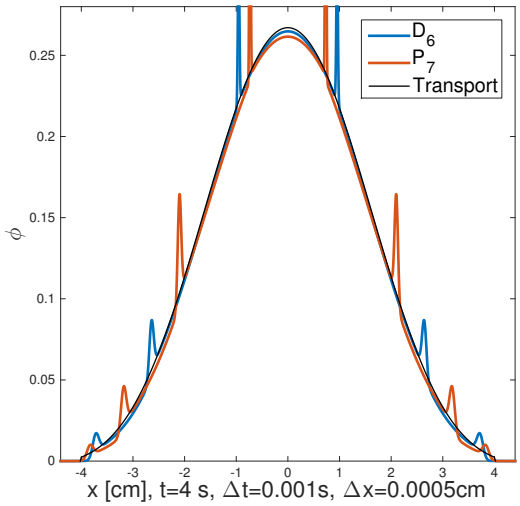

(b) Solutions at an earlier time ($t = 4$)

Figure 3.1: Examples of P_N and D_N in plane source problem. Notice that early in time the discrete wave speeds in the $P_N$and D_N solutions.

At an early time, Figure 3.2a, the wave effects are greatly reduced in the MLD_6 model relative to D_6 and P_7. Furthermore, the solution away from the waves is much closer to the transport solution. At later time, Figure 3.2b, the wave effects in P_7 and D_6 are still present whereas the MLD_6 solution has the overall shape of the transport solution with small oscillations near the D_6 waves.

Comparison of MLD_N and TP_N

We next compare the two models developed in this paper. At $t = 1$s in the plane source problem, as shown in Figure 3.3, with both $N = 6$ and 8, the TP_N model gives results closer to the transport solution than the MLD_N model.

At 5s after the pulse, it is seen that in Figure 3.4, both closures do not produce artificial waves in the solution to the degree that D_N or P_N solutions do. The MLD_N and TP_N results basically agree to the transport solution in the middle except the solution near the wavefronts in the ± 5 cm. At the wavefront none of these methods captures the solution

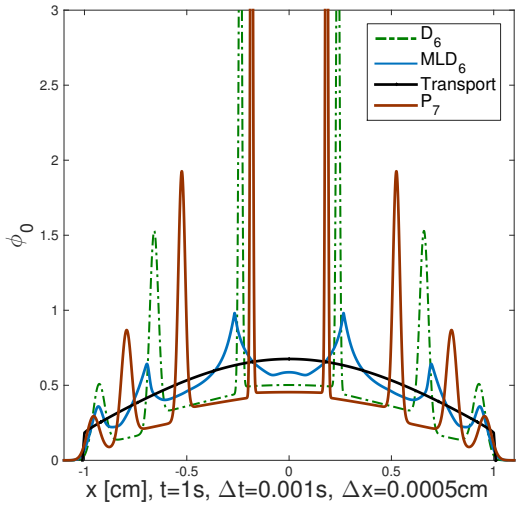

(a) MLD_6 results at 1s in plane source problem.

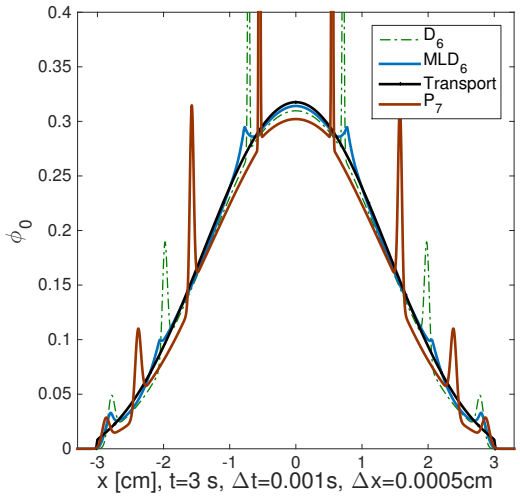

(b) MLD_6 results at 3s in plane source problem.

Figure 3.2: MLD_N and linear closure solutions to the plane source problem at different times.

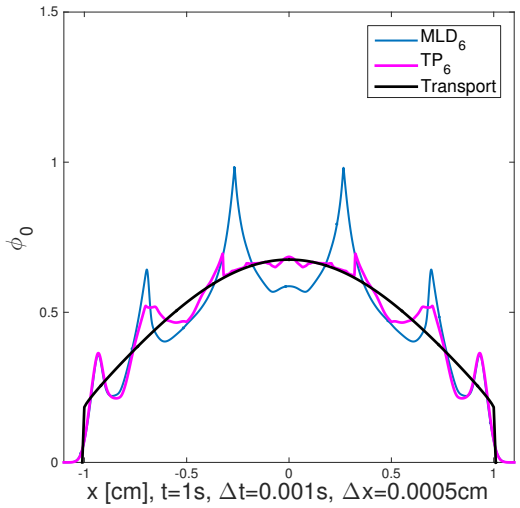

(a) MLD_6 and TP_6 results.

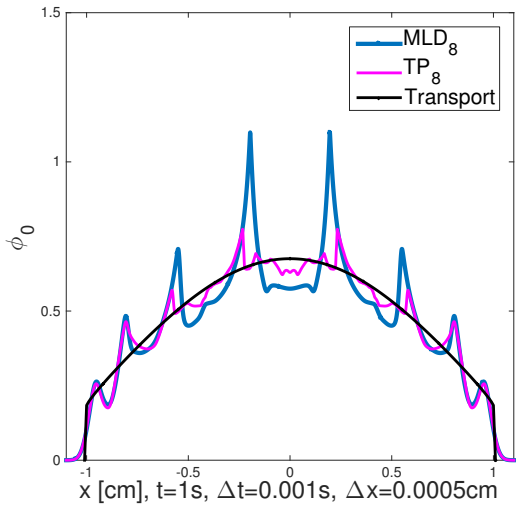

(b) MLD_8 and TP_8 results.

Figure 3.3: MLD_N and TP_N comparison at 1 s.

correctly.

In summary, both the MLD_N and TP_N closures effectively damp the unphysical modes

(large spikes), which leads to relatively accurate solutions for the transport problem during short-time transients. Moreover, on every problem we have tested, the TP_N method was superior to the MLD_N method. Henceforth, we will focus on this method.

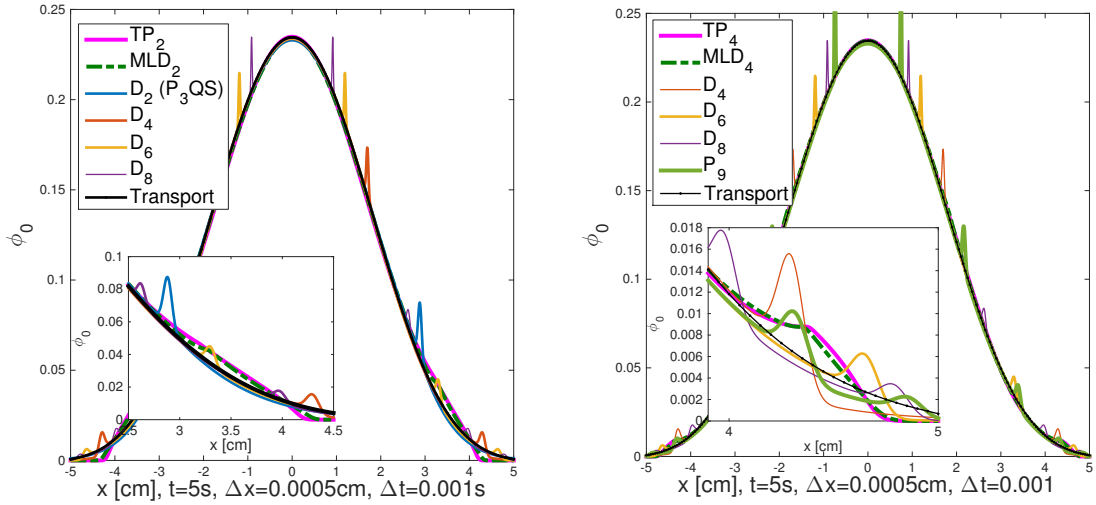

(a) MLD_2 and TP_2 results.

(b) MLD_4 and TP_4 results.

Figure 3.4: MLD_N and TP_N comparison at 5s.

The impact of spatial and temporal terms in the model

To further investigate the importance of different terms in the closure, we individually turn on/off different derivatives in the closure. It is observed that, at 1 s in the plane source problem in Figure 3.5a using only the spatial derivative term in the closure makes the solution flat in the middle and, as a result, too low. On the other hand, merely using the temporal derivative terms retains a better flux profile in the slab center, while the artificial spikes are not yet dampened effectively as with spatial limiter at later times in Figure 3.5b. Note that the moving modes propagate further than those with the spatial limiter. Therefore, we conclude that both derivative terms in the closure contribute to the accuracy

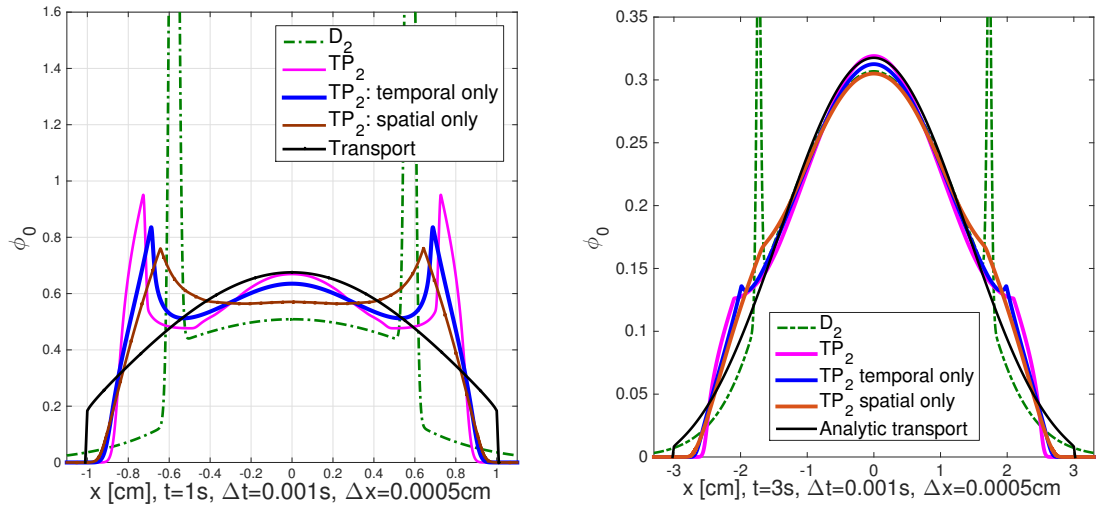

(a) TP_2 results at $t = 1$ s

(b) TP_2 results at $t = 3$ s

Figure 3.5: Illustration of the impact of the spatial and temporal derivative terms in the TP_N closure.

of the model.

Impact from Power n of TP_N models

It is observed that for low order TP_N approximations, varying the power n does adjust the dissipation in the solution. As illustrated in Figure 3.6, the originally proposed value, $n = 1$ retains the correct value near $x = 0$. Simultaneously, $n = 2$ makes the solution flatter. On the other hand, reducing n to $1/3$ amplifies the dampened spikes and makes the solution more similar to the even P_N flux profile in that it has a stationary mode at $x = 0$. It would suggest small powers should be avoided. Yet, all solutions agree with each other when the transient is passed. We have also observed that with increasing N the solution becomes less sensitive to the power n for $n > 1$.

Spatial derivative coefficient α

In our initial derivation of the TP_N model we surmised that the value of α should be between $1/3$ and 1 because it appears in a similar way to the coefficients of the P_N Ja-

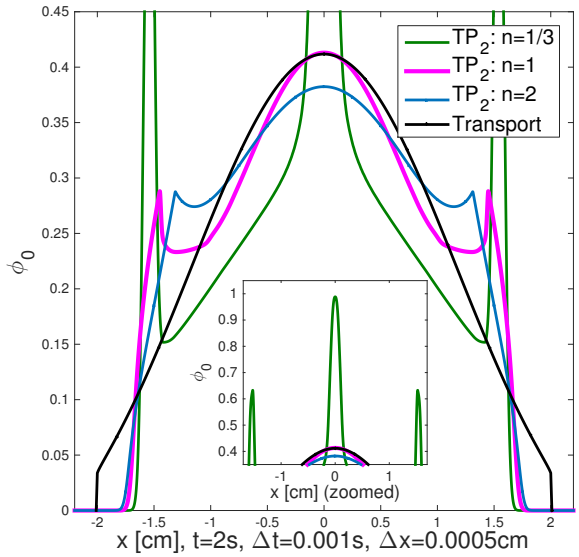

Figure 3.6: Effects from different power n on the in Eq. (3.31b).

cobian. Since these coefficients range from $1/3$ through 1, we therefore used the median value $2/3$.

We present a limited parameter study for α in Figure 3.7. Therein, the flux profiles vary in several respects. With the smallest value shown, $\alpha = 1/3$, the solution is much closer to the D_N solution: the solution is too low in the middle, and the wave effects are amplified. On the other hand, increasing α to 1 appears to amplify and spread the waves in the solution in addition to increasing the solution near $x = 0$ too much.

Compared with 1/3 and 1, $2/3$ provides the most accurate and least oscillatory result among the three choices. We have performed more studies using many more values of α and found that α values of 0.5 through 0.7 are comparable to the 2/3 solution.

3.4.2 Two-beam problem

The second test problem is a highly absorbing problem with isotropic incident angular fluxes on both sides of a slab. The scattering ratio, $c = \sigma_\mathrm{s}/\sigma_\mathrm{t}$, of the medium is 0.1. The original test problem is in steady state[44]. We, however, run this problem in time-

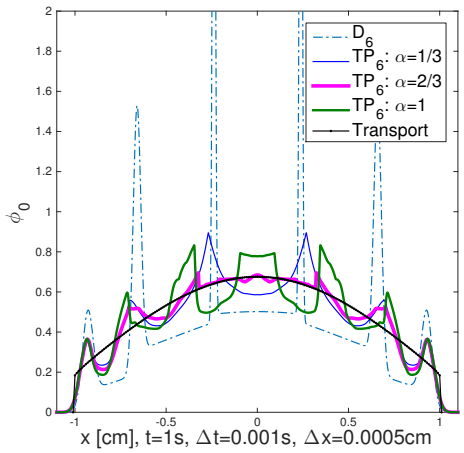

Figure 3.7: Effects from different coefficients α in the closure. With $\alpha = 0$ the spatial derivative of the scalar flux has no impact on the closure.

dependent mode to see how different methods approach the steady state solution. These results are shown in Figure 3.8.

Both TP_N and D_N converge to the reference solution at 10 s. Theoretically, incident particles from different sides of the slab are not supposed to meet before $t = L/(2v) = 5$ s. Yet, D_2 artificially moves particles faster than their physical speeds, making the solution greater than 10^{-8} at $x = 0$ as early as $t = 2$s. On the other hand, the TP_2 model retains a sharper wavefront and as a result the solution at $x = 0$ is below 10^{-8} until 5 s.

Though the incident flux is isotropic on the boundary, the angular flux gradually turns to become strongly anisotropic and form a beam-like distribution in the middle of the slab due to the strong absorption. This beam-like behavior of the angular flux is a potential challenge for the model. Some closure models, such as the entropy based closure model (M_N), have difficulty in resolving the beam. For the M_N method, it tends to have artificial shock in the middle (Ref. [15, 44]). It is also suspected in Ref. [15] that this shock could possibly caused by small errors when solving minimization problem governing the M_N method. Fortunately, the TP_N model does not have the artificial shock in this problem.

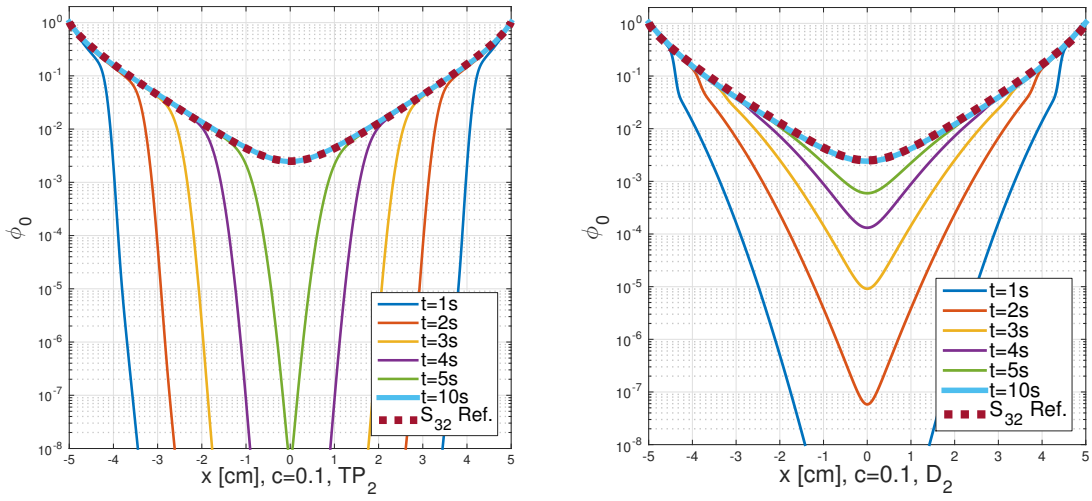

Figure 3.8: Comparison between TP_2 and D_2 (P_3QS) solutions to two-beam problem.

3.4.3 Reed's problem

The last test problem in this work is Reed's problem [54]. It contains several regions with largely varied properties including strong pure absorbers, voids, strong source and material discontinuities.

The numerical example in Figure 3.9 is TP_4 and D_4 solutions of Reed's problem. In voids, in order to make the diffusive closure well-posed, an artificial absorption ζ is chosen:

$$\sigma_{\mathrm{t}}' = \sigma_{\mathrm{t}} + \zeta, \tag{3.40}$$

where ζ is a small number, which is fixed at 10^{-8}. For the TP_N model we only need a correction when $\tilde{\sigma}$ is zero, (i.e., in voids when then the scalar flux is constant in space and time). The correction we use is

$$\tilde{\sigma}' = \tilde{\sigma} + \zeta, \tag{3.41}$$

We use 800 cells in the discretization for D_4, D_6, and TP_4. The S_N solutions are calculated with cell centered difference using 16,000 cells. We observe that TP_4 retains an

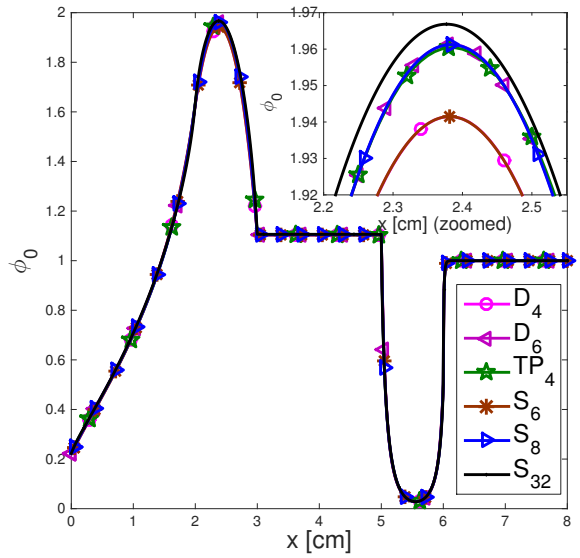

Figure 3.9: Reed's problem solved with D_4, TP_4, and D_6 compared with S_{32}.

accuracy comparable to D_6 and S_8. As a comparison, D_4 displays comparable accuracy to S_6. Given that in 1-D slabs, S_{N+1} gives identical solutions to P_N, this result is evidence that the D_N and TP_N models improve the solution as indicated by our residual analysis. As our analysis also predicts, the TP_N solution is superior to both D_N and P_N.

Overall, as illustrated in Figure 3.10, the pointwise errors from TP_4 are comparable to D_6 and smaller than those from D_4 method in most regions especially for regions with large errors ($> 10^{-2}$). We also observe that the boundary treatment in Eq (3.34) brings about 0.8% of error, slightly higher than D_4. However, the global L_1 norm of error for D_4 (estimated based on the fine-mesh S_{32} solution) is 0.129 and is larger than that of TP_4, which is 0.061. For comparison, the D_6 solution has an error of 0.066.

3.4.4 2D line source problem

The line source problem is a 2D variation of the plane source problem in 1D slab geometry. The problem is an infinite, pure scattering medium ($\sigma_t = \sigma_s = 1$) with no

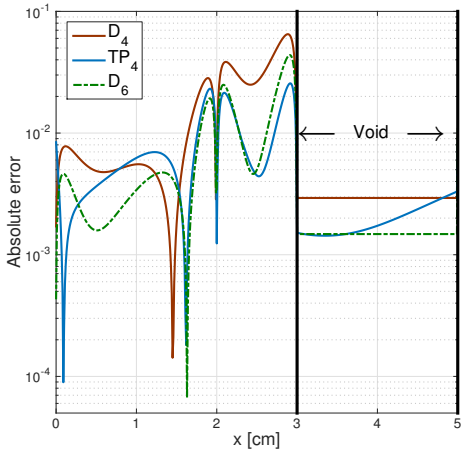

(a) Pointwise absolute errors of D_4, TP_4, and D_6 methods (Part 1).

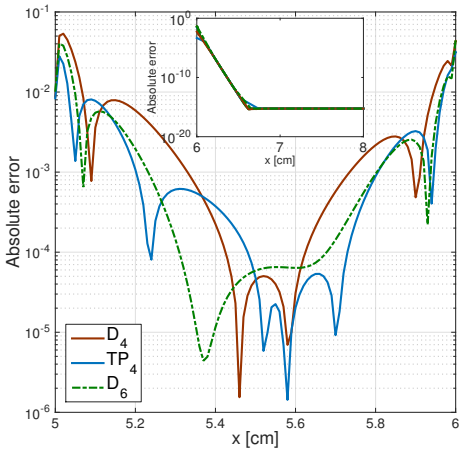

(b) Pointwise absolute errors of D_4, TP_4, and D_6 methods (Part 2).

Figure 3.10: Errors as a function of space in Reed's problem.

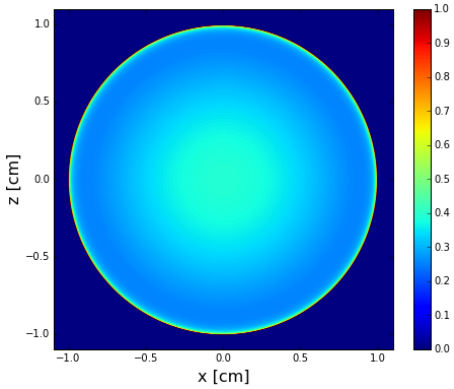

(a) Analytic transport

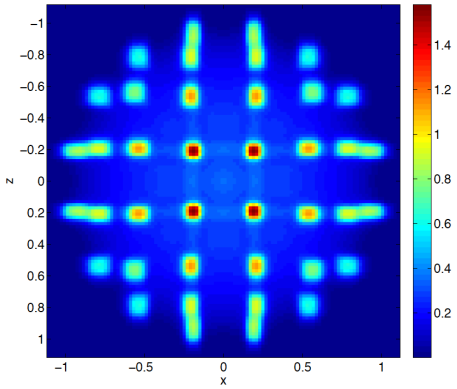

(b) S_8

Figure 3.11: 2D line source problem at $t = 1$ s with transport and S_N.

source. The initial condition is given by[53]:

$$\psi(x, z, \vec{\Omega}, 0) = \frac{\delta(x)\delta(z)}{4\pi}. \tag{3.42}$$

S_8 result in Figure 3.11b is achieved from Ref. [17]. The analytic solution is shown in

Figure 3.11a from the benchmark code AZURV1[53]. P_N, D_N and TP_N results in Figures 3.12 and 3.13 are achieved with $\Delta t = 0.02$ s and $\Delta x = 0.02$ cm, respectively. The wavefront at $r = \sqrt{x^2 + z^2} = vt$, essentially a moving delta function, will induce oscillations and negative scalar fluxes in P_N and D_N methods as illustrated in Figures 3.12a and 3.12b. Meanwhile, for this streaming dominated problem, S_N results have strong ray-effects as in Figure 3.11b. On the other hand, TP_2 solution presents plausible results in Figure 3.13a. Increasing the angular order to TP_6 will further improve the solution as illustrated in Figure 3.13b.

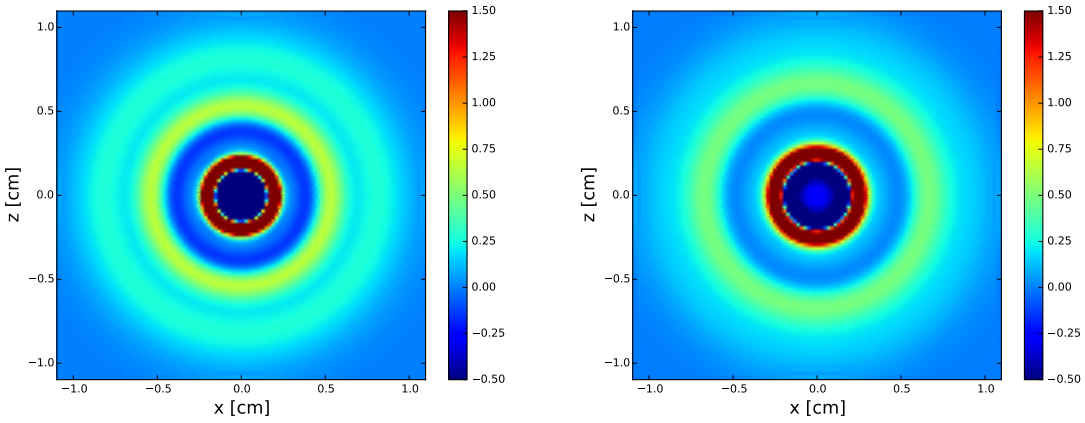

(a) P_7 (b) D_6

Figure 3.12: 2D line source problem at $t = 1$ s with D_N and P_N.

Unlike the 1D TP_N model, multi-D TP_N models for different angular orders do not have a single coefficient α, therefore, the results shown in Figure 3.13 are obtained with different coefficients. Figures 3.14a and 3.14b presents the diagonal lineout plots of TP_2, and TP_6 with different α. Changing the α for each angular order can effectively change the results, as observed in 1D. Unfortunately, the “optimal" values for different angular orders are different, e.g. while $\alpha = 0.1$ would lead to relatively accurate TP_2 results, the

"optimal" α changes 1.5 for TP_6.

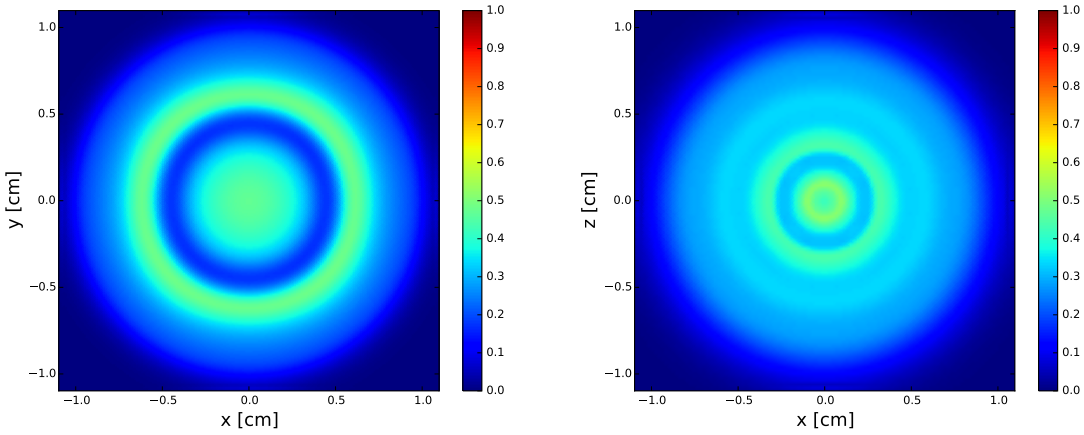

(a) TP_2 (b) TP_6

Figure 3.13: 2D line source problem at $t = 1$ s.

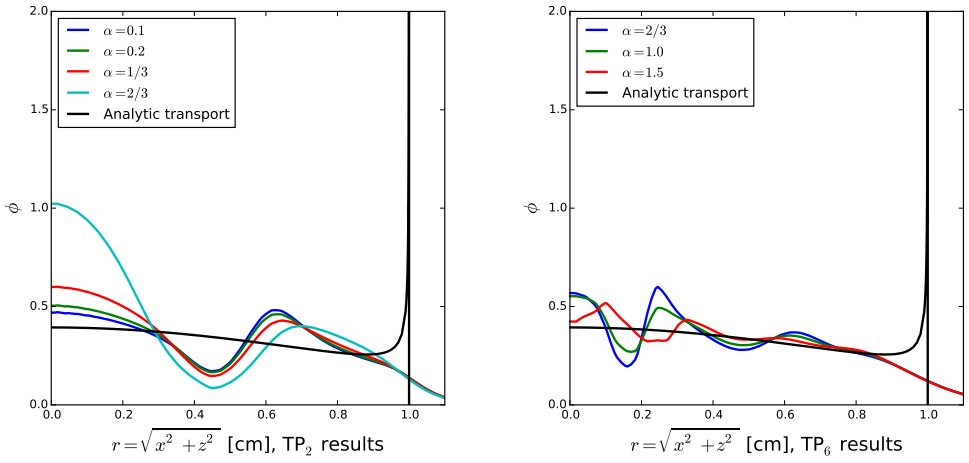

(a) TP_2 results with different α. (b) TP_6

Figure 3.14: TP_6 results with different α.

2D P_N, D_N and TP_N are solved with (semi-)implicit discretization in time and DG/LDG

method in space. A GMRES solver is used with the Jacobi preconditioner. A comparison of timings for TP_N and linear closures is made in Table 3.1. Simulations were run on a Mac mini with Intel i7-3615 processor and 16GB 1600MHz DDR3 RAM.

Table 3.1: Timings for line source problem at 1s.

	P_3	TP_2	D_2
Setup+assembly time [s]	6.9	7.4	7.2
Estimate+assemble limiter time [s]	0	16.5	0
Solving+preconditioning time [s]	124.6	215.6	562.8
Total CPU time [s]	131.5	228.5	570.0
	P_5	TP_4	D_4
Setup+assembly time [s]	20.6	19.5	18.5
Estimate+assemble limiter time [s]	0	28.3	0
Solving+preconditioning time [s]	383.5	482.0	1308.8
Total CPU time [s]	404.1	529.8	1327.3
	P_7	TP_6	D_6
Setup+assembly time [s]	43.7	42.4	43.0
Estimate+assemble limiter time [s]	0	153.2	0
Solving+preconditioning time [s]	734.5	760.4	2424.7
Total CPU time [s]	778.1	956.0	2467.7

With LDG method, D_N and TP_N have the same number of degrees of freedom (DoFs) as P_{N+1} with the same basis functions used on the same mesh. The overall CPU time of TP_N is much shorter than D_N. The hypothesis is that the D_N model sets the time dependence of ϕ_{N+1}^m to be zero, forcing particles in that mode to move with infinite speed. This makes D_N model physically ill-posed in time dependent problems. Numerically, the ill-posedness causes the degradation of the preconditioning efficiency.

On the other hand, though TP_2's solving time is around 73% higher than P_3, TP_6's solving time is comparable to P_7. The correction brought by flux limiters affects not only the physical properties as discussed in 1D scenarios, but also the computational proper-

ties. Overall, we conclude TP_N would be comparably efficiently solved as P_N in multi-D applications.

3.5 Summary

In this section, we analyzed the effects on the P_N approximation residual caused by different closures. We provide a new explanation of the reasons the conventional P_N and P_N with diffusive closure has issues in transient simulations, such as the pulsed plane source problem in 1D and line source problem in 2D. Based on the analysis, we proposed two novel closures, the “moment-limited" closure for 1D and “transient” P_N closure in 1D and 2D. The results we presented indicate that, relative to other linear closures, our new closures perform better on a variety of problems, including the notorious plane source problem and line-source problem.

Last but not least, it can be realized that the ideas behind the TP_N model could be used in other transport models. For instance, this type of closure could be applied to the simplified P_N method [55].

4. NONLINEAR FILTERED MOMENT CLOSURE FOR SIMULATING TIME-DEPENDENT RADIATION TRANSPORT

4.1 Introduction

In Section 3, the TP_N closure, a nonlinear P_N closure, is proposed for solving time dependent linear radiation transport equation with P_N expansion in angle. Indeed, it overcomes several difficulties in P_N and improves it: the TP_N model alleviates the negative solutions where P_N suffers from Gibbs phenomenon[17]. Also, as a modified diffusive closure, it improves the D_N closure by setting the boundedness of the solution and increasing the implicit solver efficiency.

However, there are realizable downsides found in multi-D test problems. While TP_N is quite efficient for high order P_N in 1D and low order P_N in general dimension, it does not perform consistently when extending to high order P_N in multi-D. Therein, the solution is quite sensitive to the multiplier applied to the nonlinear viscosity. Also, as increasing the P_N order, boundedness of the model observed in 1D tests is weakened and negative solution manifests.

Despite the issues mentioned above, TP_N still has its significance that it derives a nonlinear viscosity that would provide a mechanism to enable the P_N angular model to be adjusted in light of the solution. In fact, efforts have been put on angular viscosity to improve P_N model. The prototypical angular viscosity is yet implemented in a filter initially proposed by McClarren and Hauck[17]. Several other filtering models or solving techniques are then developed thereafter[21, 22, 18]. Such a method, in essence, is equivalent to adding artificial anisotropic scattering in the moment system. With a carefully prescribed viscosity, the filtering presents plausibly accurate results where P_N solution is either erroneous or negative.

An intuition is then to combine the idea of filtering and the nonlinear viscosity developed in previous section. Such a combination, on one hand, might fix the issue existing in high order TP$_N$; on the other hand, would rather provide an automatic prescription of the amount of artificial scattering used in the filtering.

4.2 Theory

4.2.1 Minimization view of multi-D P$_N$ expansion

Appendix A introduces how P$_N$ equations are formulated: by testing the transport equation, with expanding angular flux as a linear combination of finite orders of spherical harmonics, using spherical harmonics up to order $l = N$ in angular space, one obtains a series of equations for the expansion coefficients, also called the moments. In fact, the P$_N$ method may also be viewed as a finite element method in angle. The derivation can also come from minimizing least-squares angular error. For multi-D P$_N$, the derivation is identical to 1D slab geometry (see Eq. (3.6)) except the angular basis is changed from Legendre polynomial to spherical harmonics. Let us define the least-squares measure of P$_N$ angular flux errors in angle as the following functional:

$$\Gamma_{\mathrm{P}_N} = \int_{4\pi} d\Omega \ \left(\psi_{\mathrm{P}_N} - \psi\right)^2 . \tag{4.1}$$

Minimizing the functional above, we recover the P$_N$ projection:

$$\phi_l^m = \int_{4\pi} d\Omega \ \psi(\vec{\Omega}) \bar{Y}_l^m(\vec{\Omega}), \tag{4.2}$$

which is identical to the relationship gained from utilizing the orthogonality in Eq. (A.2). The P$_N$ equations can then be generated by performing the integration $\int_{4\pi} d\Omega \ (\cdot) \bar{Y}_l^m(\vec{\Omega})$ to transport equation.

4.2.2 Linear filtering overview

Angular penalty based filtering

As a spectral method in angle, P_N attains the exponential convergence for smooth angular flux. When discontinuity manifests in angle, however, a truncated P_N expansion suffers from Gibbs phenomenon and consequently oscillation and negativity occur to angular flux before introducing any spatial discretization. To damp those artifacts, McClarren and Hauck introduce artificial diffusion in angle, namely:

$$\Gamma_{\mathrm{FP}_N} = \int_{4\pi} d\Omega \ \left(\psi_{\mathrm{FP}_N} - \psi\right)^2 + \alpha \int_{4\pi} d\Omega \ \left(\nabla^2_{\vec{\Omega}} \psi_{\mathrm{FP}_N}\right)^2, \tag{4.3}$$

where α is a penalty coefficient and

$$\psi_{\mathrm{FP}_N} = \sum_{l,m} Y_l^m \phi^m_{l,\mathrm{FP}_N}. \tag{4.4}$$

By recognizing $\nabla^2_{\vec{\Omega}} Y_l^m = -l(l+1) Y_l^m$, we can minimize Eq. (4.3) and approach:

$$\phi^m_{l,\mathrm{FP}_N} = \frac{\phi_l^m}{1 + \alpha l^2 (l+1)^2}. \tag{4.5}$$

In order to preserve thick diffusion limit, α is argued to be defined as

$$\alpha = \frac{c\Delta t}{\Delta x N^2} \frac{1}{(\sigma_{\mathrm{t}} L + N)^2} \tag{4.6}$$

With spatial and temporal discretizations, the filtering is equivalent to adding the following viscosity ν_l to the l^{th} moment equations:

$$\nu_l = \frac{l^2 (l+1)^2}{c\Delta t l^2 (l+1)^2 + \Delta x N^2 (\sigma_{\mathrm{t}} L + N)^2}, \quad l = 1, \cdots, N, \tag{4.7}$$

That being said, a viscosity term $\mathbf{D}$ is inserted into the P_N equation system shown in Eq. (A.3):

$$\frac{1}{c}\frac{\partial\vec{\phi}}{\partial t}+\sum_{\chi=x,y,z}\mathbf{A}_\chi\vec{\phi}+\left(\mathbf{\Sigma}_\mathrm{t}-\mathbf{S}+\mathbf{D}\right)\vec{\phi}=\vec{Q}, \tag{4.8}$$

where $\mathbf{D}=\mathrm{diag}(0,\nu_1\mathbf{I}_{\mathrm{b}_1},\cdots,\nu_N\mathbf{I}_{\mathrm{b}_N})$.

Variations

Despite the success in damping angular oscillations, the viscosity in Eq. (4.7) does not have a proper continuum limit as $\Delta x,\Delta t\rightarrow 0$[17]. In fact, with shrinking the mesh and time steps, the filter becomes ill-defined. Yet, it illuminates that adding a viscosity in moment equations is resembling introducing angular diffusion. Since then, other works alternatively defines viscosity without such a minimization rationale to overcome P_N's issue. As an example, Olson[22] proposed the following variation:

$$\nu_l=\sigma_{\mathrm{eff}}\left(\frac{l}{N}\right)^k,\quad l=1,\cdots,N, \tag{4.9}$$

where k is a coefficient chosen by modeler. σ_{eff} is an effective cross section. In fact, Frank et al. proposed this viscosity independently in another way and name it exponential filter due to the way of their formulation[20]. Radice, on the other hand, examined four filters[21]. Ahrens proposed another filter in order to gain a better transition when changing the P_N order[56]. Overall, these variations obtain accuracy enhancements compared with P_N in a wide range of test problems, as observed in the prototypical filtering.

Related issues

A potential issue for the filters developed in previous works[17, 22, 21, 18, 56] is that they are “linear". It means the viscosity is unrelated to the radiation field information.

However, in problems with thin-thick contact interface where shadows might form, the filtering globally applied in the problems would bring in over diffusion of the solution. Though strategies such as defining localized filter[18] overcomes this shortcoming, it requires knowledge of the problem and solution and cannot easily be generalized.

Besides, the preservation of thick diffusion limit for the linear filters, except McClarren's, is not taken into account. Adding viscosity to the first moment equations without caution might break the the preservation, which is crucial for simulating TRT problem with thick materials.

4.2.3 Constructing a nonlinear filter

Formulation

In Section 3, while defining a P_N closure, we realized that the change to the cross section in the closure takes a similar form with the limiter in flux limited diffusion, which possesses the unit of a cross section. A more favorable property is that the factor is determined on the fly based on the solution variations in space and time. This naturally fit in the filtering method as our expectation. Then we propose to construct a nonlinear filter based on the facts above as[1]:

$$\nu_l = c_N \left(\frac{l}{N}\right)^k \left(\left|\frac{\partial_t \phi_0^0}{\phi_0^0}\right| + \frac{\|\nabla \phi_0^0\|}{|\phi_0^0|}\right), \quad l = 2, \cdots, N \tag{4.10a}$$

$$\mathbf{D} = \mathrm{diag}\left(0, 0\mathbf{I}_{\mathrm{b}_1}, \nu_2 \mathbf{I}_{\mathrm{b}_2}, \cdots, , \nu_N \mathbf{I}_{\mathrm{b}_N}\right) \tag{4.10b}$$

We leave the filtering out of the first moment equation such that the thick diffusion limit can be preserved, as will be discussed in Section 5.

[1] k is fixed at 3 in the dissertation. The effects of changing k is referred to the work in [18].

Significance and issue

We expect the angular dissipation is added only when necessary. The calculation of such a viscosity, unlike other nonlinear moment method such as positive P_N[14] or the entropy based M_N requiring solving the dual problems[49, 15], which is computationally intensive and complex, is simple and scalable[1], making the real-world application more approachable.

Still, the viscosity has the coefficient c_N not determined We would rather leave it problem dependent. For problems tested in this section, c_N is set to be $0.5 \sim 1$, which accomplishes the work well. Indeed, it is the disadvantage. But it also gives modeler freedom to tune the strength of the nonlinear filtering. On the other hand, the nonlinear filtering adds flexibility of assigning the value to c_N. Even with improperly large value of c_N for transient problems such as the line-source test, NFP_N would produce acceptably accurate solution when the solution varies slowly in space and time.

4.3 Discretizations and Implementation

Spatially discretization is carried out by using DFEM with bilinear basis in consideration for the preservation of thick diffusion limit (see Section D.1). In time, a semi-implicit integrator which treats the viscosity explicitly using information from previous time steps while engaging backward Euler method for the other parts, as described in Section 3. In Section 5, when interfacing the radiation with material coupling, a fully implicit scheme is realized to ensure the stability.

4.4 Numerical Results

The testing codes for this section are implemented with the C++ based open source finite element library deal.II[52]. The results for the line source problem, checkerboard problem and simplified Hohlraum problem will be presented.

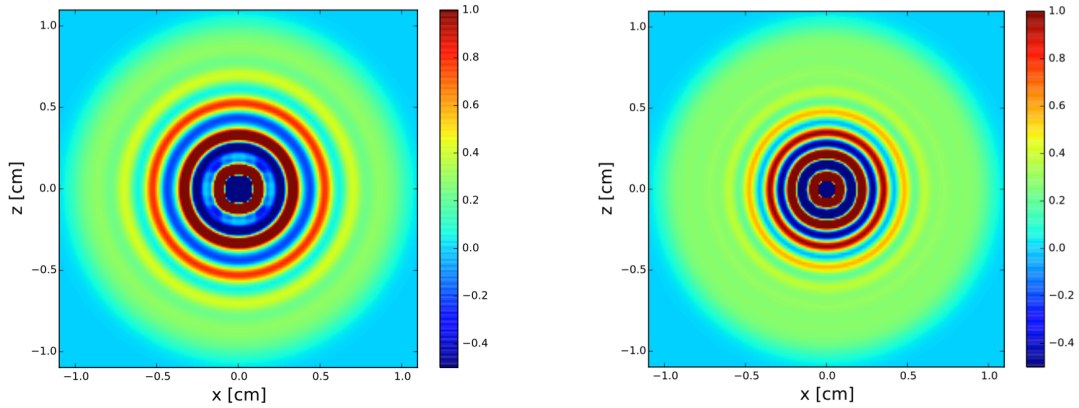

(a) D_{14} (b) P_{21}

Figure 4.1: 2D line source problem at $t = 1$ s with linear closures.

4.4.1 Line-source test problem

The line-source problem is tested again. As shown in Figures 3.12a and 3.12b, low order linear closures like P_N and D_N would produce notorious oscillations. Factually, simply increasing the order of linear closures does not ensure the convergence to transport solution, as illustrated in Figures 4.1b and 4.1a, which are for P_{21} and D_{14}. Graphically, with NFP_9 (see Figure 4.2a), the scalar flux agrees with transport solution in most part of the domain except around the wavefront that some oscillations occur. Increasing the order to 15 (see Figure 4.2b) gives more accurate results with a smeared wavefront, which seems to be due to the effects from low order time accuracy.

Figure 4.3 presents diagonal line-out plots for comparison. With increasing the orders, NFP_N presents consistent but increasingly more accurate results compared with the transport. It illustrates that it overcomes the difficulty of extending to high angular orders appearing in TP_N.

As described in Section 4.2.3, NFP_N would be robust in sense of tuning the coefficients c_N. Due to the definition of the NFP_N viscosity, it tends to vanish when radiation field

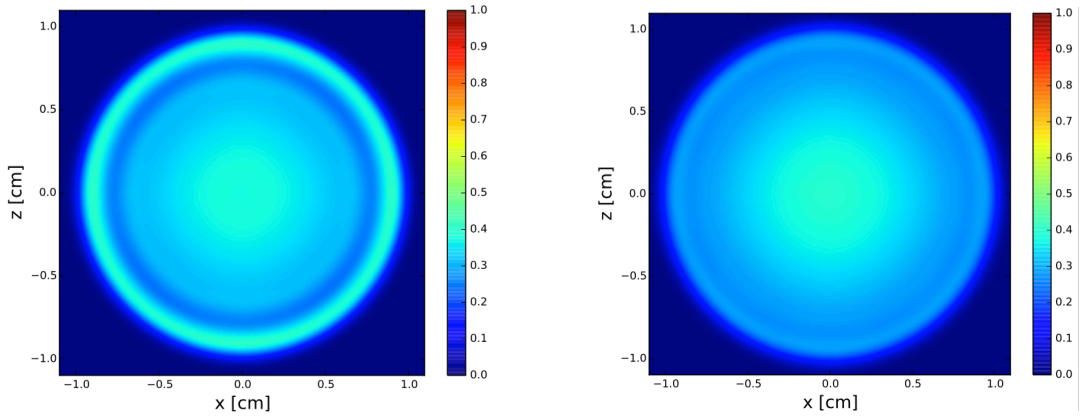

(a) NFP_9 (b) NFP_{15}

Figure 4.2: 2D line source problem at $t = 1$ s with NFP_N.

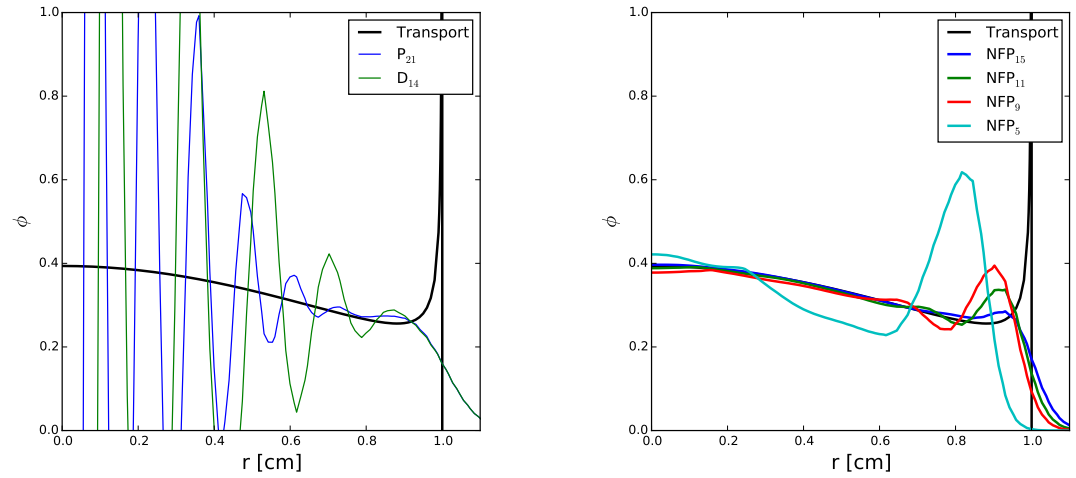

(a) P_{21} and D_{14}. (b) NFP_N.

Figure 4.3: Diagonal line-out plots.

varies slowly in time and space, which is the case for line-source problem when $t = 5$ s. Figure 4.4a gives an example of using tuned coefficients to obtain plausible solutions for both linear and nonlinear FP_N. As shown in Figure 4.4b, when increasing the properly tuned coefficients by 400% times, the solution from NFP_N is still acceptable, yet FP_N

presents the over-diffused solution.

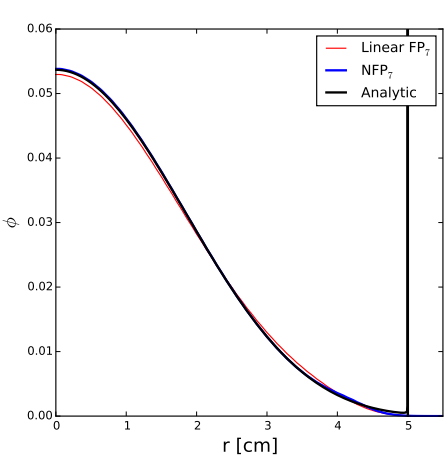

(a) Tuned strength.

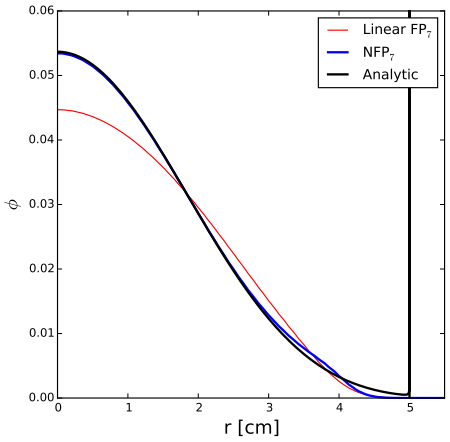

(b) Results comparison when increasing filtering strengths by 400%.

Figure 4.4: Line source problem results at $t = 5$ s.

4.4.2 Checkerboard problem

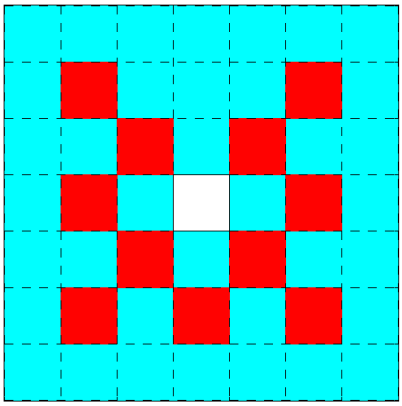

(a) Layout

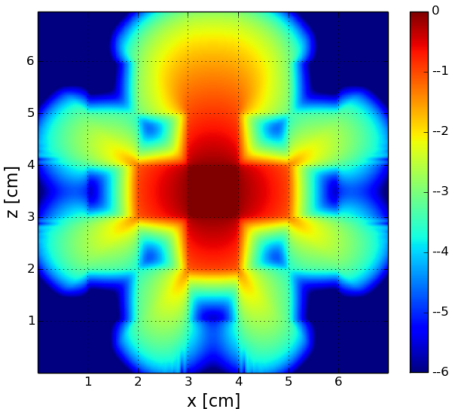

(b) S_{50} Reference solution

Figure 4.5: Checkerboard problem layout and reference solution at $t = 3.2$ s.

The checkerboard problem, which is from part of a reactor core[6], appears to be a challenge for angular discretization schemes. The white block in Figure 4.5a is with a strong absorber, the light blue blocks are thin scatterings and red blocks are absorbers[2]. When particles collide in scatterers and leak out into absorbers, “communication" between particles is shut down and particles stream, which forms angular discontinuity. On one hand, since particles lack collisions, ray effects manifest in S_N solutions (see Figures 4.6a and 4.6b). Even increasing S_N order to 50, rays can still be seen (e.g. around $x = 0$ and $z = 3.5$ in Figure 4.5b). On the other hand, P_N, as a spectral method in angle suffering from Gibbs phenomenon, produce negative solutions in the absorbers (see Figures 4.7a and 4.7b).

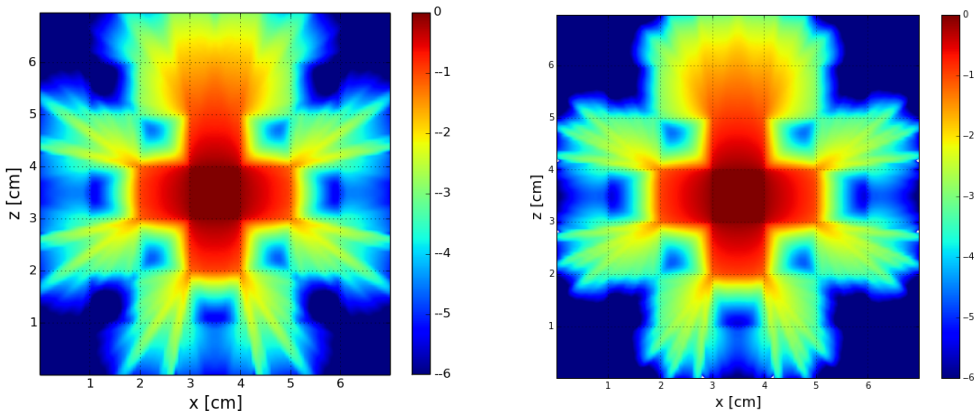

(a) S_8 (b) S_{12}

Figure 4.6: S_N solution for checkerboard problem.

Meanwhile the NFP_N gives good estimation of the scalar flux in the domain (Figure 4.8a and 4.8b). Particles going through absorbers are decoupled with other particles and solely stream forward. It then forms shadows in the absorbers and thusly the angular dis-

[2]Material properties are given in [6].

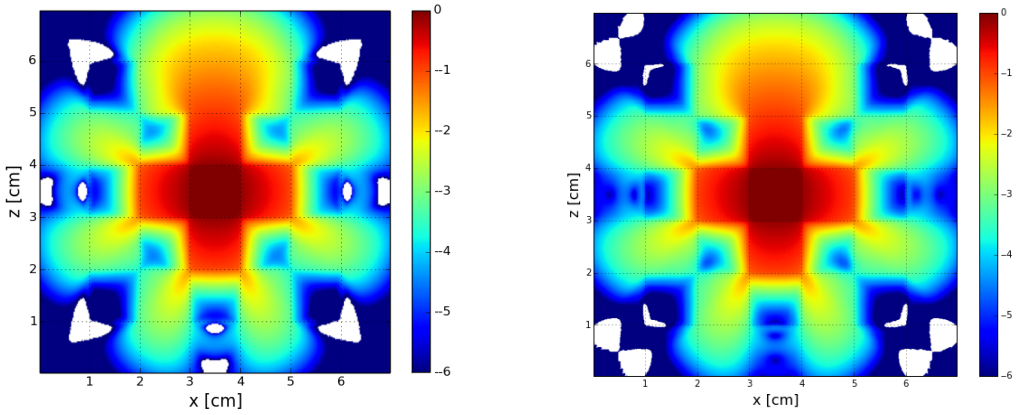

(a) P_7 (b) P_{11}

Figure 4.7: P_N solutions for checkerboard problem at $t = 3.2$ s.

continuity. In the NFP_N cases, adding proper amount of angular viscosity helps alleviate the solution and wipe out the negativities.

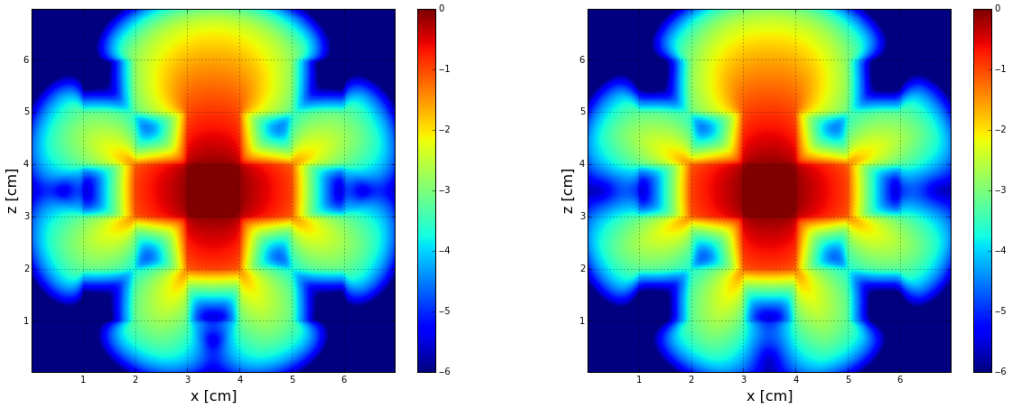

(a) NFP_7 (b) NFP_{11}

Figure 4.8: Checkerboard problem NFP_N solutions at $t = 3.2$ s. $k = 3$ and $c_N = 1$.

4.4.3 Simplified Hohlraum problem

When simulating radiative transfer, there exists interfaces between thin and thick materials. A simplified Hohlraum problem with thin scattering in the duct ($\sigma_{\mathrm{t}} = \sigma_{\mathrm{s}} = 0.1$) and thick material in walls and the central block ($\sigma_{\mathrm{t}} = 100,\ \sigma_{\mathrm{s}} = 30$) is used to test NFP$_N$ in such a situation. A unit isotropic incident boundary is imposed on the left side of the domain (see Figure 4.9a for the layout and 4.9b for a reference solution using S$_{60}$).

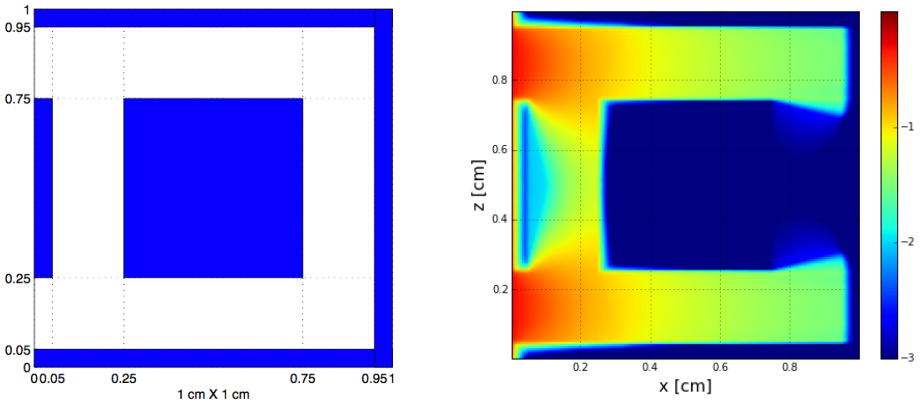

(a) Hohlraum layout (b) S$_{60}$

Figure 4.9: Simplified Hohlraum problem layout and reference solutions at $t = 2$ s.

Since radiation moves faster in the thin material (the duct) than in the thick material (the central block), it forms a shadow on the right side of the central block. Consequently, S$_N$ shows great ray-effects (Figures 4.11a and 4.11b). On the other hand, the shadow drags the radiation field obtained from P$_N$ to be negative. At the same time, P$_N$ solution presents negative scalar flux in both the duct and central block (see Figures 4.12a and 4.12b). Even increasing the order to 23 does not make the negative solution vanish (Figure 4.10).

As a comparison, we also present two result for NFP$_N$ with $N = 11$ (see Figure 4.13a) and $N = 17$ (see Figure 4.13b). With introducing the nonlinear filtering process, the

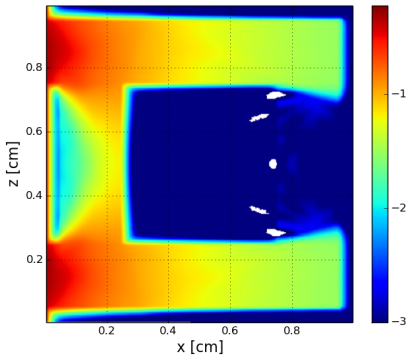

Figure 4.10: P_{23} solution for simplified Hohlraum problem

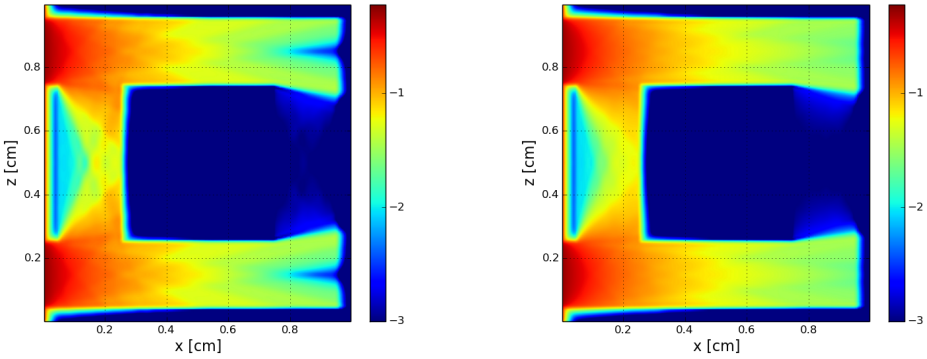

(a) S_{12} (b) S_{18}

Figure 4.11: S_N solution for simplified Hohlraum problem at $t = 2$ s.

negative solution existed in P_N is eliminated effectively.

Line-out plots are drawn in the duct and along the walls at $x = 0.25,\ 0.75$ and 0.95 cm as illustrated in Figures 4.14. NFP_N presents accurate and positive results in both cases. Positivity is crucial for the multi-physics prototype of this problem that P_N's negative radiation field crashed the simulation due to the induced negative material temperature[17]. We also notice that NFP_N is not flawless. It presents overshooting on the walls on the right hand side. It might be due to the over-diffusion from the viscosity overestimation that too much angular diffusion is added at certain spots so particles keep colliding therein. Yet,

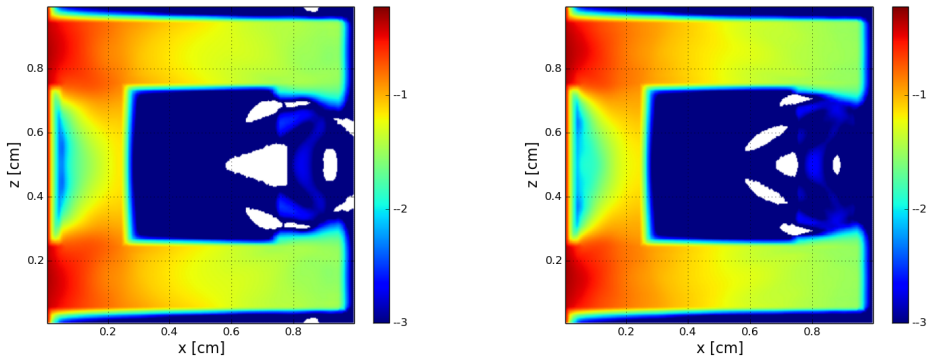

(a) P_{11} (b) P_{17}

Figure 4.12: P_N solution for simplified Hohlraum problem at $t = 2$ s.

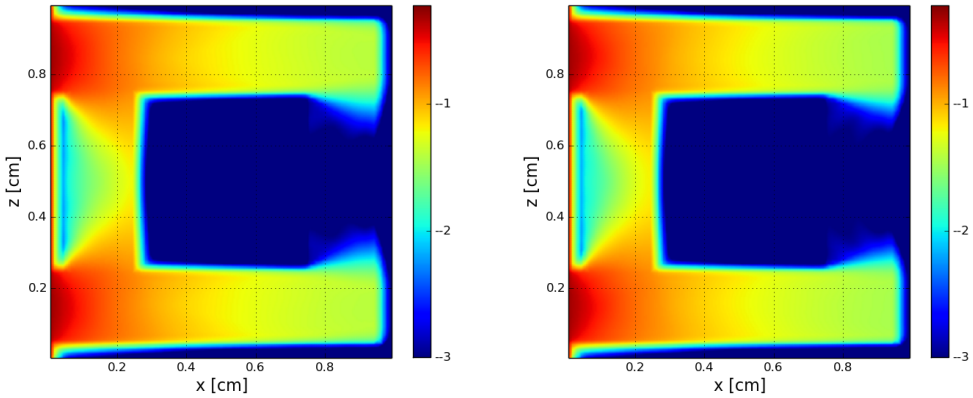

(a) NFP_{11} (b) NFP_{17}

Figure 4.13: NFP_N solution for simplified Hohlraum problem at $t = 2$ s.

unlike the negativity, increasing P_N order effectively removes that (See line-out plot for NFP_{17} in Section E.1).

4.5 Summary

In this section, we developed an nonlinear filtered spherical harmonics method for simulating radiation transport based on the nonlinear viscosity developed in Section 3. Overall, the nonlinear filtering method is promising that it somehow infer the filter strength

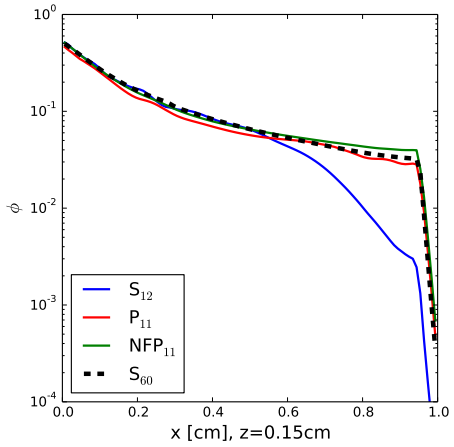

(a) Solutions along $z = 0.15$ cm

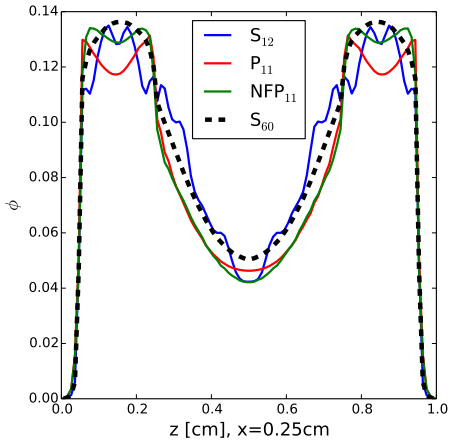

(b) Solutions along $x = 0.25$ cm

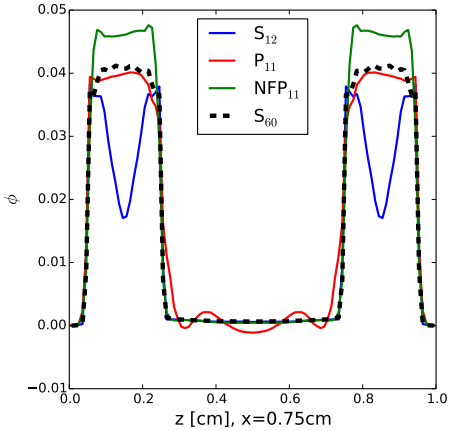

(c) Solutions along $x = 0.75$ cm

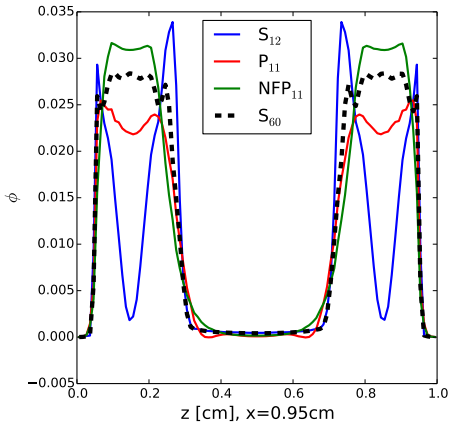

(d) Solutions along $x = 0.95$ cm

Figure 4.14: Line-out plots for Hohlraum problem.

in light of the solution. It shows effectiveness when solving the time-dependent transport equations.

Without touching the first moment, indeed, the NFP_N preserves the diffusion limit. Nevertheless, it does not claim the nonlinear filtering cannot be put into the first moment equation properly. In Section 5, we will present another NFP_N formulation for TRT problems and provide the proof for the statement of preserving the thick diffusion limit.

5. ASYMPTOTIC ANALYSIS OF NONLINEAR FILTERED P_N AND RADIATIVE TRANSFER APPLICATIONS

5.1 Introduction

In Section 4, we proposed a filtered spherical hamonics method. In this section, we first provide another formulation for the nonlinear filter. Thereafter, we will provide asymptotic analysis for linear FP_N, NFP_N proposed in Section 4 and the new formulation of NFP_N[1]. At last, we extend the NFP_N methods to radiative transfer with providing proper implicit time integration method.

5.2 Asymptotic Analysis for FP_1 Methods

5.2.1 FP_1 forms and scaling

When performing asymptotic analysis to FP_N, higher moments would not affect if the system preserves diffusion limit or not. Therefore, analysis on the FP_1 reflect the asymptotics of the methodology.

Generically, we can write the filtered P_1 system for gray radiation in 1D slab geometry as following:

$$\frac{1}{c}\frac{\partial \phi_0}{\partial t} + \frac{\partial \phi_1}{\partial x} + \sigma_{\mathrm{a}}\phi_0 = \sigma_{\mathrm{a}} acT^4, \tag{5.1a}$$

$$\frac{1}{c}\frac{\partial \phi_1}{\partial t} + \frac{1}{3}\frac{\partial \phi_0}{\partial x} + \left(\sigma_{\mathrm{a}} + \nu_1\right)\phi_1 = 0, \tag{5.1b}$$

$$C_v \frac{\partial T}{\partial t} = \sigma_{\mathrm{a}}(\phi_0 - acT^4), \tag{5.1c}$$

We follow the scaling developed for thermal radiative transfer by Morel[41]:

$$\frac{1}{c}\frac{\partial}{\partial t} \to \epsilon^2 \frac{1}{c}\frac{\partial}{\partial t} \quad \text{and} \quad \frac{\partial}{\partial x} \to \epsilon \frac{\partial}{\partial x}, \tag{5.2}$$

[1] We will name the NFP_N developed in Section 4 Type-I NFP_N and call the new formulation developed in this section Type-II NFP_N.

then the scaled system is expressed as:

$$\epsilon^2 \frac{1}{c}\frac{\partial \phi_0}{\partial t} + \epsilon \frac{\partial \phi_1}{\partial x} + \sigma_{\mathrm{a}}\phi_0 = \sigma_{\mathrm{a}} acT^4, \tag{5.3a}$$

$$\epsilon^2 \frac{1}{c}\frac{\partial \phi_1}{\partial t} + \epsilon \frac{1}{3}\frac{\partial \phi_0}{\partial x} + (\sigma_{\mathrm{a}} + \nu_1)\,\phi_1 = 0, \tag{5.3b}$$

$$\epsilon^2 C_v \frac{\partial T}{\partial t} = \sigma_{\mathrm{a}}(\phi_0 - acT^4), \tag{5.3c}$$

At the same time, a power expansion about ϵ to ϕ_0, ϕ_1, T and T^4 is performed, i.e.:

$$\phi_0 = \sum_{n=0}^{\infty} \phi_0^{(n)} \epsilon^n \tag{5.4}$$

$$\phi_1 = \sum_{n=0}^{\infty} \phi_1^{(n)} \epsilon^n \tag{5.5}$$

$$T = \sum_{n=0}^{\infty} T^{(n)} \epsilon^n \tag{5.6}$$

$$T^4 = \sum_{n=0}^{\infty} T^{4(n)} \epsilon^n \tag{5.7}$$

Note that coefficients in Eqs. (5.6) and (5.7) are clearly related, but we de-relate them until needed as suggested by Morel[47].

5.2.2 $\mathbf{P}_N$ and Type-I NFP$_N$

By substituting the expanded quantities in previous section into the scaled equations, we obtain a hierarchical set of equations with the expansion coefficients. In particular, the

$O(\epsilon^0)$ equations, with recognizing $\nu_1 = 0$, are:

$$\phi_0^{(0)} = acT^{4(0)} \tag{5.8a}$$

$$\sigma_{\mathrm{a}}\phi_1^{(0)} = 0 \tag{5.8b}$$

The $O(\epsilon)$ equations arising from Eq. (5.3) are:

$$\frac{\partial}{\partial x}\phi_1^{(0)} + \sigma_{\mathrm{a}}\phi_0^{(1)} = \sigma_{\mathrm{a}} acT^{4(1)} \tag{5.9a}$$

$$\phi_1^{(1)} = -\frac{1}{3\sigma_{\mathrm{a}}}\frac{\partial}{\partial x}\phi_0^{(0)} \tag{5.9b}$$

In fact, it is straightforward to see the similar property in $O(\epsilon^2)$ equations with similar procedure:

$$\phi_1^{(2)} = -\frac{1}{3\sigma_{\mathrm{a}}}\frac{\partial}{\partial x}\phi_0^{(1)} \tag{5.10}$$

That being said, P_1 and Type-I NFP_1 in time dependent TRT problem preserve thick diffusion limit up to $O(\epsilon^2)$. Further, since higher order moments does not affect diffusion limit, P_n with $\forall N > 1$ preserves thick diffusion limit.

5.2.3 Type-II NFP_N and asymptotic analysis

Avoiding tweaking first moment equation as in Type-I NFP_N does preserve thick diffusion limit. However, that does not necessarily state that no filtering can be incorporated in the first moment equation. Inspired by Larsen's flux limited diffusion, we propose a new angular viscosity as the following:

$$\nu_l = \sqrt{\sigma_{\mathrm{a}}^2 + \left(\nu_{l,\chi}\right)^2 + \left(\nu_{l,t}\right)^2} - \sigma_{\mathrm{a}}, \quad l = 1, \cdots, N, \tag{5.11}$$

where

$$\nu_{l,t} = c_N \left(l/N\right)^k \left| \frac{\partial_t \phi_0^0}{c\phi_0^0} \right| \tag{5.12}$$

and

$$\nu_{l,\chi} = c_N \left(l/N\right)^k \frac{\|\nabla \phi_0^0\|}{|\phi_0^0|} \tag{5.13}$$

Accordingly, the scaled viscosity is expressed as:

$$\nu_l = \sqrt{\sigma_{\mathrm{a}}^2 + \epsilon^2 \nu_{1,\chi}^2 + \epsilon^4 \nu_{1,t}^2} - \sigma_{\mathrm{a}} \tag{5.14}$$

Specifically for $l = 1$, we expand the scaled viscosity with Taylor series and obtain:

$$\nu_1 = -\frac{\epsilon^2}{2} \frac{\nu_{1,\chi}^2}{\sigma_{\mathrm{a}}} + O(\epsilon^4), \tag{5.15}$$

whence the viscosity is $O(\epsilon^2)$. Thereby, we then shall see the correct Fick's law for $O(\epsilon^1)$ equations, i.e.,

$$\phi_1^{(1)} = -\frac{1}{3\sigma_{\mathrm{a}}} \frac{\partial \phi_0^{(0)}}{\partial x} \tag{5.16}$$

In order to examine the diffusion limit to $O(\epsilon^2)$, we rewrite the scaled first moment equation and end up getting:

$$\phi_1 = -\frac{\epsilon^2 \partial_t \phi_1}{c\sqrt{\sigma_{\mathrm{a}}^2 + \epsilon^2 \nu_{1,\chi}^2 + \epsilon^4 \nu_{1,t}^2}} - \frac{\epsilon \partial_x \phi_0}{3\sqrt{\sigma_{\mathrm{a}}^2 + \epsilon^2 \nu_{1,\chi}^2 + \epsilon^4 \nu_{1,t}^2}} \tag{5.17}$$

Expand the square root with Taylor-series, we find:

$$\phi_1 = -\frac{\epsilon^2\left(1+\frac{\epsilon^2\nu_{1,\chi}}{2\sigma_{\mathrm{a}}}+O(\epsilon^4)\right)}{c\sigma_{\mathrm{a}}}\partial_t\phi_1 - \frac{\epsilon\left(1+\frac{\epsilon^2\nu_{1,\chi}}{2\sigma_{\mathrm{a}}}+O(\epsilon^4)\right)}{3\sigma_{\mathrm{a}}}\partial_x\phi_0 \tag{5.18}$$

Then for $O(\epsilon^2)$, we obtain:

$$\phi_1^{(2)} = -\frac{1}{3\sigma_{\mathrm{a}}}\frac{\partial\phi_0^{(1)}}{\partial x} \tag{5.19}$$

Consequently, the Type-II NFP$_1$ preserves thick diffusion limit up to $O(\epsilon^2)$ and so does Type-I NFP$_N$, $\forall N > 1$.

Why $\nu_1 = 0$ in Type-I NFP$_N$

Following the procedure above, one will derive the following with $O(\epsilon^2)$ equations:

$$\phi_1^{(2)} = -\frac{1}{3\sigma_{\mathrm{a}}}\frac{\partial\phi_0^{(1)}}{\partial x} + \frac{\nu_{1,\chi}}{3\sigma_{\mathrm{a}}^2}\frac{\partial\phi_0^{(0)}}{\partial x},$$

which states that Type-I NFP$_N$ will not preserve diffusion limit to $O(\epsilon^2)$ with nonzero ν_1.

5.3 A Fully Implicit Solver

Section 3 and 4 employ a semi-implicit time integrator for solving linear transport equation. However, when solving TRT problems, nonlinearly, a fully implicit solver is favored, especially for where there is a thin-thick contact interface that cross sections may vary by many orders. We then present a Newton-Picard iterative scheme for solving the NFP$_N$ equations in TRT.

5.3.1 Fully implicit scheme

Let us denote the NFP$_N$ for multi-D TRT problems by the following:

$$\frac{1}{c}\frac{\partial\vec{\phi}}{\partial t} + \nabla\cdot\vec{F} + (\sigma_{\mathrm{a}} + \mathbf{D})\,\vec{\phi} = \vec{Q}(T^4) \tag{5.20a}$$

$$C_v\frac{\partial T}{\partial t} = \sigma_{\mathrm{a}}\left(\sqrt{4\pi}\phi_0^0 - acT^4\right), \tag{5.20b}$$

where

$$\mathbf{D} = \mathbf{D}\left(\sigma_{\mathrm{a}}(T), \frac{\partial\phi_0^0}{\partial t}, \nabla\phi_0^0\right) \quad \text{and} \quad \vec{Q}(T^4) = \left(\frac{acT^4}{\sqrt{4\pi}}, 0, \cdots, 0\right)^{\top} \tag{5.21}$$

A backward Euler time stepping method for unknowns at Step n ($n = 1, \cdots$) can then easily formulated as:

$$\frac{1}{c}\frac{\vec{\phi}_n}{\Delta t} + \nabla\cdot\vec{F}_n + (\sigma_{\mathrm{a}n} + \mathbf{D}_n)\,\vec{\phi} = \vec{Q}({T^4}_n) + \frac{1}{c}\frac{\vec{\phi}_{n-1}}{\Delta t} \tag{5.22a}$$

$$C_v\frac{T^n}{\Delta t} = \sigma_{\mathrm{a}n}\left(\sqrt{4\pi}\phi_{0n}^0 - ac{T^4}_n\right) + C_v\frac{T_{n-1}}{\Delta t}, \tag{5.22b}$$

Newton's method is used for treating the emission source $\vec{Q}(T^4)$. The details can be found in [41]. For every Newton iteration l, the viscosity are approximated as:

$$\left(\frac{1}{c}\frac{\partial_t\phi_0^0}{\phi_0^0}\right)_n \approx \frac{\phi_0^{0^l} - \phi_{0n-1}^0}{\Delta t\phi_0^{0^l}} \quad \text{and} \quad \left(\frac{\|\nabla\phi_0^0\|}{\phi_0^0}\right)_n \approx \frac{\|\nabla\phi_0^{0^l}\|}{\phi_0^{0^l}} \tag{5.23}$$

5.4 Numerics

5.4.1 2D Marshak wave problem

We provide test results for the 2D variation of Marshak wave problem as a demonstration for the fully implicit solver. The cross section $\sigma_{\mathrm{a}} = \sigma_{\mathrm{t}} = 10/T^3$ (cm^{-1}) with T in

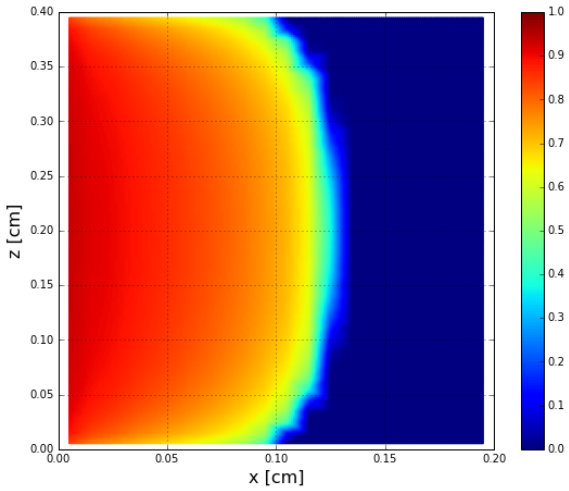

Figure 5.1: P_3 T_{rad} distribution at 1 ns in 2D Marshak problem.

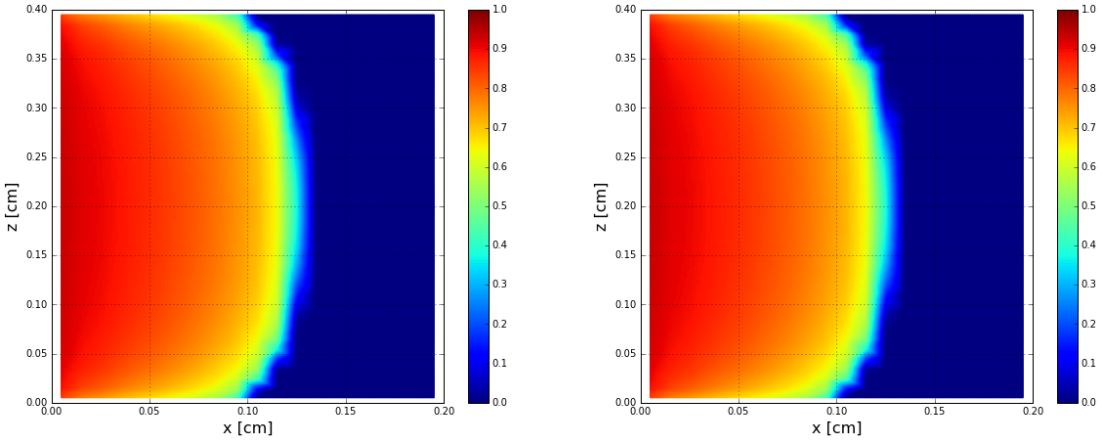

(a) Type-I NFP_3 (b) Type-II NFP_3

Figure 5.2: 2D Marshak test at $t = 1$ ns.

units of keV. And the heat capacity $C_v = 0.3$ GJ/cm^3-keV. Since the solution is diffusive, P_N can also be used in the simulation. To ensure stability $\Delta x = 0.01$ cm with $\Delta t = \Delta x/c$. In such a calculation, the cross section around the cold-hot contact interface can vary over 8 orders. In both NFP_N calculations, $c_N = 0.5$ and a upper bound of $50\sigma_{\text{t}}$ is set for the limiters.

We examine the material temperature T_{mat} and radiation temperature $T_{\text{rad}} = (\phi/ac)^{1/4}$. For P_3 (Figure 5.1) and two NFP_3 (see Figure 5.2). With the line-outs in Figure 5.3, we clearly see agreements of all methods for both quantities of interest. The results demonstrate that both types of NFP_N preserves thick diffusion limit as predicted in the analysis.

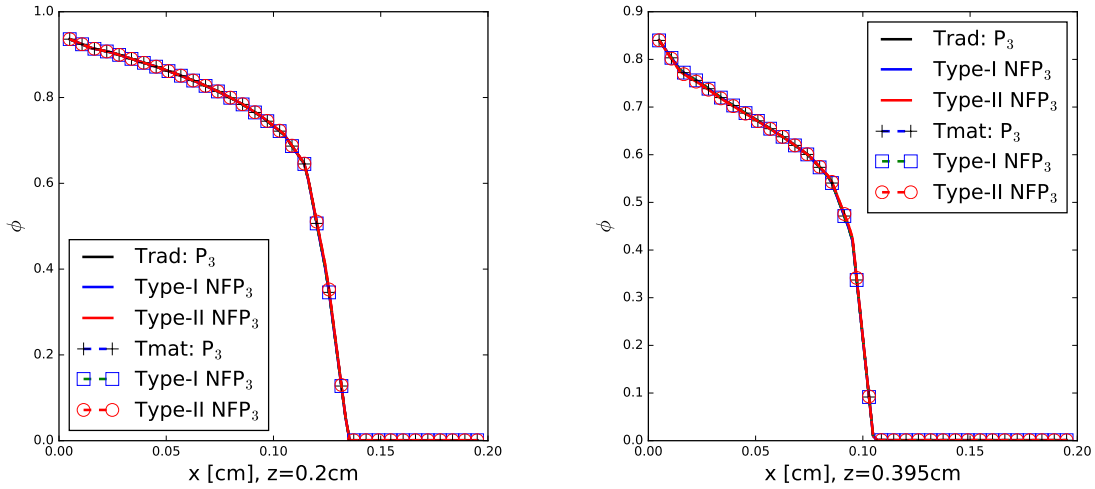

(a) Line-outs in the center

(b) Line-outs around upper boundary

Figure 5.3: 2D Marshak test line-outs at $t = 1$ ns.

6. LEAST-SQUARES TRANSPORT AND SELF-ADJOINT ANGULAR FLUX EQUATIONS AND DISCRETIZATIONS

6.1 Introduction

Previous sections focus on angular discretization using spherical harmonics for time-dependent radiation transport. In this section, we will focus on spatial discretization of steady-state neutron transport equation.

Since the Boltzmann transport equation is a first-order PDE in space, the continuous finite element method (CFEM) cannot be directly used without special stabilization treatment. Though the discontinuous finite element method (DFEM) has been widely used to solve the transport equation, it has some known or not-so-well-known drawbacks. Besides the higher DoF count than CFEM, it has the difficulty of efficiently performing sweeps with unstructured meshes[23].

In order to make use of CFEM, a common approach is to cast the first-order transport equation to a second-order PDE. Well known examples include the even parity equation[24, 23, 57] and self-adjoint equations[1][25, 23]. More recently, Hansen, et al. derived a second-order form by multiplying transport residual by the adjoint transport operator[26].

On the other hand, one could employ the least-squares finite element method (LSFEM) using continuous basis functions with or without a $1/\sigma_{\mathrm{t}}$ weighting. By defining a (weighted) least-squares (LS) transport residual functional in discrete function space and minimizing the functional, one obtains the (weighted) LS the formulation. Such least-squares formulations resemble the CFEM discretization to the second-order forms mentioned above, which can be demonstrated by simply manipulating the weak form.

In this section, we will first derive the CFEM discretization to SAAF and LSTE. There-

[1]There are two forms of self-adjoint equations. The one used in this dissertation is the source iteration compatible form.

after we derive discretization of first-order transport equation with reciprocal cross section weighted and unweighted least-squares finite element and illustrate the equivalence to CFEM-SAAF and CFEM-LSTE, respectively.

6.2 CFEM Disretizations

The second-order forms of transport equations can be discretized with CFEM due to the symmetrization of the streaming operator into a directional Laplacian operator. We will derive the CFEM derivation specifically for LSTE and SAAF in this section.

6.2.1 CFEM-LSTE

Hansen, et al. derived the LSTE by multiplying the transport equation by the adjoint transport operator, i.e.:

$$\mathcal{L}^{\dagger}\mathcal{L}\psi = \mathcal{L}^{\dagger}\left(\mathcal{S}\psi + \frac{Q}{4\pi}\right) \tag{6.1}$$

Discretizing such an equation with CFEM is equivalent to finding the solution ψ in finite element space $\mathcal{V}$, such that $\forall v \in \mathcal{V}$, the following weak form holds:

$$\int_{\mathcal{D}} d\vec{r}\, v\mathcal{L}^{\dagger}\mathcal{L}\psi = \int_{\mathcal{D}} d\vec{r}\, v\mathcal{L}^{\dagger}\left(\mathcal{S}\psi + \frac{Q}{4\pi}\right). \tag{6.2}$$

With adjoint properties, such a weak form can be re-expressed as:

$$\int_{4\pi} d\Omega \int_{\mathcal{D}} d\vec{r}\, \mathcal{L}v\mathcal{L}\psi + \int_{4\pi} d\Omega \int_{\partial\mathcal{D}} ds\, \vec{n}\cdot\vec{\Omega}v\left(\mathcal{L}\psi - \left(\mathcal{S}\psi + \frac{Q}{4\pi}\right)\right) = \int_{4\pi} d\Omega \int_{\mathcal{D}} d\vec{r}\, \mathcal{L}v\left(\mathcal{S}\psi + \frac{Q}{4\pi}\right), \tag{6.3}$$

Requiring transport equation to be fulfilled, i.e. $\mathcal{L}\psi - \left(\mathcal{S}\psi + \frac{Q}{4\pi}\right) = 0$, on the boundary

leads to the interior weak form[2]:

$$\int_{4\pi} d\Omega \int_{\mathcal{D}} d\vec{r}\, \mathcal{L}v\mathcal{L}\psi = \int_{4\pi} d\Omega \int_{\mathcal{D}} d\vec{r}\, \mathcal{L}v \left(\mathcal{S}\psi + \frac{Q}{4\pi} \right). \tag{6.4}$$

Unfortunately, there is no direct way imposing an incident boundary condition. Zhang applied strong boundary condition in a radiative transfer work[57]. More recently, a weak boundary condition from penalty method is proposed, with which the least-squares formulation resembles CFEM-SAAF in non-void homogeneous problems[58]. In this work, we will use this weak boundary condition for solving LSTE:

$$\begin{aligned} &\int_{4\pi} d\Omega \int_{\mathcal{D}} d\vec{r}\, \mathcal{L}v\mathcal{L}\psi + \int_{\vec{n}\cdot\vec{\Omega}<0} d\Omega \int_{\partial\mathcal{D}} ds\, \sigma_{\mathrm{t}} \left| \vec{n}\cdot\vec{\Omega} \right| v\psi = \\ &\int_{4\pi} d\Omega \int_{\mathcal{D}} d\vec{r}\, \mathcal{L}v \left(\mathcal{S}\psi + \frac{Q}{4\pi} \right) + \int_{\vec{n}\cdot\vec{\Omega}<0} d\Omega \int_{\partial\mathcal{D}} ds\, \sigma_{\mathrm{t}} \left| \vec{n}\cdot\vec{\Omega} \right| v\psi^{\mathrm{inc}}. \end{aligned} \tag{6.5}$$

6.2.2 CFEM-SAAF

For a specific discrete function space $\mathcal{V}$, using CFEM to solve SAAF is equivalent to finding solution $\psi \in \mathcal{V}$, such that $\forall v \in \mathcal{V}$, we have

$$\begin{aligned} &\int_{\mathcal{D}} d\vec{r} \int_{4\pi} d\Omega\, v \left(-\vec{\Omega}\cdot\nabla\frac{1}{\sigma_{\mathrm{t}}}\vec{\Omega}\cdot\nabla\psi + \sigma_{\mathrm{t}}\psi \right) \\ &= \int_{\mathcal{D}} d\vec{r} \int_{4\pi} d\Omega\, v \left(\left(\mathcal{S}\psi + \frac{Q}{4\pi} \right) - \vec{\Omega}\cdot\nabla\frac{S\psi + q}{\sigma_{\mathrm{t}}} \right), \end{aligned} \tag{6.6}$$

[2]For CFEM-LSTE $\mathcal{S}\psi$ will be treated as source to be compatible with source iteration with S_N calculations. We then prefer to put $\mathcal{S}\psi$ in the linear form on right hand side.

by performing integration by part, and recognizing $\frac{-\vec{\Omega}\cdot\nabla\psi+\mathcal{S}\psi+\frac{Q}{4\pi}}{\sigma_{\mathrm{t}}} = \psi$ on boundary, we approach:

$$\int_{4\pi} d\Omega \int_{\mathcal{D}} d\vec{r} \left(\vec{\Omega}\cdot\nabla v\frac{1}{\sigma_{\mathrm{t}}}\vec{\Omega}\cdot\nabla\psi + \sigma_{\mathrm{t}} v\psi\right) + \int_{4\pi} d\Omega \int_{\partial\mathcal{D}} ds\, \vec{n}\cdot\vec{\Omega} v\psi$$
$$= \int_{\vec{n}\cdot\vec{\Omega}<0} d\Omega \int_{\partial\mathcal{D}} ds \left(v\left(\mathcal{S}\psi + \frac{Q}{4\pi}\right) + \vec{\Omega}\cdot\nabla v\frac{\mathcal{S}\psi+\frac{Q}{4\pi}}{\sigma_{\mathrm{t}}}\right). \tag{6.7}$$

With the boundary condition in Eq. (2.2), we would transform the weak formulation into the following form[3]:

$$\int_{\mathcal{D}} d\vec{r} \int_{4\pi} d\Omega \left(\vec{\Omega}\cdot\nabla v\frac{\vec{\Omega}\cdot\nabla\psi - \mathcal{S}\psi}{\sigma_{\mathrm{t}}} + v\left(\sigma_{\mathrm{t}}\psi - \mathcal{S}\psi\right)\right) + \int_{\partial\mathcal{D}} ds \int_{\vec{n}\cdot\vec{\Omega}>0} \vec{n}\cdot\vec{\Omega} v\psi$$
$$= \int_{\mathcal{D}} d\vec{r} \int_{4\pi} d\Omega \left(vq + \vec{\Omega}\cdot\nabla v\frac{q}{\sigma_{\mathrm{t}}}\right) + \int_{\partial\mathcal{D}} ds \int_{\vec{n}\cdot\vec{\Omega}<0} \vec{n}\cdot\vec{\Omega} v\psi^{\mathrm{inc}} \tag{6.8}$$

6.3 (Weighted) Least-Squares Finite Element Discretization

6.3.1 Unweighted least-squares finite element discretization

Least-squares discretization of PDEs starts off defining proper least-squares functionals with a proper trial space. Suppose we have a trial space $\mathcal{V}$ with a function ψ spanned by basis in $\mathcal{V}$. Then the least-square functional could be defined as:

$$\Gamma_{\mathrm{LS}} = \int_{4\pi} d\Omega \int_{\mathcal{D}} d\vec{r}\, \left(\mathcal{L}\psi - q_{\mathrm{s}}\right)^2 + \int_{\vec{n}\cdot\vec{\Omega}<0} d\Omega \int_{\partial\mathcal{D}} ds\, \sigma_{\mathrm{t}} \left|\vec{n}\cdot\vec{\Omega}\right| \left(\psi - \psi^{\mathrm{inc}}\right)^2, \tag{6.9}$$

[3]We prefer to put the $\mathcal{S}\psi$ in the bilinear form of CFEM-SAAF since we would use both S_N and P_N angular discretizations on this weak form.

where $q_{\mathrm{s}} = \mathcal{S}\psi + \frac{Q}{4\pi}$. Minimizing such a functional in $\mathcal{V}$ leads to the weak formulation: finding ψ in $\mathcal{V}$, such that $\forall v \in \mathcal{V}$, the following equation holds:

$$\int_{4\pi} d\Omega \int_{\mathcal{D}} d\vec{r}\, \mathcal{L}v\mathcal{L}\psi + \int_{\vec{n}\cdot\vec{\Omega}<0} d\Omega \int_{\partial\mathcal{D}} ds\, \sigma_{\mathrm{t}} \left|\vec{n}\cdot\vec{\Omega}\right| v\psi =$$
$$\int_{4\pi} d\Omega \int_{\mathcal{D}} d\vec{r}\, \mathcal{L}v \left(\mathcal{S}\psi + \frac{Q}{4\pi}\right) + \int_{\vec{n}\cdot\vec{\Omega}<0} d\Omega \int_{\partial\mathcal{D}} ds\, \sigma_{\mathrm{t}} \left|\vec{n}\cdot\vec{\Omega}\right| v\psi^{\mathrm{inc}}. \tag{6.10}$$

Equation (6.10) is identical to (6.5), i.e. solving transport equation using least-squares finite element is identical to solving CFEM-LSTE.

6.3.2 Weighted least-squares (WLS) finite element discretization

Similar to least-squares, we define a least-squares functional weighted by $1/\sigma_{\mathrm{t}}$:

$$\Gamma_{\mathrm{WLS}} = \int_{4\pi} d\Omega \int_{\mathcal{D}} d\vec{r}\, \frac{1}{\sigma_{\mathrm{t}}} \left(\mathcal{L}\psi - q_{\mathrm{s}}\right)^2 + \int_{\vec{n}\cdot\vec{\Omega}<0} d\Omega \int_{\partial\mathcal{D}} ds\, \left|\vec{n}\cdot\vec{\Omega}\right| \left(\psi - \psi^{\mathrm{inc}}\right)^2. \tag{6.11}$$

Consequently, we obtained another least-squares weak formulation after minimizing the functional above:

$$\int_{4\pi} d\Omega \int_{\mathcal{D}} d\vec{r}\, \mathcal{L}v\frac{1}{\sigma_{\mathrm{t}}}\mathcal{L}\psi + \int_{\vec{n}\cdot\vec{\Omega}<0} d\Omega \int_{\partial\mathcal{D}} ds\, \left|\vec{n}\cdot\vec{\Omega}\right| v\psi =$$
$$\int_{4\pi} d\Omega \int_{\mathcal{D}} d\vec{r}\, \mathcal{L}v\frac{\left(\mathcal{S}\psi + \frac{Q}{4\pi}\right)}{\sigma_{\mathrm{t}}} + \int_{\vec{n}\cdot\vec{\Omega}<0} d\Omega \int_{\partial\mathcal{D}} ds\, \left|\vec{n}\cdot\vec{\Omega}\right| v\psi^{\mathrm{inc}}. \tag{6.12}$$

In addition, it is straightforward to demonstrate the resulting weak form is identical to

CFEM-SAAF. By expanding $\mathcal{L}$, Eq. (6.12) is transformed into:

$$\underline{\int_{4\pi} d\Omega \int_{\mathcal{D}} d\vec{r} \left(\vec{\Omega}\cdot\nabla v + \sigma_{\mathrm{t}} v\right) \frac{1}{\sigma_{\mathrm{t}}} \left(\vec{\Omega}\cdot\nabla\psi + \sigma_{\mathrm{t}}\psi\right) + \int_{\vec{n}\cdot\vec{\Omega}<0} d\Omega \int_{\partial\mathcal{D}} ds \left|\vec{n}\cdot\vec{\Omega}\right| v\psi} = \int_{4\pi} d\Omega \int_{\mathcal{D}} d\vec{r} \left(\vec{\Omega}\cdot\nabla v + \sigma_{\mathrm{t}} v\right) \frac{\left(\mathcal{S}\psi + \frac{Q}{4\pi}\right)}{\sigma_{\mathrm{t}}} + \int_{\vec{n}\cdot\vec{\Omega}<0} d\Omega \int_{\partial\mathcal{D}} ds \left|\vec{n}\cdot\vec{\Omega}\right| v\psi^{\mathrm{inc}}. \tag{6.13}$$

Recognize that further expansion with integration by part would transform the Eq. (6.13) to:

$$\begin{aligned} &\int_{4\pi} d\Omega \int_{\mathcal{D}} d\vec{r} \left(\vec{\Omega}\cdot\nabla v \frac{1}{\sigma_{\mathrm{t}}} \vec{\Omega}\cdot\nabla\psi + v\sigma_{\mathrm{t}}\psi\right) \\ &\underline{+ \int_{4\pi} d\Omega \int_{\partial\mathcal{D}} ds\, \vec{n}\cdot\vec{\Omega} v\psi + \int_{\vec{n}\cdot\vec{\Omega}<0} d\Omega \int_{\partial\mathcal{D}} ds \left|\vec{n}\cdot\vec{\Omega}\right| v\psi} = \\ &\int_{4\pi} d\Omega \int_{\mathcal{D}} d\vec{r} \left(\vec{\Omega}\cdot\nabla v + \sigma_{\mathrm{t}} v\right) \frac{\left(\mathcal{S}\psi + \frac{Q}{4\pi}\right)}{\sigma_{\mathrm{t}}} + \int_{\vec{n}\cdot\vec{\Omega}<0} d\Omega \int_{\partial\mathcal{D}} ds \left|\vec{n}\cdot\vec{\Omega}\right| v\psi^{\mathrm{inc}}. \end{aligned} \tag{6.14}$$

Cancel the incoming part of the underlined integrals, we obtain:

$$\begin{aligned} &\int_{4\pi} d\Omega \int_{\mathcal{D}} d\vec{r} \left(\vec{\Omega}\cdot\nabla v \frac{\vec{\Omega}\cdot\nabla\psi - \mathcal{S}\psi}{\sigma_{\mathrm{t}}} + v\left(\sigma_{\mathrm{t}}\psi - \mathcal{S}\psi\right)\right) + \int_{\vec{n}\cdot\vec{\Omega}>0} d\Omega \int_{\partial\mathcal{D}} ds\, \vec{n}\cdot\vec{\Omega} v\psi \\ &= \int_{4\pi} d\Omega \int_{\mathcal{D}} d\vec{r} \left(vq + \vec{\Omega}\cdot\nabla v \frac{q}{\sigma_{\mathrm{t}}}\right) + \int_{\vec{n}\cdot\vec{\Omega}<0} d\Omega \int_{\partial\mathcal{D}} ds \left|\vec{n}\cdot\vec{\Omega}\right| v\psi^{\mathrm{inc}}, \end{aligned} \tag{6.15}$$

That being said, solving transport equation with $1/\sigma_{\mathrm{t}}$-weighted least-squares finite element is identical to solving SAAF using CFEM.

6.4 Summary

The main contribution in this section is that we illustrate the resemblances between

CFEM discretizing second-order forms and solving transport equation using (weighted) least-squares finite element method. Deriving least-squares like methods from minimizing functionals forms the basis for the following sections in this dissertation.

7. RELAXED L_1 FINITE ELEMENT METHOD FOR SOLVING NEUTRONICS PROBLEMS

7.1 Introduction

In Section 6, we derived least-squares finite element methods solving neutron transport equation. While it can be equipped with continuous basis, difficulty still arises in certain situations. In general dimensions, with under resolved mesh, problems with strong absorber can induce oscillations and thusly negative solutions[59, 60]. Moreover, in multi-D situations, void or near-void situations can also induce negativity, even for first order transport with DFEM[61]. Even without oscillations, void can induce low accuracy of the least-squares method. Yet, in real-world problems, like shielding problems, those situations are usual and inevitable, which inspires the development of other methods.

For least-squares method, one of causes of the oscillations is that the L_2 norm of transport residual overestimates the contribution from large residual components. Like least-squares fitting in data analysis, when trying to fit every single data point, the fitting principle would overweight the contribution from outliers, leading to erroneous and oscillatory results[29, 28].

One of the remedies is to introduce other norms of the transport residual. Previously, Jiang developed the iteratively reweighted least-squares (IRLS) method for linear advection[28]. The prototypical IRLS is to use some power of the inverse residual as the weight for least-squares method. For simplicity the sum of solution change to some power in each cell is used instead. The rationale behind it is that such a method would resemble L_1 norm induced method. For discontinuous boundary condition, such a method is extremely accurate in interior of the domain. However, Lowrie et al.[62] found that IRLS does not propagate information properly so that if the incident boundary condition is smooth, IRLS

can give erroneous results that large gradients of the solution can be mistakenly treated as discontinuity. Lowrie demonstrated the IRLS is not a L_1 method, which is thereafter assigned to the cause of erroneous results for problems with smooth solutions.

In a more recent work, by developing efficient nonlinear solving techniques, Guermond approximated the L_1 solution for several problems in fluid dynamics[30]. The L_1 method is demonstrated to be accurate in problems where least-squares has difficulty and can well interpret smooth solution in contrast to Lowrie's findings about IRLS[62].

Inspired by Guermond, in this section, we introduce a relaxed L_1 method for solving neutron transport equations. Such a method is designed to be a relaxed version of L_1 method in the sense that L_1 finite element will be used only when point residual becomes higher than certain criteria otherwise the least-squares method is used. Essentially, it is equivalent to adding L_1 regularization to a least-squares method. Additionally, accounting for the presence of scattering, the scheme is designed to be compatible with source iteration and acceleration techniques like diffusion synthetic acceleration (DSA)[63].

7.2 Derivation in L_1 Norm

7.2.1 Smoothed L_1 norm and L_1 finite element

The derivation starts off defining the following functional as L_1 norm of transport residual $R = \mathcal{L}\psi - q_{\mathrm{s}}$:

$$\Gamma_{\mathrm{L}_1}(\psi) = \int_{4\pi} d\Omega \int_{\mathcal{D}} d\vec{r}\, |R(\psi)| \tag{7.1}$$

A suitable finite element method would be developed by minimizing the functional above. As introduced in Section 6, we introduce a small perturbation ϵv, we obtained a perturbed

functional:

$$\Gamma_{\mathrm{L}_1}(\psi + \epsilon v) = \int\limits_{4\pi} d\Omega \int\limits_{\mathcal{D}} d\vec{r}\, |R(\psi + \epsilon v)| \tag{7.2}$$

However, the functional is not differentiable at the points where $R = 0$. To overcome the non-differentiation, Guermond[30] introduced a replacement of the functional equipped with a quite complex nonlinear solving method. On the other hand, Zheng and McClarren[60, 59] derived the L_1 functional with a smoothed substitution, which is quite straightforward.

For arbitrary small number ζ, one should recognize the approximation:

$$|R| \approx \sqrt{R^2 + \zeta^2} \tag{7.3}$$

Figure 7.1 shows the example illustrating the smoothing effects brought by the approximation for different values of ζ. With decreasing ζ, $\sqrt{x^2 + \zeta^2}$ converges to $|x|$ rapidly. What can be expected is with ζ goes to zero, $\sqrt{x^2 + \zeta^2}$ has the limit of $|x|$.

Introduce Eq. (7.3) back into (7.2) and then we obtain a differentiable approximation perturbed L_1 norm functional:

$$\Gamma_{\mathrm{L}_1}(\psi + \epsilon v) \approx \int\limits_{4\pi} d\Omega \int\limits_{\mathcal{D}} d\vec{r}\, \sqrt{R(\psi + \epsilon v)^2 + \zeta^2} \tag{7.4}$$

To minimize the functional, we expect the first derivative to be zero, i.e.

$$\lim_{\epsilon \to 0} \frac{\partial \Gamma_{\mathrm{L}_1}}{\partial \epsilon} = \int\limits_{4\pi} d\Omega \int\limits_{\mathcal{D}} d\vec{r}\, \frac{\mathcal{L}v(\mathcal{L}\psi - q_{\mathrm{s}})}{\sqrt{R^2 + \zeta^2}} = 0 \tag{7.5}$$

Taking the limit $\zeta \to 0$, the smoothed L_1 expression approaches the L_1 weak formulation

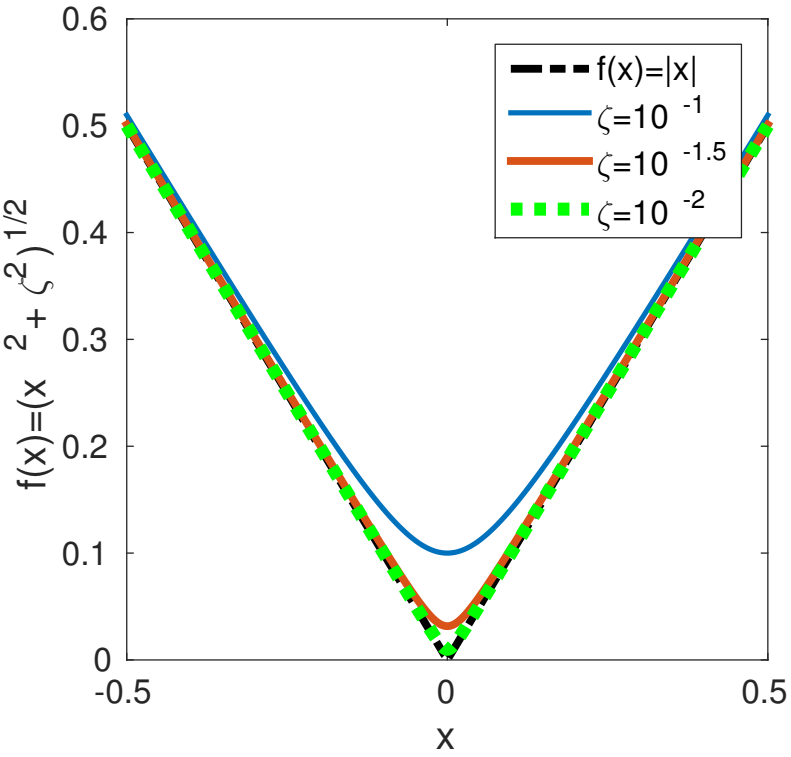

Figure 7.1: $\sqrt{x^2+\zeta^2}$ vs $|x|$ for different ζ values.

as $\sqrt{R^2+\zeta^2} \to |R|$:

$$\int_{4\pi} d\Omega \int_{\mathcal{D}} d\vec{r}\, \frac{\mathcal{L}v(\mathcal{L}\psi - (\mathcal{S}\psi + \frac{Q}{4\pi}))}{|R|} = 0, \tag{7.6}$$

or equivalently,

$$\int_{4\pi} d\Omega \int_{\mathcal{D}} d\vec{r}\, \frac{\mathcal{L}v\mathcal{L}\psi}{|R|} = \int_{4\pi} d\Omega \int_{\mathcal{D}} d\vec{r}\, \frac{\mathcal{L}v\,(\mathcal{S}\psi + \frac{Q}{4\pi})}{|R|}. \tag{7.7}$$

Apparently, solving the weak formulation requires evaluation of residual, which is calculated with the solutions. Thus, the L_1 finite element method is nonlinear.

7.2.2 A L_1 boundary condition

In 1D applications, least-squares weak boundary is used. However, in multi-D calculations, such a boundary condition causes stability problems for incident boundaries. A hypothesis is the norms measuring residuals on boundary and interiors should be consistent. Hence, developing an appropriate boundary condition is a necessity.

Similar to the interior functional, we can define a L_1 boundary functional on boundary, namely

$$\Gamma_{b,\mathrm{L}_1} = \int\limits_{\vec{n}\cdot\vec{\Omega}<0} d\Omega \int\limits_{\partial\mathcal{D}} ds\ \lambda \left|\vec{n}\cdot\vec{\Omega}\right| \left|\psi - \psi^{\mathrm{inc}}\right|, \tag{7.8}$$

where λ is a cross section related multiplier and defined as:

$$\lambda = \begin{cases} \sigma_{\mathrm{t}}, & \sigma_{\mathrm{t}} > 0 \\ 1.0, & \mathrm{otherwise} \end{cases} \tag{7.9}$$

A boundary weak form as the following can be achieved through a similar minimization process shown in Section 7.2.1:

$$\int\limits_{\vec{n}\cdot\vec{\Omega}<0} d\Omega \int\limits_{\partial\mathcal{D}} ds\ \lambda \left|\vec{n}\cdot\vec{\Omega}\right| \frac{v\psi}{\left|\psi - \psi^{\mathrm{inc}}\right|} = \int\limits_{\vec{n}\cdot\vec{\Omega}<0} d\Omega \int\limits_{\partial\mathcal{D}} ds\ \lambda \left|\vec{n}\cdot\vec{\Omega}\right| \frac{v\psi^{\mathrm{inc}}}{\left|\psi - \psi^{\mathrm{inc}}\right|} \tag{7.10}$$

7.2.3 L_1 and relaxed L_1 weak forms

Whence we have the complete L_1 finite element weak formulations:

$$\begin{aligned}
&\int_{4\pi} d\Omega \int_{\mathcal{D}} d\vec{r}\, \frac{\mathcal{L}v\mathcal{L}\psi}{|R|} + \int_{\vec{n}\cdot\vec{\Omega}<0} d\Omega \int_{\partial\mathcal{D}} ds\, \lambda \left|\vec{n}\cdot\vec{\Omega}\right| \frac{v\psi}{|\psi-\psi^{\text{inc}}|} \\
&= \int_{4\pi} d\Omega \int_{\mathcal{D}} d\vec{r}\, \frac{\mathcal{L}v\left(\mathcal{S}\psi + \frac{Q}{4\pi}\right)}{|R|} + \int_{\vec{n}\cdot\vec{\Omega}<0} d\Omega \int_{\partial\mathcal{D}} ds\, \lambda \left|\vec{n}\cdot\vec{\Omega}\right| \frac{v\psi^{\text{inc}}}{|\psi-\psi^{\text{inc}}|}
\end{aligned} \tag{7.11}$$

Due to the assumption of letting ζ vanish, the weak form above is not an approximated but exact L_1 finite element formulation. However, solving such an weak form can be extremely challenging especially when residual in the problem varies by several orders. Instead, we propose a relaxed L_1 formulation. Such a formulation is composed such that in regions with moderate to large residuals, L_1 is executed, or least-squares method is used otherwise. As a result, we attain the weak form with a relaxation factor θ:

$$\begin{aligned}
&\int_{4\pi} d\Omega \int_{\mathcal{D}} d\vec{r}\, \frac{\theta\mathcal{L}v\mathcal{L}\psi}{\max(\theta,|R|)} + \int_{\vec{n}\cdot\vec{\Omega}<0} d\Omega \int_{\partial\mathcal{D}} ds\, \lambda \left|\vec{n}\cdot\vec{\Omega}\right| \frac{\theta v\psi}{\max(\theta,|\psi-\psi^{\text{inc}}|)} \\
&= \int_{4\pi} d\Omega \int_{\mathcal{D}} d\vec{r}\, \frac{\theta\mathcal{L}v\left(\mathcal{S}\psi + \frac{Q}{4\pi}\right)}{\max(\theta,|R|)} + \int_{\vec{n}\cdot\vec{\Omega}<0} d\Omega \int_{\partial\mathcal{D}} ds\, \lambda \left|\vec{n}\cdot\vec{\Omega}\right| \frac{\theta v\psi^{\text{inc}}}{\max(\theta,|\psi-\psi^{\text{inc}}|)}
\end{aligned} \tag{7.12}$$

It is quite flexible to choose a θ. The effects of varying it will be illustrated in Section 7.4.1. Normally, we choose to use θ to be $0.01 \sim 0.1|R|_{\max}$ (Herein, $|R|_{\max}$ denotes the maximum absolute residual of all directions.). Smaller θ can be used, yet, the efficiency of linear solves would be degraded without gaining much more accuracy.

When implementing, the residuals are evaluated on each spatial quadrature points for every single direction. This is one of the drawbacks of this method that it requires storing or performing on-the-fly calculations of the pointwise residuals. Three-point and five-point

Gauss quadrature have been applied. Both presents quite similar solutions.

7.3 Scheme and Other Details

Unfortunately, the RL_1 is nonlinear so an appropriate nonlinear scheme is necessary in order to solve Eq. (7.12). Such a scheme is equivalent to pointwisely weighting the least-squares formulation with $\theta/\max(\theta, |R|)$. Hitherto, similar reweighting schemes have only been developed to solve equations in fluid dynamics community[28, 30]. When solving neutronics problems, the scattering phenomena adds more complexity into the problem.

In fact, the motivation of incorporating scattering terms into the source is such that scattering is treatable with source iteration as regular least-squares. Based on the assumption that least-squares can approximate the solution roughly well[28], the nonlinear scheme writes as:

1. Calculate pointwise residuals for Nonlinear Iteration (NI) l from NI $l-1$;
2. Update the weak form Eq. (7.12);
3. Solve Eq. (7.12) with source iteration;
4. Given a nonlinear tolerance tol, check nonlinear convergence $e = \frac{\|\phi^l - \phi^{l-1}\|}{\|\phi^l\|}$:
   (a) If $e < tol$, stop.
   (b) else, go to Step 1.

In the source-iteration step, DSA is utilized.

The motivation behind developing a RL_1 boundary was from the observation that oscillations happen on boundary when using LS boundary condition with RL_1 in interior for incident-boundary problems, especially for the cases that incident boundary condition is only applied partially on a boundary.

Further, Lowrie[62] point out the IRLS developed by Jiang[28] is not a minimizer of L_1 residual functional. The consequence is such that in advection problems with discontinuous incident boundary, the method provides perfect accuracy while the solution is erroneous when the boundary is smooth and continuous. We found the reason is to be IRLS utilized a cell-wise weighting. In situations where projection of real solution could vary much in a single cell, the weightings for different spots in a cell, however, are supposed to be distinct. In this work, we use pointwise weighting on quadrature points, which fixes the issue existed in IRLS.

7.4 Numerics

All tests in this section was carried out with C++ Open source library deal.II[52]. Four test problem will be performed. The first one is a single direction transport in void (void problem). The second one is mono-directional (the most grazing direction in S_4 quadrature) transport an absorber with partially applied but smooth boundary condition (smooth boundary problem). Further, two classic tests for void treatment will be presented (Ackroyd and dog-leg problems[64, 56]). Last but not least, two convergence tests will be included.

7.4.1 Void problem

Radiation transport in void is a challenge with a wide ranges of methods[27, 61, 64]. Even with conventional linear discontinuous method, numerical artifacts can still manifest[27]. In void, the Boltzmann equation essentially describes a linear advection process that particles only stream in individual directions. Therefore, with S_N angular discretization, particles never “talk" in different directions. It forms a discontinuity in cross-wind direction as a result. Schemes such as LS which is continuous in space, might raise artifacts without being able to well handle the discontinuity. Figure 7.2a shows a example of LS for solving void transport (0.5×0.5 cm square). The unit incident boundary condition

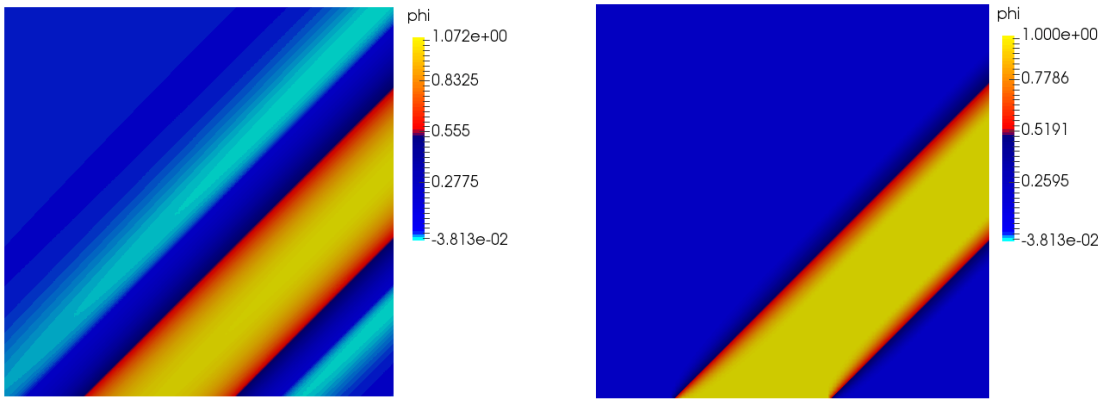

(a) LS result in void.

(b) RL_1 result in void.

Figure 7.2: LS and RL_1 method comparison in void transport problem.

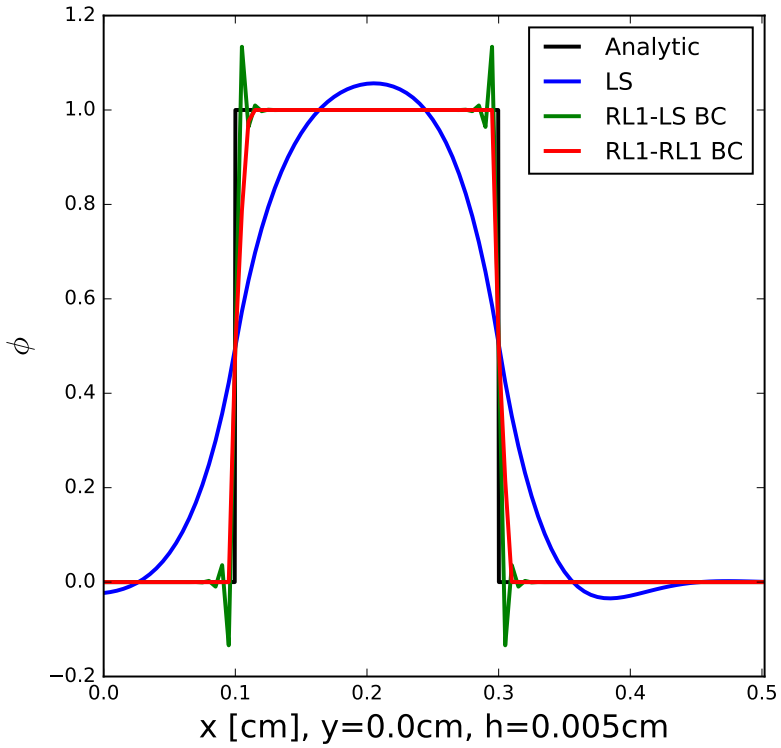

Figure 7.3: LS and RL_1 boundary condition comparison.

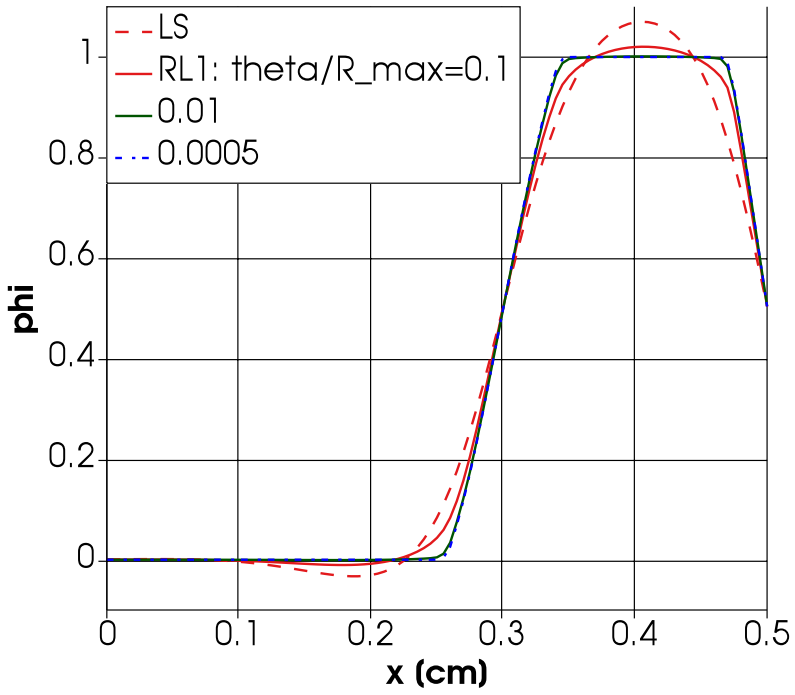

Figure 7.4: Line-outs ($y = 0.2$ cm) for different $\theta/|R|_{\max}$.

is applied only on part of the boundary. LS presents oscillatory results along the radiation (see the cyan part). Also, LS has overshoot that by 7% for the maximum flux. As a comparison, Figure 7.2b gives a non-negative flux profile with unit flux for as the maximum in interior.

The other emphasis is on the boundary condition. Figure 7.3 gives a comparison between RL_1 boundary condition and LS boundary condition used with RL_1 interior weak form. LS boundary presents oscillatory and negative solutions while allowing discontinuity solution. On the other hand, RL_1, by smearing a little, gives accurate representation of the analytic boundary flux.

The void test above is performed with $\theta/|R|_{\max} = 0.01$. In fact, it is quite robust in terms of varying θ. As the line-outs ($y = 0.2$ cm) shown in Figure 7.4, by using a large θ

(the one with $\theta/|R|_{\max} = 0.1$), RL_1 is able to effectively damp the oscillations around the discontinuous solution. Further reducing θ such that $\theta/|R|_{\max} \leq 0.01$ present graphically consistent results. Therefore, for the rest of the tests in this section, we choose to set $\theta/|R|_{\max} = 0.05$.

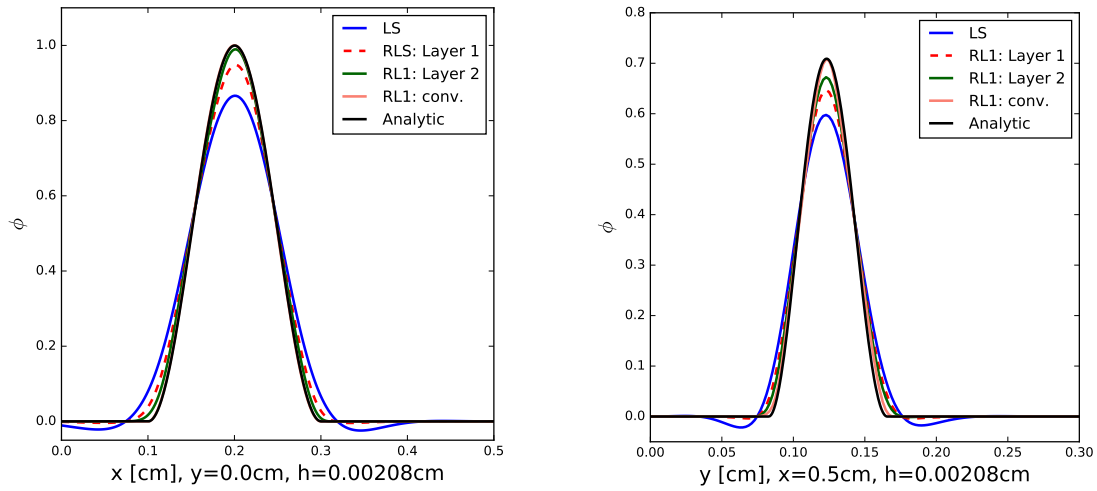

(a) Results on bottom boundary.

(b) Results on right boundary.

Figure 7.5: Boundary results comparison for smooth boundary problem.

7.4.2 Smooth boundary problem

Unlike the void problem with discontinuous boundary condition, we use a sine-like boundary condition which is C^1 continuous in this test with the same geometry. An absorber is used instead ($\sigma_\text{t} = 1$ cm^{-1}). The direction is the most grazing direction in a S_4 quadrature set. We compare the behavior of different schemes on the bottom boundary and right boundary in Figure 7.5.

With converged RL_1 (red line), one would see no difference graphically except the little smearing in Figure 7.5b. Moreover, without convergence but with only one or two

layers of reweighting, RL_1 can still deliver acceptable results (orange dash line and green line).

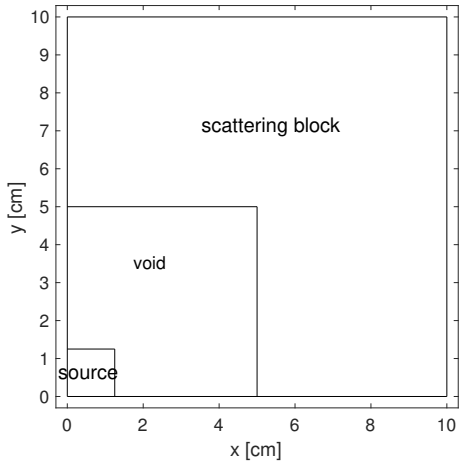

Figure 7.6: Ackroyd problem configuration.

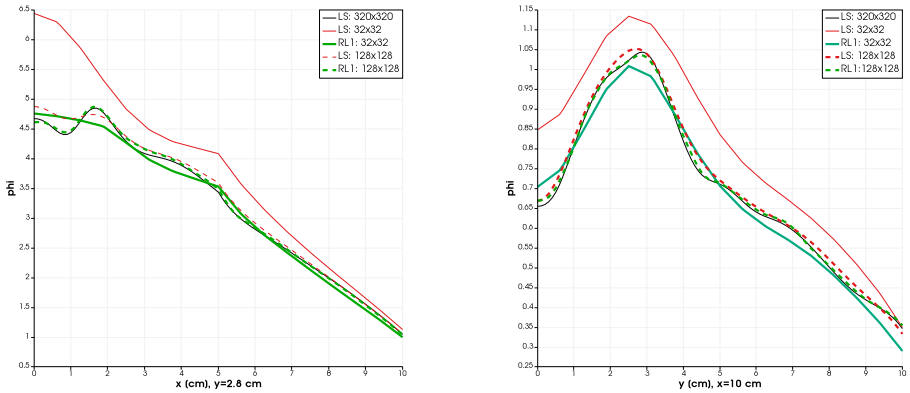

(a) Results across the void. (b) Results on boundary.

Figure 7.7: Ackroyd problem line-out plots.

7.4.3 Ackroyd test

The Ackroyd problem[64, 65] is a heterogeneous problem with the central block and outer shield to be with high scattering ratio ($\sigma_{\mathrm{t}} = 0.2, \sigma_{\mathrm{s}} = 0.19$). The gap between two blocks is a void (see Figure 7.6 for a quarter of the problem geometry). The whole problem is symmetric about x-axis and y-axis. We examine a line-out in going through the void (Figure 7.7a) and another one on the boundary (Figure 7.7b). In both cases RL_1 (green lines and green dash lines) follows well with the fine mesh LS results (black lines), while LS presents solution with noticeably larger error in the graph norm.

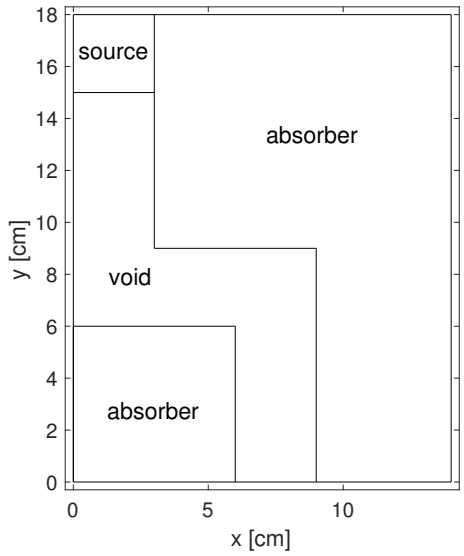

(a) A quarter configuration.

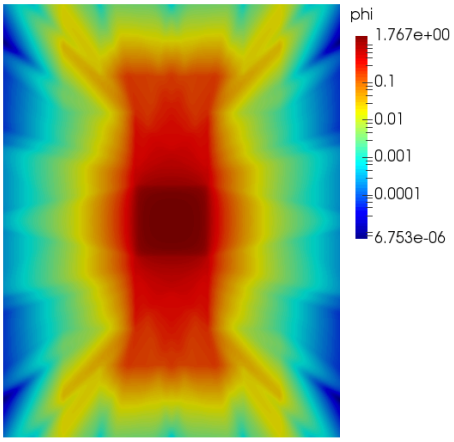

(b) LSS_8 solution with 840x1080 cells.

Figure 7.8: Configuration and LSS_8 solution with 840x1080 cells for dog-leg problem.

7.4.4 Dog-leg test

Last but not least, we present a crooked pipe (dog-leg shaped) test. Since the geometry is symmetric about x-axis and $y = 18$ cm, only a quarter of geometry is shown in Figure

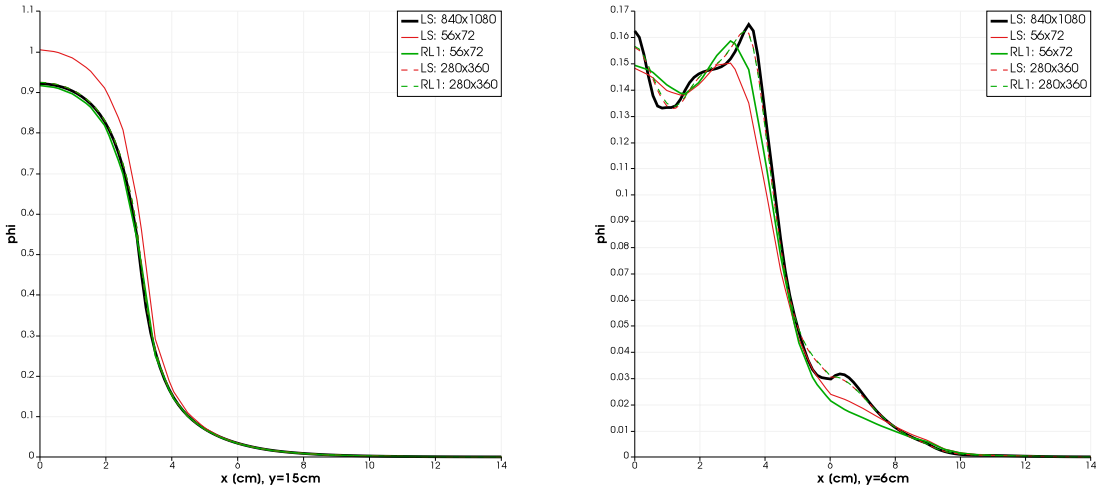

(a) Results along $y = 15$ cm.

(b) Results along $y = 6$ cm.

Figure 7.9: Dog-leg problem line-out plots.

7.8a. Figure 7.8b presents the reference solution with 840×1080 cells. In the source and absorber $\sigma_a = \sigma_t = 0.5$. A unit volumetric source is used in the calculation.

Figure 7.9a draws a line-out along $y = 15$, across the source surface. It is noticed that with coarse mesh (56×72 cells), RL_1 (green line) follows the reference well while LS (red line) is away from the reference solution. Meanwhile, when refining (280×360 cells), both methods agree with the reference.

Figure 7.9b presents the comparison along $y = 6$ cm, going across the bottom absorber surface. We observe some improvements from using RL_1 method for both coarse mesh and fine mesh. Yet the effects is not as significant as what is produced around the source region. The bottom line is it does not degrade the solution.

7.4.5 Convergence tests

We first test the L_1 error of the angular flux in void problem. As illustrated in Figure 7.10, both LS and RL_1 hold half order convergence. In addition, non-converged RL_1 also

improve the solution from LS[1].

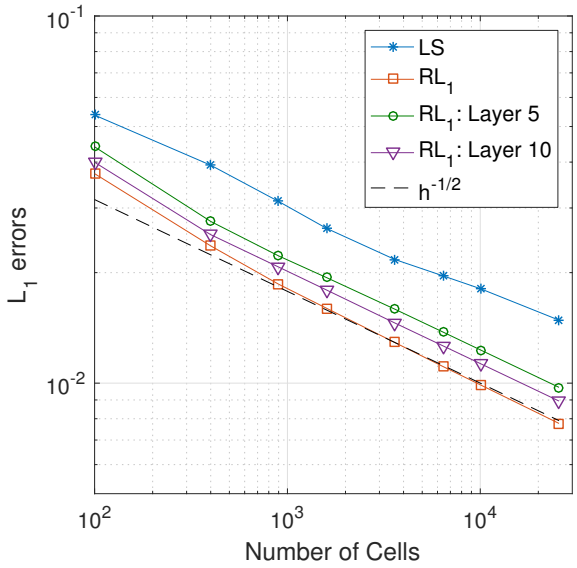

Figure 7.10: Void problem convergence test.

The other test is an S_2 uniformly incident problem on the whole bottom boundary with an absorption $\sigma_t = 1.0$ cm^{-1}. We examine the L_1 error of scalar fluxes. The angular flux in one direction are drawn in Figures 7.11a and 7.11b. In the homogeneous absorber problem LS is oscillatory while RL_1 is oscillation free. Examining the convergence tests in Figure 7.12 we found both LS and RL_1 have poor convergence rates in such a case. Asymptotically, LS has a convergence of quarter-th order. RL_1 has a similar behavior but with lower error magnitudes.

[1] h stands for mesh size.

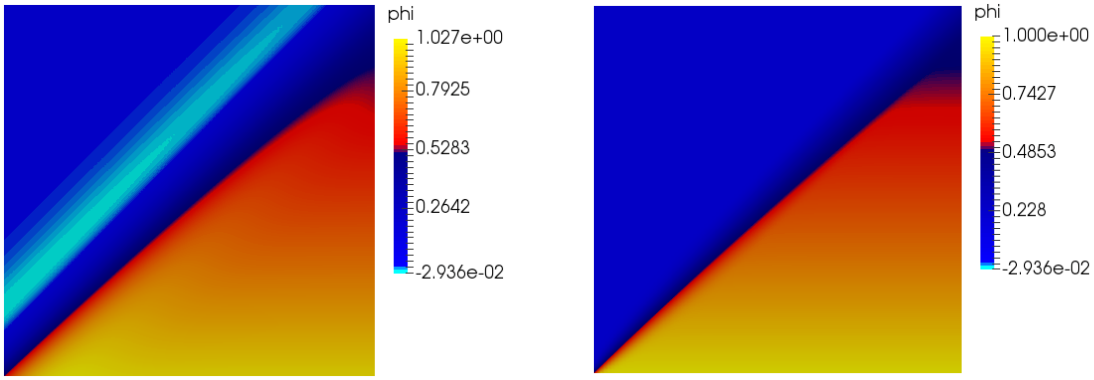

(a) LS. (b) RL_1.

Figure 7.11: Angular flux distributions in incident convergence test.

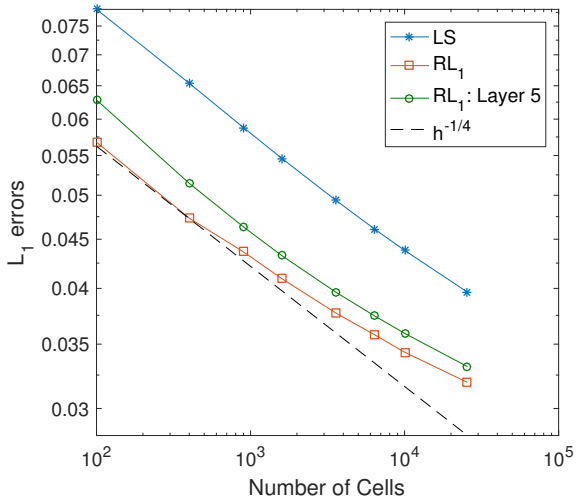

Figure 7.12: Incident absorber scalar flux errors.

8. GLOBALLY CONSERVATIVE CONTIGUOUS DISCONTINUOUS LEAST-SQUARES FINITE ELEMENT METHOD

8.1 Introduction

Section 6 derives least-squares finite element method for solving transport equation. It is valuable when solving with S_N angular discretization and source iteration that system for each direction is symmetric positive definite. An additional benefit is that continuous basis functions can be used for discretization.

However, when used in problems, such as k-eigenvalue problems, where global conservation is important, a conservative treatment must be applied[58]. Another downside of using least-squares method, which is also true for other second order forms of transport equations, is that particle causality is not preserved correctly.

8.2 A Contiguous-Discontinuous Least-Squares Discretization

8.2.1 The contiguous discontinuous least-squares (CDLS) functional and weak formulation

The LS formulation symmetrizes the streaming operator so CFEM can be applied in the discretization. However, it does not have global conservation in heterogeneous problems where cross sections are not space-independent over the whole domain, which is crucial in k-eigenvalue problems. Also, with the presence of thin-thick material interface, the accuracy of scalar flux degrades.

The intuition is to solve using least-squares in subdomains where cross sections are constant, i.e. without the presence of material interface, and transferring angular flux on interfaces in a sweep way. In such a case, solution will be continuous within subdomains and discontinuous on interfaces. In fact, we can derive the desired method in the same

procedure deriving LS method described in Section 6. To start, we define a functional in the following form:

$$\Gamma_{\mathrm{CDLS}} = \frac{1}{2}\sum_{\mathcal{D}_\mathrm{i}}\int_{4\pi} d\Omega \int_{\mathcal{D}_\mathrm{i}} dV\ (\mathcal{L}_\mathrm{i}\psi_\mathrm{i} - q_\mathrm{si})^2 + \frac{1}{2}\int_{\vec{n}\cdot\vec{\Omega}<0} d\Omega \int_{\partial\mathcal{D}} dV\ \sigma_\mathrm{t}\left|\vec{n}\cdot\vec{\Omega}\right|(\psi - \psi^{\mathrm{inc}})^2$$
$$+ \frac{1}{2}\sum_{\mathcal{D}_\mathrm{i}}\sum_{\mathcal{F}_\mathrm{ij}}\int_{\vec{n}_\mathrm{i}\cdot\vec{\Omega}<0} d\Omega \int_{\mathcal{F}_\mathrm{ij}} ds\ \sigma_\mathrm{ti}\left|\vec{n}_\mathrm{i}\cdot\vec{\Omega}\right|(\psi_i^{\mathrm{inc}} - \psi_j^{\mathrm{inc}})^2, \tag{8.1}$$

where $\mathcal{F}_\mathrm{ij}$ is the interface between $\mathcal{D}_\mathrm{i}$ and any contiguous subdomain $\mathcal{D}_\mathrm{j}$. Accordingly, the variational problem turns to: find ψ_i in a polynomial space $\mathcal{V}$ such that $\forall v_\mathrm{i} \in \mathcal{V}$,

$$\sum_{\mathcal{D}_\mathrm{i}}\left(\int_{4\pi} d\Omega \int_{\mathcal{D}_\mathrm{i}} dV\ \mathcal{L}_\mathrm{i}v_\mathrm{i}\left(\mathcal{L}_\mathrm{i} - \mathcal{S}_\mathrm{i}\right)\psi_\mathrm{i} + \sum_{\mathcal{F}_\mathrm{ij}}\sigma_\mathrm{ti}\int_{\vec{n}_\mathrm{i}\cdot\vec{\Omega}<0} d\Omega \int_{\mathcal{F}_\mathrm{ij}} ds\ \left|\vec{n}_\mathrm{i}\cdot\vec{\Omega}\right| v_\mathrm{i}\left(\psi_\mathrm{i} - \psi_\mathrm{j}\right)\right)$$
$$+ \int_{\vec{n}\cdot\vec{\Omega}<0} d\Omega \int_{\partial\mathcal{D}} ds\ \sigma_\mathrm{t}\left|\vec{n}\cdot\vec{\Omega}\right| v\psi \tag{8.2}$$
$$= \sum_{\mathcal{D}_\mathrm{i}}\int_{4\pi} d\Omega \int_{\mathcal{D}_\mathrm{i}} dV\,\mathcal{L}_\mathrm{i}v_\mathrm{i}\frac{Q_\mathrm{i}}{4\pi} + \int_{\vec{n}\cdot\vec{\Omega}<0} d\Omega \int_{\partial\mathcal{D}} ds\ \sigma_\mathrm{t}\left|\vec{n}\cdot\vec{\Omega}\right| v\psi^{\mathrm{inc}}$$

Compared with ordinary LS method, CDLS does not enforce the continuity on subdomain interface. That gives the possibility of combining least-squares method and transport sweeps. One could solve the transport equation by using LS in each subdomain individually and perform the sweeps on the interface. This is an advantage over ordinary transport sweeps. For unstructured mesh, it is easier to perform LS calculations than to use transport sweeps in the sense of implementation. The 1D implementation is done in this hybrid way.

8.2.2 Subdomain-wise and global conservations

LS does not possess global conservation in heterogeneous problems. However, we can demonstrate that CDLS is conservative not only globally, but also on each subdomain individually.

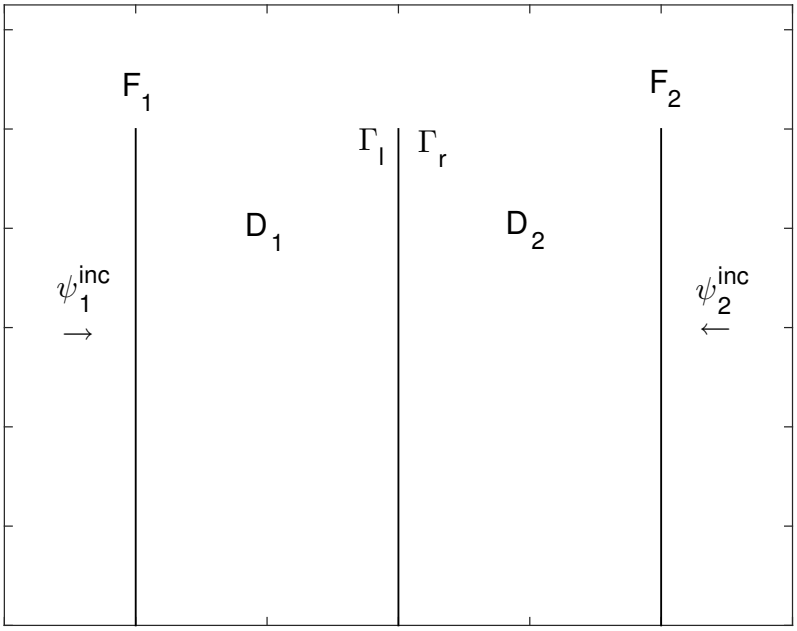

Figure 8.1: Generic multi-region problem for illustration of global conservation for CDLS.

Taking all the test functions to be unity, i.e. $v_{\rm i} = 1$, a conservative scheme with appropriate boundary conditions is expected to retain zero balance[1], i.e.,

$$\int\limits_{\vec{n}\cdot\vec{\Omega}>0} d\Omega \int\limits_{\partial\mathcal{D}} ds\ |\vec{n}\cdot\vec{\Omega}|\psi - \int\limits_{\vec{n}\cdot\vec{\Omega}<0} d\Omega \int\limits_{\partial\mathcal{D}} ds\ |\vec{n}\cdot\vec{\Omega}|\psi^{\rm inc} + \int\limits_{\mathcal{D}} dV\ (\sigma_{\rm a}\phi - Q) = 0, \quad (8.3)$$

where $Q = \int\limits_{4\pi} d\Omega\ q$.

Take $v_{\rm i} = 1$ to Eq. (8.2), we see

$$\mathcal{L}_{\rm i} v_{\rm i} = \vec{\Omega}\cdot\nabla v_{\rm i} + \sigma_{\rm ti} v_{\rm i} = \sigma_{\rm ti} \quad (8.4)$$

To simplify the notation, we consider a infinite slab with only two subdomains (see

[1] In fact, one would instead expect a round-off balance, which is related to the machine precision.

Figure 8.1), within each the cross sections are constants. Consequently, Eq. (8.2) is turned to be

$$\int\limits_{4\pi} d\Omega \int\limits_{\mathcal{D}_1} dV\ \sigma_{\mathrm{t}1} \left(\left(\mathcal{L}_1 - \mathcal{S}_1\right) \psi_1 - \frac{Q_1}{4\pi} \right) + \int\limits_{\vec{n}_1 \cdot \vec{\Omega} < 0} d\Omega \int\limits_{\mathcal{F}_1} ds\ \sigma_{\mathrm{t}1} \left| \vec{n}_1 \cdot \vec{\Omega} \right| \left(\psi_1 - \psi_1^{\mathrm{inc}} \right) \tag{8.5}$$

$$+ \int\limits_{4\pi} d\Omega \int\limits_{\mathcal{D}_2} dV\ \sigma_{\mathrm{t}2} \left(\left(\mathcal{L}_2 - \mathcal{S}_2\right) \psi_2 - \frac{Q_2}{4\pi} \right) + \int\limits_{\vec{n}_2 \cdot \vec{\Omega} < 0} d\Omega \int\limits_{\mathcal{F}_2} ds\ \sigma_{\mathrm{t}2} \left| \vec{n}_2 \cdot \vec{\Omega} \right| \left(\psi_2 - \psi_2^{\mathrm{inc}} \right)$$

$$+ \int\limits_{\vec{n}_1 \cdot \vec{\Omega} < 0} d\Omega \int\limits_{\Gamma_{\mathrm{l}}} ds\ \sigma_{\mathrm{t}1} \left| \vec{n}_1 \cdot \vec{\Omega} \right| \left(\psi_1 - \psi_2 \right) + \int\limits_{\vec{n}_2 \cdot \vec{\Omega} < 0} d\Omega \int\limits_{\Gamma_{\mathrm{r}}} ds\ \sigma_{\mathrm{t}2} \left| \vec{n}_2 \cdot \vec{\Omega} \right| \left(\psi_2 - \psi_1 \right) = 0$$

Define

$$j_{\mathrm{i}}^{\mathrm{in}}(\vec{r}) := \int\limits_{\vec{n}_{\mathrm{i}} \cdot \vec{\Omega} < 0} d\Omega\ \left| \vec{n}_{\mathrm{i}} \cdot \vec{\Omega} \right| \psi_{\mathrm{i}} \quad \text{and} \quad j_{\mathrm{i}}^{\mathrm{out}}(\vec{r}) := \int\limits_{\vec{n}_{\mathrm{i}} \cdot \vec{\Omega} > 0} d\Omega\ \left| \vec{n}_{\mathrm{i}} \cdot \vec{\Omega} \right| \psi_{\mathrm{i}}, \tag{8.6}$$

then

$$\int\limits_{4\pi} d\Omega \int\limits_{\mathcal{D}_{\mathrm{i}}} dV\ \left(\mathcal{L}_{\mathrm{i}} \psi_{\mathrm{i}} - \mathcal{S}_{\mathrm{i}} \psi_{\mathrm{i}} - \frac{Q_{\mathrm{i}}}{4\pi} \right) = \int\limits_{\partial \mathcal{D}_{\mathrm{i}}} ds\ \left(j_{\mathrm{i}}^{\mathrm{out}} - j_{\mathrm{i}}^{\mathrm{in}} \right) + \int\limits_{\mathcal{D}_{\mathrm{i}}} dV\ \left(\sigma_{\mathrm{ai}} \phi_{\mathrm{i}} - Q_{\mathrm{i}} \right) \tag{8.7}$$

Plug Eq. (8.7) back into (8.5) and rearrange, leading to:

$$
\begin{aligned}
&\sigma_{\mathrm{t}1}\left(\int_{\mathcal{F}_1}+\int_{\Gamma_{\mathrm{l}}}\right) ds\ (j_1^{\mathrm{out}}-\cancel{j_1^{\mathrm{in}}})+\sigma_{\mathrm{t}1}\int_{\mathcal{D}_1} dV\ (\sigma_{\mathrm{a}1}\phi_1-Q_1)\\
&+\sigma_{\mathrm{t}2}\left(\int_{\mathcal{F}_2}+\int_{\Gamma_{\mathrm{r}}}\right) ds\ (j_2^{\mathrm{out}}-\cancel{j_2^{\mathrm{in}}})+\sigma_{\mathrm{t}2}\int_{\mathcal{D}_2} dV\ (\sigma_{\mathrm{a}1}\phi_2-Q_2)\\
&+\sigma_{\mathrm{t}1}\left(\int_{\mathcal{D}_1}+\int_{\Gamma_{\mathrm{l}}}\right) ds\ \cancel{j_1^{\mathrm{in}}}-\sigma_{\mathrm{t}1}\int_{\mathcal{F}_1} ds\int_{\vec{n}_1\cdot\vec{\Omega}<0} d\Omega\ \left|\vec{n}_1\cdot\vec{\Omega}\right|\psi_1^{\mathrm{inc}}\\
&-\sigma_{\mathrm{t}1}\int_{\Gamma_{\mathrm{l}}} ds\int_{\vec{n}_1\cdot\vec{\Omega}<0} d\Omega\ \left|\vec{n}_1\cdot\vec{\Omega}\right|\psi_2(\Gamma_{\mathrm{r}})+\sigma_{\mathrm{t}2}\left(\int_{\mathcal{D}_2}+\int_{\Gamma_{\mathrm{r}}}\right) ds\ \cancel{j_2^{\mathrm{in}}}\\
&-\sigma_{\mathrm{t}2}\int_{\mathcal{F}_2} ds\int_{\vec{n}_2\cdot\vec{\Omega}<0} d\Omega\ \left|\vec{n}_2\cdot\vec{\Omega}\right|\psi_2^{\mathrm{inc}}-\sigma_{\mathrm{t}2}\int_{\Gamma_{\mathrm{r}}} ds\int_{\vec{n}_2\cdot\vec{\Omega}<0} d\Omega\ \left|\vec{n}_2\cdot\vec{\Omega}\right|\psi_1(\Gamma_{\mathrm{l}})=0
\end{aligned}
\tag{8.8}
$$

Denote balances of $\mathcal{D}_1$ and $\mathcal{D}_2$ by $\mathbf{B}_1$ and $\mathbf{B}_2$ we then have a weighted balance equation:

$$
\sigma_{\mathrm{t}1}\mathbf{B}_1+\sigma_{\mathrm{t}2}\mathbf{B}_2=0, \tag{8.9}
$$

where

$$
\begin{aligned}
\mathbf{B}_1=&\left(\int_{\mathcal{F}_1}+\int_{\Gamma_{\mathrm{l}}}\right) ds\ j_1^{\mathrm{out}}+\int_{\mathcal{D}_1} dV\ (\sigma_{\mathrm{a}1}\phi_1-Q_1)\\
&-\int_{\mathcal{F}_1} ds\int_{\vec{n}_1\cdot\vec{\Omega}<0} d\Omega\ \left|\vec{n}_1\cdot\vec{\Omega}\right|\psi_1^{\mathrm{inc}}-\int_{\Gamma_{\mathrm{l}}} ds\int_{\vec{n}_1\cdot\vec{\Omega}<0} d\Omega\ \left|\vec{n}_1\cdot\vec{\Omega}\right|\psi_2(\Gamma_{\mathrm{r}}),
\end{aligned}
\tag{8.10}
$$

and

$$\mathbf{B}_2 = \left(\int\limits_{\mathcal{F}_2} + \int\limits_{\Gamma_\mathrm{r}} \right) ds\, j_2^{\mathrm{out}} + \int\limits_{\mathcal{D}_2} dV\, (\sigma_{\mathrm{a}2}\phi_2 - Q_2) \tag{8.11}$$
$$- \int\limits_{\mathcal{F}_2} ds \int\limits_{\vec{n}_2\cdot\vec{\Omega}<0} d\Omega\, \left|\vec{n}_2\cdot\vec{\Omega}\right| \psi_2^{\mathrm{inc}} - \int\limits_{\Gamma_\mathrm{r}} ds \int\limits_{\vec{n}_2\cdot\vec{\Omega}<0} d\Omega\, \left|\vec{n}_2\cdot\vec{\Omega}\right| \psi_1(\Gamma_\mathrm{l}).$$

Apparently, for all nonzero $\sigma_{\mathrm{t}1}$ and $\sigma_{\mathrm{t}2}$, in order to make Eq. (8.9) true, one must have:

$$\mathbf{B}_1 \equiv 0 \quad \text{and} \quad \mathbf{B}_2 \equiv 0, \tag{8.12}$$

which claims the conservations within each subdomain.

In addition, since $\mathbf{B}_1$ and $\mathbf{B}_2$ are zero, therefore

$$\mathbf{B}_1 + \mathbf{B}_2 \equiv 0 \tag{8.13}$$

Note that

$$\int\limits_{\Gamma_\mathrm{l}} ds\, j_1^{\mathrm{out}} - \int\limits_{\Gamma_\mathrm{r}} ds \int\limits_{\vec{n}\cdot\vec{\Omega}<0} d\Omega\, |\vec{n}\cdot\vec{\Omega}| \psi_1(\Gamma_\mathrm{l}) \tag{8.14}$$
$$= \int\limits_{\Gamma_\mathrm{l}} ds\, j_1^{\mathrm{out}} - \int\limits_{\Gamma_\mathrm{l}} ds \int\limits_{\vec{n}\cdot\vec{\Omega}>0} d\Omega\, |\vec{n}\cdot\vec{\Omega}| \psi_1(\Gamma_\mathrm{l}) = 0,$$

and

$$\int\limits_{\Gamma_\mathrm{r}} ds\, j_2^{\mathrm{out}} - \int\limits_{\Gamma_\mathrm{l}} ds \int\limits_{\vec{n}\cdot\vec{\Omega}<0} d\Omega\, |\vec{n}\cdot\vec{\Omega}| \psi_2(\Gamma_\mathrm{r}) \tag{8.15}$$
$$= \int\limits_{\Gamma_\mathrm{r}} ds\, j_2^{\mathrm{out}} - \int\limits_{\Gamma_\mathrm{r}} ds \int\limits_{\vec{n}\cdot\vec{\Omega}>0} d\Omega\, |\vec{n}\cdot\vec{\Omega}| \psi_2(\Gamma_\mathrm{r}) = 0.$$

As a consequence,

$$\mathbf{B}_1 + \mathbf{B}_2 = \int_{\mathcal{F}_1} ds\; j_1^{\text{out}} + \int_{\mathcal{D}_1} dV\; (\sigma_{\text{a}1}\phi_1 - Q_1) - \int_{\mathcal{F}_1} ds \int_{\vec{n}\cdot\vec{\Omega}<0} d\Omega\; |\vec{n}\cdot\vec{\Omega}|\psi_1^{\text{inc}} \qquad (8.16)$$
$$+ \int_{\mathcal{F}_2} ds\; j_2^{\text{out}} + \int_{\mathcal{D}_2} dV\; (\sigma_{\text{a}2}\phi_2 - Q_2) - \int_{\mathcal{F}_2} ds \int_{\vec{n}\cdot\vec{\Omega}<0} d\Omega\; |\vec{n}\cdot\vec{\Omega}|\psi_2^{\text{inc}} = 0$$

Hence, the CDLS scheme is subdomain-wise and globally conservative if the cross section is subdomain-wise constant (and nonzero).

8.3 Numerical Results

The implementation is carried out by the C++ Open source finite element library deal.II[52]. In all tests, we also include results from solving the globally conservative self-adjoint angular flux (SAAF) equation with CFEM as a comparison[25, 66].

8.3.1 Modified Reed's problem

A modified Reed's problem is used[54]. The material properties are listed in Table 8.1. By using S_8 in angle, the result comparison is presented by Figure 8.2. 48 cells are used for CFEM-LS, CFEM-SAAF and CDLS calculations. Specifically, the interfaces are set at $x = 3, 5, 6$ cm which are where the material interfaces reside.

The reference is made from CFEM-SAAF with 8000 cells. Without enough refinements, solutions for CFEM-SAAF and CFEM-LS are distorted in the thin absorber ($x \in (3, 5)$ cm). Also, the accuracy in the source region $x \in (2, 3)$ cm. However, CDLS, through adding a few extra DoFs on the material interfaces and therefore introducing discontinuities, CDLS fits the 8000 cells reference with merely 48 cells graphically well.

To better fit the thick regions, methods with CFEM tends to "sacrifice" the thin-region solution. On the other hand, CDLS scheme chooses to break the continuity on the inter-

faces and add one extra DoF at one interface per direction. The gain is thin regions, away from the interfaces, scalar flux is recovered and thus accurate.

Table 8.1: Material configuration for modified Reed's problem.

x [cm]	(0,2)	(2,3)	(3,5)	(5,6)	(6,8)
σ_{t} [cm^{-1}]	1	1	0.005	5	50
σ_{s} [cm^{-1}]	0.9	0.9	0	0	0
Q	0	1	0	0	50

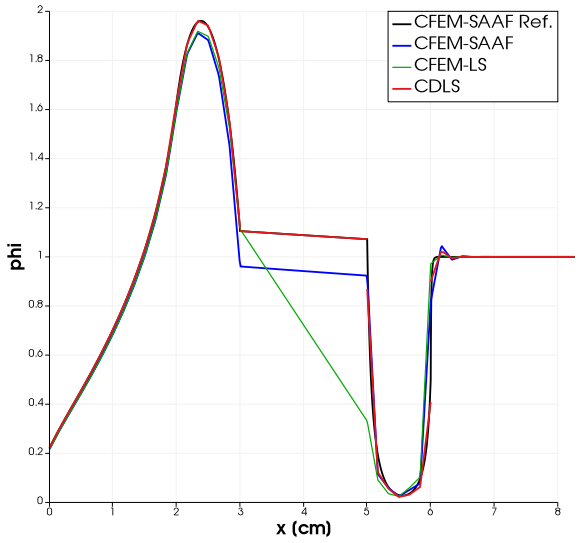

Figure 8.2: Modified Reed's problem result comparison.

8.3.2 Two-region absorption problem

The second test problem is a 1D slab pure absorber problem. There is a unit incident angular flux on left boundary of the slab. No source appears in the domain. $\sigma_{\mathrm{t}} = 0.1$ cm^{-1}

for $x < 1$ cm or $\sigma_{\mathrm{t}} = 10$ cm^{-1} otherwise.

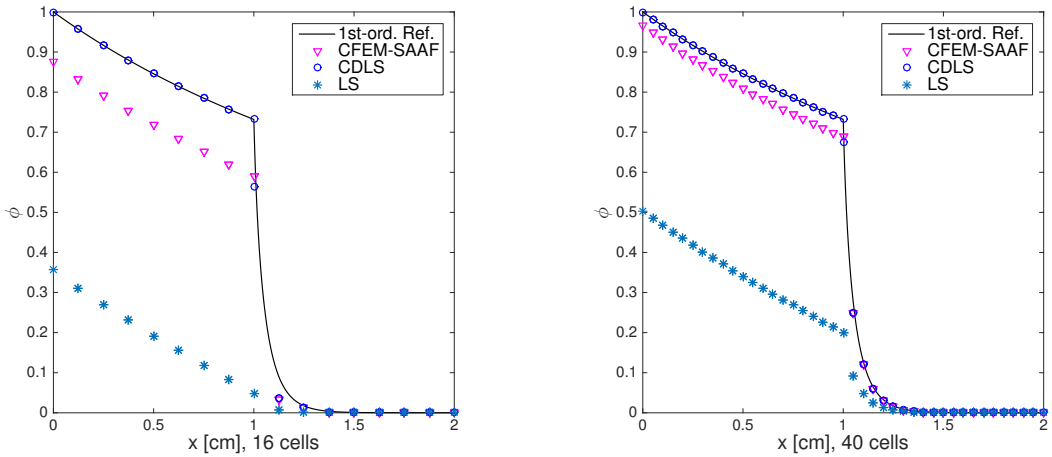

(a) 16 cells. (b) 40 cells.

Figure 8.3: Two-region absorption results comparison with LS, SAAF and CDLS.

As illustrated in Figure 8.3, due to the existence of the thin-thick material interface, the LS solution in thin material is heavily affected by trying to fit the thick-region solution, using more cells is not effectively improving the LS solution. SAAF, on the other hand, present better solution with the same DoF counts. One reason would be due to the presence of the $1/\sigma_{\mathrm{t}}$ weight to the streaming operator, the effects from the thick material is weakened. But both schemes does not have correct particle causality. Nevertheless, breaking the continuity results in accurate solution in thin material even with merely 16 cells in total (see Figure 8.3a). Increasing the total number of cells improves the solution in the thick material as well (see Figure 8.3b). When calculating the leakage error as shown in Figure 8.4, one observes that CDLS has a second order convergence rate, yet, with noticeably lower error magnitudes.

Moreover, the absolute values of global balances are examined (see Table 8.2). As expected, LS presents large balances. Refining the mesh does lower the balance, the ef-

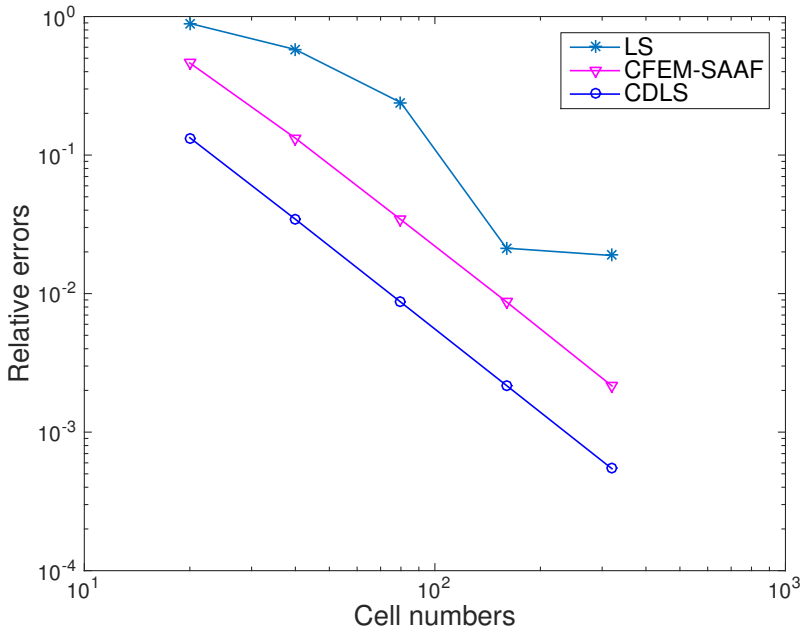

Figure 8.4: Leakage errors at right boundary.

fectiveness is doubtable. On the other hand, CFEM-SAAF gives round-off balance as expected. The results for CDLS demonstrate the global conservation as claimed in previous sections.

Table 8.2: Absolute global balance with different methods.

Cell numbers	20	40	80	160	320
LS	4.232×10^{-1}	3.213×10^{-1}	1.782×10^{-1}	1.715×10^{-1}	2.474×10^{-2}
CFEM-SAAF	2.958×10^{-14}	8.958×10^{-14}	1.311×10^{-13}	6.392×10^{-13}	2.808×10^{-12}
CDLS	1.074×10^{-13}	3.834×10^{-13}	7.462×10^{-13}	1.045×10^{-11}	1.352×10^{-12}

8.3.3 One group iron-water problem

The last test is modified from a iron-water shielding problem[67] used to test accuracy of numerical schemes in relatively thick materials (see the configuration in Figure 8.5a).

S_2 is used in angular discretization. The quantity of interest is the absorption rate in iron shield. The reference is with CFEM-SAAF using 1200x1200 cells. As shown in Figure 8.5, LS and SAAF presents similar spatial convergence rates. However, LS presents lower accuracy than CFEM-SAAF with the presence of material interface between iron and water. On the other hand, by setting two interfaces between iron and water and introducing extra DoFs on the interfaces, CDLS presents roughly the same spatial convergence but much lower error magnitudes than CFEM-SAAF and ordinary LS.

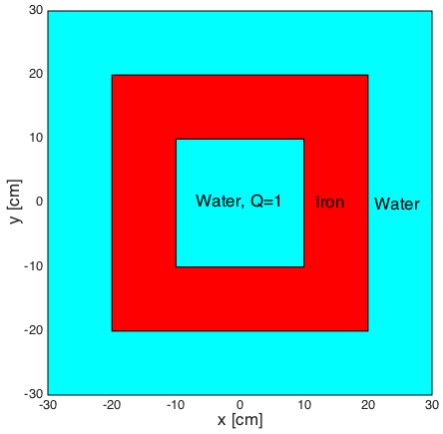

(a) Problem configuration.

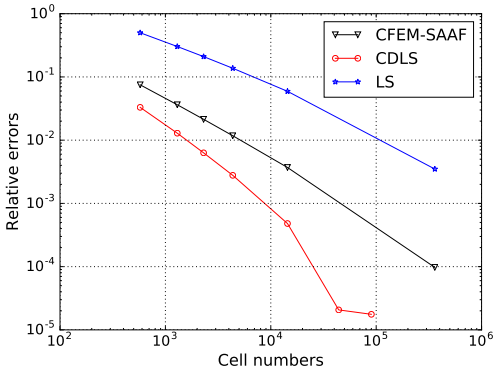

(b) Relative errors of absorption rate in iron.

Figure 8.5: Iron water problem.

8.4 Summary

In this section, we proposed a contiguous-discontinuous least-squares discretization method for solving neutron particle transport. Such a method resembles least-squares discretization in each subdomain of the problem. Yet, additional interface term appears to alleviate the solution and retain the subdomain-wise and global conservation by introducing discontinuity on the material interfaces.

Since CD methodology allows the discontinuity on the subdomain interface, different angular schemes, e.g. S_N and P_N can be used in different subdomains. In fact, with borrowing the CD concept, such an angular hybridation scheme has been implemented in MOOSE based application Rattlesnake as its multiscale capability[68, 69], which will be introduced in Section 9.

9. CONTIGUOUS DISCONTINUOUS DISCRETIZATION OF SELF-ADJOINT ANGULAR FLUX EQUATION AND ANGULAR HYBRIDATION SCHEMES

9.1 Introduction

Section 8 introduced a novel least-squares finite element method solving neutron transport method. Such a method, unlike ordinary least-squares method, is globally conservative if total cross section in each contiguous subdomain is constant, which is significant for k-eigenvalue problems for neutronics. Also, it is observed that there is a noticeable increase in accuracy with allowing the discontinuity of angular flux on the interface between contiguous subdomains by paying the price of a few extra interface DoFs.

Nevertheless, the obtainment of conservation is restricted by having constant cross section in each single subdomain. Issues would arise from this restriction. In high fidelity calculations without homogenizing the materials, numerous interfaces are needed setting up even for assembly calculations, which is exhausting and complex.

The enhancement in accuracy, however, signifies having discontinuity existing on contiguous subdomain interfaces. Section 6 illustrates having reciprocal total cross section weighted least-squares formulation illustrates CFEM-SAAF, which is globally conservative in heterogeneous problems. Thusly, an intuition is to introduce contiguous discontinuity when discretizing the transport equation with weighted least-squares finite element. Therein, the resemblance of CFEM-SAAF in each subdomain can be realized. What would be expected is that even non-constant cross sections are used in each subdomain, conservation in each subdomain can still be preserved such that global conservation is obtained. Due to the nature of the method, we name it contiguous-discontinuous (CD)-SAAF.

In this section, we will derive the proposed method. Moreover, we will demonstrate CD-SAAF method resembles CFEM-SAAF in subdomains with upwinding on subdomain

interfaces. Last but not least, we develop an angular hybridation scheme allowing the coupling between S_N and P_N on different sides of an interface utilizing CD-SAAF methodology.

9.2 Theory: Angularly Continuous Weak Forms

9.2.1 Contiguous-discontinuous (CD) weighted least-squares functional

Formulations

Let us start off defining the functional as follows:

$$\begin{aligned}\Gamma_{\mathrm{CD-SAAF}} = &\frac{1}{2}\sum_{\mathcal{D}_\mathrm{i}\subset\mathcal{D}}\int_{4\pi} d\Omega \int_{\mathcal{D}_\mathrm{i}} d\vec{r}\,\frac{1}{\sigma_{\mathrm{ti}}}(\mathcal{L}_\mathrm{i} - \underline{\left(\mathcal{S}_\mathrm{i}\psi_\mathrm{i} + \frac{Q_\mathrm{i}}{4\pi}\right)})^2 \\ &+\frac{1}{2}\sum_{\mathcal{D}_\mathrm{i}\subset\mathcal{D}}\sum_{\mathcal{F}_\mathrm{ij}}\int_{\vec{n}_\mathrm{i}\cdot\vec{\Omega}<0} d\Omega \int_{\mathcal{F}_\mathrm{ij}} ds\ \left|\vec{n}_\mathrm{i}\cdot\vec{\Omega}\right|(\psi_\mathrm{i}-\psi_\mathrm{j})^2 \\ &+\frac{1}{2}\int_{\vec{n}\cdot\vec{\Omega}<0} d\Omega \int_{\partial\mathcal{D}} ds\ \left|\vec{n}\cdot\vec{\Omega}\right|(\psi-\psi^{\mathrm{inc}})^2,\end{aligned} \tag{9.1}$$

where $\mathcal{F}_\mathrm{ij}$ is the interface between $\mathcal{D}_\mathrm{i}$ and contiguous subdomain $\mathcal{D}_\mathrm{j}$ and $\vec{n}_\mathrm{i}$ is the outward normal of subdomain $\mathcal{D}_\mathrm{i}$ on the interface. Again, the scattering source in the underlined part is rather treated as part of volumetric source as the WLS functional in Section 6. It then leads to the following contiguous-discontinuous weak formulation formulation: find $\psi \in \mathcal{V}_\mathrm{i} \subset \mathcal{V},\ \mathrm{i}=1,\cdots$ such that $\forall v_\mathrm{i} \in \mathcal{V}_\mathrm{i} \subset \mathcal{V},\ \mathrm{i}=1,\cdots$

$$\begin{aligned}&\sum_{\mathcal{D}_\mathrm{i}\subset\mathcal{D}}\int_{\mathcal{D}_\mathrm{i}} d\vec{r}\,\left(\vec{\Omega}\cdot\nabla v_\mathrm{i}\frac{1}{\sigma_\mathrm{t}}\vec{\Omega}\cdot\nabla\psi_\mathrm{i} + \sigma_\mathrm{t}v_\mathrm{i}\psi_\mathrm{i} - v_\mathrm{i}\left(\mathcal{S}_\mathrm{i}\psi_\mathrm{i}+\frac{Q_\mathrm{i}}{4\pi}\right) - \vec{\Omega}\cdot\nabla v_\mathrm{i}\frac{\mathcal{S}_\mathrm{i}\psi_\mathrm{i}+\frac{Q_\mathrm{i}}{4\pi}}{\sigma_\mathrm{t}}\right) \\ &+\sum_{\mathcal{D}_\mathrm{i}\subset\mathcal{D}}\sum_{\mathcal{F}_\mathrm{ij}}\int_{\mathcal{F}_\mathrm{ij}} ds\,\left(\int_{\vec{n}_\mathrm{i}\cdot\vec{\Omega}>0} d\Omega\ \left|\vec{n}_\mathrm{i}\cdot\vec{\Omega}\right| v_\mathrm{i}\psi_\mathrm{i} - \int_{\vec{n}_\mathrm{i}\cdot\vec{\Omega}<0} d\Omega\ \left|\vec{n}_\mathrm{i}\cdot\vec{\Omega}\right| v_\mathrm{i}\psi_\mathrm{j}\right) \\ &+\int_{\vec{n}\cdot\vec{\Omega}>0} d\Omega\int_{\partial\mathcal{D}} ds\ \left|\vec{n}\cdot\vec{\Omega}\right| v\psi - \int_{\vec{n}\cdot\vec{\Omega}<0} d\Omega\int_{\partial\mathcal{D}} ds\ \left|\vec{n}\cdot\vec{\Omega}\right| v\psi^{\mathrm{inc}} = 0.\end{aligned} \tag{9.2}$$

Intuitively, the formulation above resembles CFEM-SAAF within the subdomains and on domain boundaries but differ from it on interfaces. By the formulation above, when assembling the system, every subdomain interface needs visiting twice. We then name the resulting scheme CD-SAAF in the rest of the report.

Upwinding flux on the interface

It can be demonstrated that the mechanism allowing interface discontinuity is essentially the upwinding. To reveal that, we would visit every face only once but visit both sides simultaneously when assembling. The new assembly strategy is identical to the original interface formulation except the logics differs.

We isolate the interface terms and denote them as I. Let $\mathcal{F}$ stand for the interface of two contiguous subdomains generically represented by $\mathcal{D}_1$ and $\mathcal{D}_2$. Let $\vec{n}_1$ and $\vec{n}_2$ are outward normal vectors of $\mathcal{D}_1$ and $\mathcal{D}_2$, respectively, then the interface term can be rewritten as:

$$\begin{aligned} I = &\int_\Gamma ds \int_{\vec{n}_1\cdot\vec{\Omega}>0} d\Omega \left|\vec{n}_1\cdot\vec{\Omega}\right| v_1\psi_1 - \int_\Gamma ds \int_{\vec{n}_1\cdot\vec{\Omega}<0} d\Omega \left|\vec{n}_1\cdot\vec{\Omega}\right| v_1\psi_2 \\ &+ \int_\Gamma ds \int_{\vec{n}_2\cdot\vec{\Omega}>0} d\Omega \left|\vec{n}_2\cdot\vec{\Omega}\right| v_2\psi_2 - \int_\Gamma ds \int_{\vec{n}_2\cdot\vec{\Omega}<0} d\Omega \left|\vec{n}_2\cdot\vec{\Omega}\right| v_2\psi_1. \end{aligned} \tag{9.3}$$

By recognizing $\vec{n}_1 = -\vec{n}_2$, Eq. (9.3) can be shortened as:

$$\begin{aligned} I = &\int_\Gamma ds \int_{\vec{n}_1\cdot\vec{\Omega}>0} d\Omega \left|\vec{n}_1\cdot\vec{\Omega}\right| (v_1 - v_2)\,\psi_1 \\ &+ \int_\Gamma ds \int_{\vec{n}_1\cdot\vec{\Omega}<0} d\Omega \left|\vec{n}_1\cdot\vec{\Omega}\right| (v_2 - v_1)\,\psi_2 \end{aligned} \tag{9.4}$$

Thereafter, it is clear the equation above is identical to the classic upwinding formula-

tion:

$$I = \int_{\Gamma} ds \int_{4\pi} d\Omega \left| \vec{n} \cdot \vec{\Omega} \right| [v] \, \psi_{+} \tag{9.5a}$$

$$[v] := v_{+} - v_{-}, \tag{9.5b}$$

where $\psi_{\pm}$ are the upwind and downwind angular flux with respect to direction $\vec{\Omega}$.

9.2.2 Compact weak forms of CFEM-SAAF and CD-SAAF

To simplify the notations, we define the inner products with generic functions a and b:

$$(a, b)_{\mathcal{D}_{\mathrm{i}}} = \int_{4\pi} d\Omega \int_{\mathcal{D}_{\mathrm{i}}} d\vec{r} \, a^{\top} b \tag{9.6a}$$

$$< a, b >_{\mathcal{E}} = \int_{\mathcal{F}} ds \, a^{\top} b, \tag{9.6b}$$

$$< a, b >_{\mathcal{E}}^{+} = \int_{\vec{n}\cdot\vec{\Omega}>0} d\Omega \int_{\mathcal{F}} ds \, |\vec{n} \cdot \vec{\Omega}| a^{\top} b, \tag{9.6c}$$

$$< a, b >_{\mathcal{E}}^{-} = \int_{\vec{n}\cdot\vec{\Omega}<0} d\Omega \int_{\mathcal{F}} ds \, |\vec{n} \cdot \vec{\Omega}| a^{\top} b, \tag{9.6d}$$

where $\mathcal{E}$ generically represents the interior or boundary face and $\vec{n}$ is the outward normal vector of the element.

The weak formulation of CD-SAAF is then re-expressed as:

$$\begin{aligned}
&\sum_{\mathcal{D}_\mathrm{i}\subset\mathcal{D}}\Bigg[\left(\vec{\Omega}\cdot\nabla v_\mathrm{i},\frac{1}{\sigma_\mathrm{ti}}\vec{\Omega}\cdot\nabla\psi_\mathrm{i}\right)_{\mathcal{D}_\mathrm{i}}+\left(v_\mathrm{i},\sigma_\mathrm{ti}\psi_\mathrm{i}\right)_{\mathcal{D}_\mathrm{i}}\\
&-\left(v_\mathrm{i},\left(\mathcal{S}_\mathrm{i}\psi_\mathrm{i}+\frac{Q_\mathrm{i}}{4\pi}\right)\right)_{\mathcal{D}_\mathrm{i}}-\left(\vec{\Omega}\cdot\nabla v_\mathrm{i},\frac{\left(\mathcal{S}_\mathrm{i}\psi_\mathrm{i}+\frac{Q_\mathrm{i}}{4\pi}\right)}{\sigma_\mathrm{ti}}\right)_{\mathcal{D}_\mathrm{i}}\Bigg]\\
&+\sum_{\mathcal{F}}\int_{4\pi}d\vec{\Omega}\ \left|\vec{n}\cdot\vec{\Omega}\right|\left\langle\left[v\right],\psi_+\right\rangle_{\mathcal{F}}+\left\langle v,\psi\right\rangle^{+}_{\partial\mathcal{D}}-\left\langle v,\psi^{\mathrm{inc}}\right\rangle^{-}_{\partial\mathcal{D}}=0,
\end{aligned}\tag{9.7}$$

where $\mathcal{F}$ is the interface between any two contiguous subdomains.

More specifically, the weak form can be separated as bilinear form $b_{\mathrm{CD-SAAF}}(v,\psi)$ and linear form $l_{\mathrm{CD-SAAF}}(v)$ such that $b(v,\psi)=l(v)$:

$$\begin{aligned}
b_{\mathrm{CD-SAAF}}(v,\psi)=&\sum_{\mathcal{D}_\mathrm{i}\subset\mathcal{D}}\Bigg[\left(\vec{\Omega}\cdot\nabla v_\mathrm{i},\frac{1}{\sigma_\mathrm{ti}}\vec{\Omega}\cdot\nabla\psi_\mathrm{i}\right)_{\mathcal{D}_\mathrm{i}}+\left(v_\mathrm{i},\sigma_\mathrm{ti}\psi_\mathrm{i}\right)_{\mathcal{D}_\mathrm{i}}-\left(v_\mathrm{i},\mathcal{S}_\mathrm{i}\psi_\mathrm{i}\right)_{\mathcal{D}_\mathrm{i}}\\
&-\left(\vec{\Omega}\cdot\nabla v_\mathrm{i},\frac{\mathcal{S}_\mathrm{i}\psi_\mathrm{i}}{\sigma_\mathrm{ti}}\right)_{\mathcal{D}_\mathrm{i}}\Bigg]+\sum_{\mathcal{F}}\int_{4\pi}d\vec{\Omega}\ \left|\vec{n}\cdot\vec{\Omega}\right|\left\langle\left[v\right],\psi_+\right\rangle_{\mathcal{F}}+\left\langle v,\psi\right\rangle^{+}_{\partial\mathcal{D}}
\end{aligned}\tag{9.8a}$$

$$l_{\mathrm{CD-SAAF}}(v)=\sum_{\mathcal{D}_\mathrm{i}\subset\mathcal{D}}\left[\left(v_\mathrm{i},\frac{Q_\mathrm{i}}{4\pi}\right)_{\mathcal{D}_\mathrm{i}}+\left(\vec{\Omega}\cdot\nabla v_\mathrm{i},\frac{Q_\mathrm{i}}{4\pi\sigma_\mathrm{ti}}\right)_{\mathcal{D}_\mathrm{i}}\right]+\left\langle v,\psi\right\rangle^{-}_{\partial\mathcal{D}}\tag{9.8b}$$

As a comparison, compact CFEM-SAAF weak form, identical to Eq. (6.8), is:

$$\begin{aligned}
b_{\mathrm{CFEM-SAAF}}(v,\psi)=&\left(\vec{\Omega}\cdot\nabla v,\frac{1}{\sigma_\mathrm{t}}\vec{\Omega}\cdot\nabla\psi\right)_{\mathcal{D}}+\left(v,\sigma_\mathrm{t}\psi\right)_{\mathcal{D}}-\left(v,\mathbf{S}\psi\right)_{\mathcal{D}}\\
&-\left(\vec{\Omega}\cdot\nabla v,\frac{\mathbf{S}\psi}{\sigma_\mathrm{t}}\right)_{\mathcal{D}}+\left\langle v,\psi\right\rangle^{+}_{\partial\mathcal{D}}
\end{aligned}\tag{9.9a}$$

$$l_{\mathrm{CFEM-SAAF}}(v)=\left(v,\frac{Q}{4\pi}\right)_{\mathcal{D}}+\left(\vec{\Omega}\cdot\nabla v,\frac{Q}{4\pi\sigma_\mathrm{t}}\right)_{\mathcal{D}}+\left\langle v,\psi^{\mathrm{inc}}\right\rangle^{-}_{\partial\mathcal{D}}\tag{9.9b}$$

Apparently, they are almost identical except that CD-SAAF possesses an extra interface upwinding term.

9.3 Angular Discretizations

9.3.1 Redefine the upwinding

Classic upwinding definition is with respect to specific direction, which brings difficulty when treating P_N interface conditions. Therefore, we redefine the upwinding. In the redefinition, we always specify a master and a slave subdomains. For instance, we always set S_N and P_N subdomains to be master and slave, respectively, when we have an S_N-P_N interface. We fix the normal vector to be pointing from master subdomain to slave subdomain. Further, we have some new definitions accordingly:

$$\psi^{\mp} = \lim_{s\to 0^+} \psi(\vec{r} \mp s\vec{n}) \quad \text{and} \quad [\![v]\!] = v^- - v^+, \tag{9.10}$$

that being said, ψ_- is always fixed to be the master angular flux. Consequently, the upwinding in Eq. (9.5a) can be redefined as:

$$\begin{aligned} I &= \int_{\mathcal{F}} ds \left(\int_{\vec{n}\cdot\vec{\Omega}>0} d\Omega \left|\vec{n}\cdot\vec{\Omega}\right| [\![v]\!]\, \psi^- - \int_{\vec{n}\cdot\vec{\Omega}<0} d\Omega \left|\vec{n}\cdot\vec{\Omega}\right| [\![v]\!]\, \psi^+ \right) \\ &= \left\langle [\![v]\!], \psi^- \right\rangle_{\mathcal{F}}^{+} - \left\langle [\![v]\!], \psi^+ \right\rangle_{\mathcal{F}}^{-} \end{aligned} \tag{9.11}$$

9.3.2 S_N-S_N coupling

Discretization with S_N in both subdomains is straightforward with the surface inner product:

$$I = \sum_{\vec{n}\cdot\vec{\Omega}_{\mathrm{m}}>0} w_{\mathrm{m}} \left|\vec{n}\cdot\vec{\Omega}_{\mathrm{m}}\right| \left\langle [\![v_{\mathrm{m}}]\!], \psi_{\mathrm{m}}^- \right\rangle_{\mathcal{F}} - \sum_{\vec{n}\cdot\vec{\Omega}_{\mathrm{m}}<0} w_{\mathrm{m}} \left|\vec{n}\cdot\vec{\Omega}_{\mathrm{m}}\right| \left\langle [\![v_{\mathrm{m}}]\!], \psi_{\mathrm{m}}^+ \right\rangle_{\mathcal{F}} \tag{9.12}$$

9.3.3 P_N-P_N couplings

There would be a necessity by setting up an interface between two P_N schemes[1].

Direct coupling

Define the P_N expansion of angular flux with the real-valued spherical harmonics:

$$\psi(\vec{\Omega}) = \vec{R}^{\top}(\vec{\Omega})\overrightarrow{\Phi}, \tag{9.13}$$

where $\vec{R}^{\top}(\vec{\Omega})$ and $\overrightarrow{\Phi}$ are column vectors of spherical harmonics and moments, respectively. In addition to the $\mathbf{L}^{+}$ defined previously, let us further define the $\mathbf{L}^{-}$ matrix:

$$\mathbf{L}^{-} = \int\limits_{\vec{n}\cdot\vec{\Omega}<0} d\Omega \left|\vec{n}\cdot\vec{\Omega}\right| \vec{R}(\vec{\Omega})\vec{R}^{\top}(\vec{\Omega}) \tag{9.14}$$

Plug Eqs. (B.8c) and (9.14) into Eq. (9.11), we shall see

$$\begin{aligned} I &= \left\langle \vec{v}^{-}, \mathbf{L}^{+}\overrightarrow{\Phi}^{-} \right\rangle_{\mathcal{F}} + \left\langle \vec{v}^{+}, \mathbf{L}^{-}\overrightarrow{\Phi}^{+} \right\rangle_{\mathcal{F}} - \left\langle \vec{v}^{+}, \mathbf{L}^{-}\overrightarrow{\Phi}^{-} \right\rangle_{\mathcal{F}} - \left\langle \vec{v}^{-}, \mathbf{L}^{+}\overrightarrow{\Phi}^{+} \right\rangle_{\mathcal{F}} \\ &= \left\langle [\![\vec{v}]\!], \left(\mathbf{L}^{+} - \mathbf{L}^{-}\right)\left\{\overrightarrow{\Phi}\right\} + \frac{\mathbf{L}^{+} + \mathbf{L}^{-}}{2}[\![\overrightarrow{\Phi}]\!] \right\rangle_{\mathcal{F}} \end{aligned} \tag{9.15}$$

where $\left\{\overrightarrow{\Phi}\right\} = \left(\overrightarrow{\Phi}^{+} + \overrightarrow{\Phi}^{-}\right)/2$.

Riemann solver based coupling

It is clear that the formulation above is similar to the upwinding in P_N-DFEM. The difference is P_N-DFEM upwinding is based on the eigenstructure of streaming matrices while Eq. (9.15) is not. An alternative is then to perform eigenvalue decomposition and reformulate the upwinding in an eigenstructure based way. The cause of the difference is that the original formulation for upwinding is for transport equation before discretized in

[1]For formulation about SAAF-P_N scheme, see Appendix B

angle while the eigenstructure based method is the upwinding after P_N angular discretization has been introduced.

That being said, the interface weak form should be rewritten as:

$$I = \int\limits_{\vec{n}\cdot\vec{\Omega}>0} d\Omega \ \left|\vec{n}\cdot\vec{\Omega}\right| \left\langle [\![v]\!], \widetilde{\psi} \right\rangle_{\mathcal{F}} - \int\limits_{\vec{n}\cdot\vec{\Omega}<0} d\Omega \ \left|\vec{n}\cdot\vec{\Omega}\right| \left\langle [\![v]\!], \widetilde{\psi} \right\rangle_{\mathcal{F}}, \tag{9.16}$$

where $\widetilde{\psi}$ is the "proper" angular flux that needs to be specified. Expand all the angular flux with P_N method, we have:

$$I(\vec{v}^{-}, \vec{v}^{+}, \widetilde{\Phi}) = \left\langle \vec{v}^{-}, \left(\mathbf{L}^{+} - \mathbf{L}^{-}\right) \widetilde{\Phi} \right\rangle_{\mathcal{F}} - \left\langle \vec{v}^{+}, \left(\mathbf{L}^{+} - \mathbf{L}^{-}\right) \widetilde{\Phi} \right\rangle_{\mathcal{F}}. \tag{9.17}$$

To know how to perform upwinding for $\mathbf{L}^{+} - \mathbf{L}^{-}$, we need to know the eigenstructure of it. Since $\mathbf{L}^{+} - \mathbf{L}^{-}$ is symmetric, eigenvalue decomposition brings

$$\left(\mathbf{L}^{+} - \mathbf{L}^{-}\right) = \mathbf{U}\Lambda\mathbf{U}^{\top}, \tag{9.18}$$

where Λ is the diagonal matrix whose diagonal elements are the eigenvalues of $\mathbf{L}^{+} - \mathbf{L}^{-}$. $\mathbf{U}$ is a matrix whose columns are the eigenvectors of $\mathbf{L}^{+} - \mathbf{L}^{-}$. Before proceeding, we separate Λ to be Λ^{+}, which contains only the positive eigenvalues of Λ, and Λ^{-}, which contains the absolute values of negative eigenvalues. Accordingly, we have:

$$\Lambda = \Lambda^{+} - \Lambda^{-}. \tag{9.19}$$

With the separation, the interface weak form can be transformed to

$$I = \left\langle \vec{v}^{-}, \mathbf{U}\Lambda^{+}\mathbf{U}^{\top}\overrightarrow{\Phi}^{-} \right\rangle_{\mathcal{F}} - \left\langle \vec{v}^{-}, \mathbf{U}\left|\Lambda^{-}\right|\mathbf{U}^{\top}\overrightarrow{\Phi}^{+} \right\rangle_{\mathcal{F}} - \left\langle \vec{v}^{+}, \mathbf{U}\Lambda^{+}\mathbf{U}^{\top}\overrightarrow{\Phi}^{-} \right\rangle_{\mathcal{F}} + \left\langle \vec{v}^{+}, \mathbf{U}\left|\Lambda^{-}\right|\mathbf{U}^{\top}\overrightarrow{\Phi}^{+} \right\rangle_{\mathcal{F}}. \tag{9.20}$$

Similarly, the weak form can be re-expressed in a upwinding way:

$$I = \left\langle \left[\!\left[\vec{v}\right]\!\right], \left(\mathbf{M}^{+} - \mathbf{M}^{-}\right)\left\{\overrightarrow{\Phi}\right\} + \frac{\mathbf{M}^{+} + \mathbf{M}^{-}}{2}\left[\!\left[\overrightarrow{\Phi}\right]\!\right] \right\rangle_{\mathcal{F}} \tag{9.21}$$

Note

$$\mathbf{M}^{+} - \mathbf{M}^{-} = \mathbf{U}\Lambda^{+}\mathbf{U}^{\top} - \mathbf{U}\Lambda^{-}\mathbf{U}^{\top} = \mathbf{U}(\Lambda^{+} - \Lambda^{-})\mathbf{U}^{\top} = \mathbf{U}\Lambda\mathbf{U}^{\top} = \mathbf{L}^{+} - \mathbf{L}^{-}, \tag{9.22}$$

therefore

$$I = \left\langle \left[\!\left[\vec{v}\right]\!\right], \left(\mathbf{L}^{+} - \mathbf{L}^{-}\right)\left\{\overrightarrow{\Phi}\right\} + \frac{\mathbf{M}^{+} + \mathbf{M}^{-}}{2}\left[\!\left[\overrightarrow{\Phi}\right]\!\right] \right\rangle_{\mathcal{F}}. \tag{9.23}$$

At the end, the upwinding differs from the original upwinding in the dissipation part. If we further proceed, we know:

$$\mathbf{M}^{+} + \mathbf{M}^{-} = \mathbf{U}\Lambda^{+}\mathbf{U}^{\top} + \mathbf{U}\Lambda^{-}\mathbf{U}^{\top} = \mathbf{U}(\Lambda^{+} + \Lambda^{-})\mathbf{U}^{\top} = \sum_{\mathrm{k}} \vec{r}_{\mathrm{k}} \left|\lambda_{\mathrm{k}}\right| \vec{r}_{\mathrm{k}}^{\top}, \tag{9.24}$$

where $(\lambda_{\mathrm{k}}, \vec{r}_{\mathrm{k}})$ is the k^{th} eigenpair of $\mathbf{L}^{+} - \mathbf{L}^{-}$. Introduce this back to (9.23), we will have the upwinding represented by Roe type Riemann solver:

$$I = \left\langle \left[\!\left[\vec{v}\right]\!\right], \left(\mathbf{L}^{+} - \mathbf{L}^{-}\right)\left\{\overrightarrow{\Phi}\right\} + \frac{\sum_{\mathrm{k}} \vec{r}_{\mathrm{k}} \left|\lambda_{\mathrm{k}}\right| \vec{r}_{\mathrm{k}}^{\top}}{2}\left[\!\left[\overrightarrow{\Phi}\right]\!\right] \right\rangle_{\mathcal{F}} \tag{9.25}$$

Differentiations and consistency

The original type of upwinding for P_N-P_N coupling is performed before doing angular integration while the eigenstructure based upwinding is performed after projecting transport equation into spherical harmonics function space. Intuitively, the solutions from these two method are expected to be different. In fact, for the original type of upwinding, one performs half-range integral in angle for each side of an interface, which naturally resembles a Marshak boundary condition on the boundary[16]. Meanwhile, the Riemann type of upwinding resembles the “ghost cell" boundary condition[7, 6] on the interface. Fundamentally, such a boundary condition is a Mark type boundary condition as it transmits the boundary information outside current subdomain in characterized directions and speed, based on the eigenstructure of streaming matrix, into the subdomains. However, the consistency appears when increasing the P_N angular order as the angular error from truncating spherical harmonics vanishes.

9.3.4 S_N-P_N coupling

S_N-P_N interface is chosen to be formulated in a similar way to S_N-S_N. Factually, it is much easier to reconstruct angular flux in discrete directions in S_N quadrature using P_N moments than the reverse way to keep the compatibility of DoFs from different subdomains.

We always choose S_N to be the master subdomain such that the normal vector $\vec{n}$ is always fixed to be from S_N to P_N. We separate the weak form into four different terms based on what the weight and basis functions are, i.e.

$$I = I_{\mathrm{S}_N-\mathrm{S}_N} + I_{\mathrm{S}_N-\mathrm{P}_N} + I_{\mathrm{P}_N-\mathrm{S}_N} + I_{\mathrm{P}_N-\mathrm{P}_N}. \tag{9.26}$$

By performing all the angular integration with the quadrature identical to the S_N sub-

domain, we can specifically write all four terms as:

$$I_{\mathrm{S}_N-\mathrm{S}_N} = \sum_{\vec{\Omega}_m\cdot\vec{n}_m>0} w_{\mathrm{m}} \left\langle \left| \vec{n}\cdot\vec{\Omega}_{\mathrm{m}} \right| v_m^-, \psi_m^- \right\rangle_{\mathcal{F}}, \tag{9.27}$$

$$\begin{aligned} I_{\mathrm{S}_N-\mathrm{P}_N} &= -\sum_{\vec{\Omega}_m\cdot\vec{n}_m<0} w_{\mathrm{m}} \left\langle \left| \vec{n}\cdot\vec{\Omega}_{\mathrm{m}} \right| v_m^-, \psi_m^+ \right\rangle_{\mathcal{F}} \\ &= -\sum_{\vec{\Omega}_m\cdot\vec{n}_m<0} w_{\mathrm{m}} \left\langle \left| \vec{n}\cdot\vec{\Omega}_{\mathrm{m}} \right| v_m^-, \vec{R}^{\top}(\vec{\Omega}_m)\overrightarrow{\Phi}^+ \right\rangle_{\mathcal{F}}, \end{aligned} \tag{9.28}$$

$$\begin{aligned} I_{\mathrm{P}_N-\mathrm{S}_N} &= -\sum_{\vec{\Omega}_m\cdot\vec{n}_m>0} w_{\mathrm{m}} \left\langle \left| \vec{n}\cdot\vec{\Omega}_{\mathrm{m}} \right| v_m^+, \psi_m^- \right\rangle_{\mathcal{F}} \\ &= -\sum_{\vec{\Omega}_m\cdot\vec{n}_m>0} w_{\mathrm{m}} \left\langle \left| \vec{n}\cdot\vec{\Omega}_{\mathrm{m}} \right| \vec{R}^{\top}(\vec{\Omega}_m)\vec{v}^+, \psi_m^- \right\rangle_{\mathcal{F}}, \end{aligned} \tag{9.29}$$

$$\begin{aligned} I_{\mathrm{P}_N-\mathrm{P}_N} &= \sum_{\vec{\Omega}_m\cdot\vec{n}_m<0} w_{\mathrm{m}} \left\langle \left| \vec{n}\cdot\vec{\Omega}_{\mathrm{m}} \right| v_m^-, \psi_m^- \right\rangle_{\mathcal{F}} \\ &= \sum_{\vec{\Omega}_m\cdot\vec{n}_m<0} w_{\mathrm{m}} \left\langle \left| \vec{n}\cdot\vec{\Omega}_{\mathrm{m}} \right| \vec{R}^{\top}(\vec{\Omega}_m)\vec{v}^-, \vec{R}(\vec{\Omega}_m)\overrightarrow{\Phi}^- \right\rangle_{\mathcal{F}}, \end{aligned} \tag{9.30}$$

9.3.5 Diffusion-diffusion coupling

Coupling between two diffusion schemes are favored in the case that scalar fluxes in contiguous subdomains are diffusive. Unlike high order couplings, the coupling between two diffusion schemes is rather to borrow the methodology developed for DFEM-diffusion that penalizes the jump of the scalar flux value and gradient[70]. The difference from DFEM-diffusion is that herein CFEM is still engaged to discretize the diffusion equation within each subdomain. We only apply the penalty method on the interface. We arbitrarily

choose one subdomain as the master subdomain and as always fix the normal vector $\vec{n}$ pointing from master to slave. Further, every quantity belonging to master/slave subdomain will be given a superscript "$\mp$". The definition of penalty coefficient is given by[70]:

$$\kappa = \max\left(p^-(p^-+1)\frac{D^-}{h^-} + p^+(p^++1)\frac{D^+}{h^+}, \frac{1}{4}\right), \tag{9.31}$$

where p is the polynomial order; D is diffusion coefficient, h is the length of the cell orthogonal to interface, which is defined as $h = \frac{2A}{L}$ where A is the element area and L is the element edge length on the interface. Thereafter, the interface bilinear form is formulated as:

$$I = \langle [\![v]\!], \kappa [\![\phi]\!] \rangle_{\mathcal{F}} + \langle \{D\partial_n v\}, [\![\phi]\!] \rangle_{\mathcal{F}} + \langle [\![v]\!], \{D\partial_n \phi\} \rangle_{\mathcal{F}}, \tag{9.32}$$

where $\partial_n \phi = \vec{n} \cdot \nabla \phi$.

9.4 Numerical Tests

Most numerical tests in this section are carried out with Rattlesnake the MOOSE based application, as a new realization of its multiscale functionality, which allows different angular schemes to couple in different subdomains divided from the whole domain[68, 69]. Part of the results for S_N-S_N method were obtained by implementation with the C++ open source finite element library deal.II[52].

Test results for S_N-S_N, P_N-P_N and S_N-P_N couplings will be presented.

Reed-like problem will be presented for all three schemes[54]. In the process of developing all the couplings, Reed-like problem was always used in tests and found to be extremely useful. As a multi-region heterogeneous problem, it easily triggered errors from the way we set up interfaces and splitted boundaries for different schemes. As a heterogeneous problem with nonsmooth solution, one could quickly tell if a developing

scheme/formulation is correct.

For S_N-P_N coupling, a eigenvalue problem named “poison problem" will be presented. Essentially, it is an 2D thick square pure absorber surrounded by thin fuel meat. Strong absorption makes CFEM-SAAF-S_N hard to have an accurate estimation of k_{eff} even with many layers of spatial refinements.

Also, a more realistic problem, i.e. the KAIST-3A 2D test problem will be presented for S_N-P_N calculation.

9.4.1 S_N-S_N

Reed’s problem

The first test is the Reed’s problem for S_N-S_N coupling as illustrated in Figure 9.1. S_{16} is used in the calculation. In the void, the void treatment is utilized so that conservation is preserved[66]. What is surprising is that in void, the flux profile is flat to round-off level, which means with void treatment, the subdomain-wise conservation is achieved. However, CFEM-SAAF-S_N with void treatment does not possess this property. In fact, with under-resolved mesh, CFEM-SAAF-S_N would present oscillations around the right interface in void. By detaching subdomains with different materials, the subdomain-wise particle causality is fixed.

Two-region test

The second test is a two-region absorber test as used in Section 8. Figure 9.2a presents the comparison of the flux profiles with 16 cells for both CFEM-SAAF-S_4 and CD-SAAF-S_4. With the additional DoFs on the interface, the scalar flux in the thin material is computed accurately while CFEM-SAAF’s result is highly distorted in the thin material. Figure 9.2b is the relative error of the leakage rate on the right side for different schemes. We also compared the least-squares method (LS) S_4 with the other two. Fixing up the causality not only brings accurate scalar flux profile in thin material, but also affects the

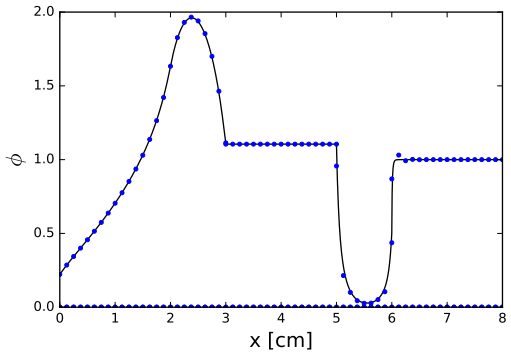

Figure 9.1: Reed's problem for S_N-S_N coupling

accuracy of boundary leakage.

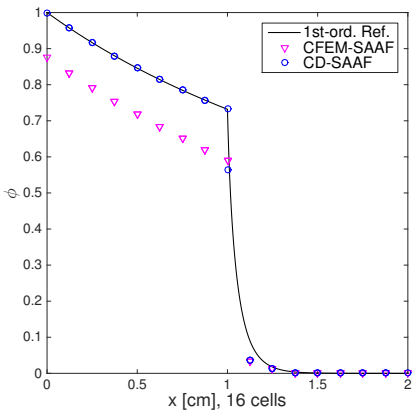

(a) Scalar flux profiles.

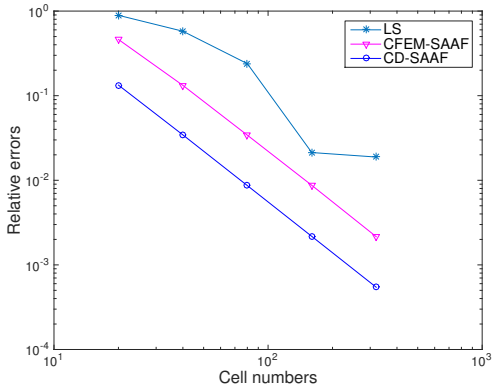

(b) Leakage rate errors on right side boundary.

Figure 9.2: Two-region absorber test for S_N-S_N coupling.

Iron-water shielding problem

Iron-water problem is re-used as an spatial accuracy demonstration for S_N-S_N. S_2 is used in angle. To make a reference, 1200x1200 cells are used for CFEM-SAAF-S_N. When measuring the absorption rate error in iron, we found both methods roughly have

second-order spatial convergence rates (see Figure 9.3). Yet, CD-SAAF delivers lower error magnitudes for all cell sizes as observed in the iron-water test for CDLS.

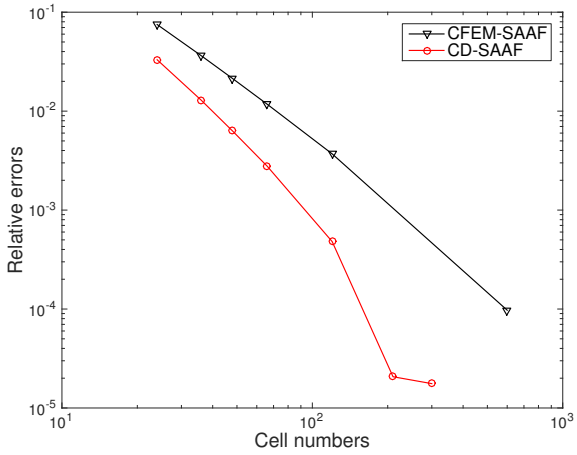

Figure 9.3: Error of absorption rates in iron vs cell numbers along one direction.

9.4.2 P_N-P_N

Modified Reed's problem

The modified Reed's problem in the rest of the report is such that in void, a thin absorber ($\sigma_t = 0.01$) is used instead. Mesh is refined enough such that all the errors we see in Figure 9.4 are reasoned to be mainly from angular discretization. The P_1-P_1 presents discontinuous solution on the interfaces. This seems to be the results of the scheme trying to better fit the flux shape without increasing angular space in subdomains. Instead, the solution is detached on the interfaces. The Roe solver ("CD-SAAF-P_N: Riemann" shown in the legends) presents similar discontinuous solution on interfaces. However, increasing angular order from P_1 to P_5, we observe the discontinuity on the interfaces tend to vanish and all schemes tend to be consistent.

If we check the error of integral flux at the spots where schemes differ most (i.e. $x \in$

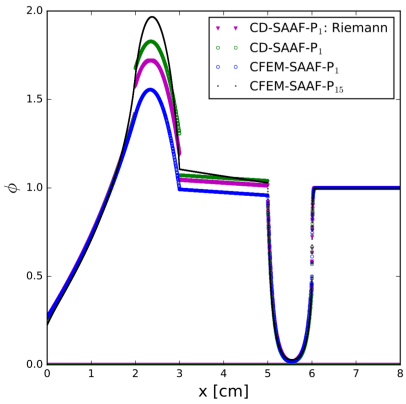

(a) CD-SAAF-P_1 with different upwindings.

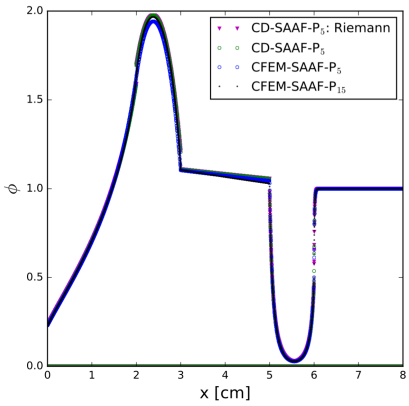

(b) CD-SAAF-P_5 with different upwindings.

Figure 9.4: Modified Reed's problem with different order P_N angular disretizations

$(2, 3)$ cm), we see the error magnitudes are lowered significantly based on the reference of S_{110} (see Figure 9.5). However, with increasing angular orders, all scheme errors go to zero.

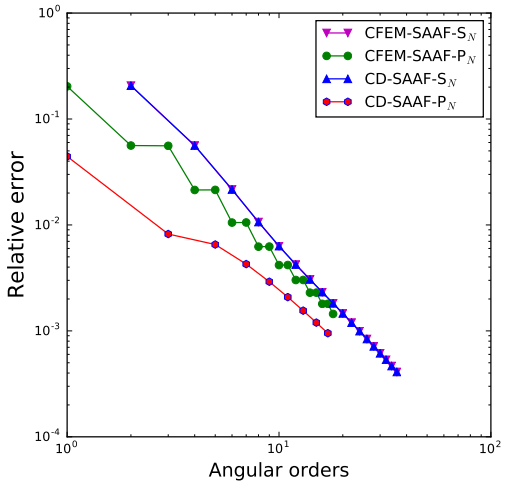

Figure 9.5: Modified Reed's problem absorption rate errors for multiple schemes for $x \in (2, 3)$ cm.

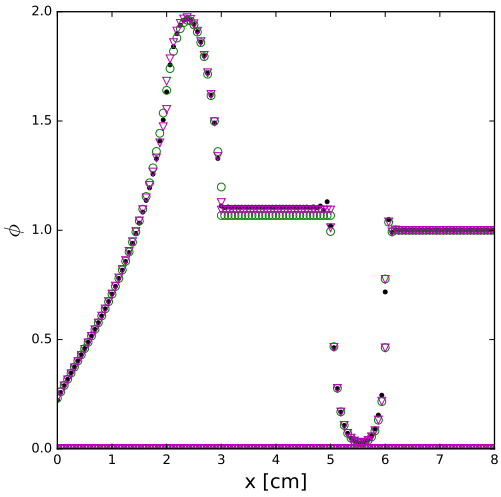

Figure 9.6: Reed's problem for S_N-P_N coupling

9.4.3 S_N-P_N

Reed's problem

Reed's problem is the first test used as a demonstration of S_N-P_N functionality. As seen in Figure 9.6, green dots are for the hybridation of S_{16} for $x \in (3, 6)$ cm and P_5 elsewhere. The hybridation presents an accurate scalar flux profile in most regions. However, the scalar flux level in void is lower than the reference, which is from the CFEM-SAAF-S_{16}. Apparently, high angular accuracy is required not only in void, but also in the subdomains contiguous to it in order to attain an accurate solution. Therefore, a relatively high order P_N, P_{13}, is placed as a buffer layer for $x \in (2, 3)$ cm between P_5 and S_{16}. The purple triangles are for the new solution. As expected, the solution in void is correct by introducing the "buffer".

Quasi-1D modified Reed's problem

As spherical harmonics is the only set of angular basis which is rotationally invariant, S_N with angular quadrature in multi-D would never be equivalent to P_N method. The

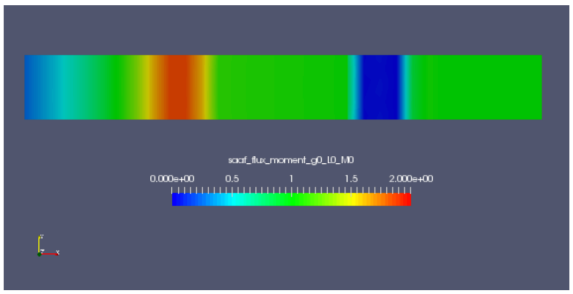

Figure 9.7: Quasi 1D modified Reed's problem for S_N-P_N coupling compared with mortar implementation of multiscale

discrepancy between these two method cause oscillations around coupling interface when coupling is realized by strongly enforcing angular flux continuity, as what mortar finite element delivers[68]. A further check beyond the 1D test is then necessary. Therefore, a modified Reed's problem is employed and extended to 2D. By making the upper and lower boundaries of a rectangular domain to be reflective, a 2D variation of modified Reed's problem is created. Along x axis, the setting is the same as 1D modified Reed's problem. Figure 9.7 presents the scalar flux for a hybrid scheme between P_3 ($x \in (3, 5)$ cm) and S_4 (elsewhere). Without angular smoothing around the coupling interfaces, which are necessary for mortar implementation of Rattlesnake multiscale capability, we still observe smooth solution in the domain. No obvious oscillation is seen around the interfaces.

Figure 9.8a is a line plot along axis for $y = 0.5$ cm. Mortar and CD-SAAF solutions are produced using 4x32 cells. The reference is made with CFEM-SAAF-S_4 with 2 more layers of uniform refinement. CD-SAAF agrees with mortar solution in most regions but has much higher accuracy in the thin absorber, where mortar solution is distorted a lot by thick materials around. A sanity check is also performed that lines along y axis around the S_N-P_N interfaces are drawn out in Figure 9.8b. Graphically, scalar flux is flat and no oscillation manifests around the interfaces.

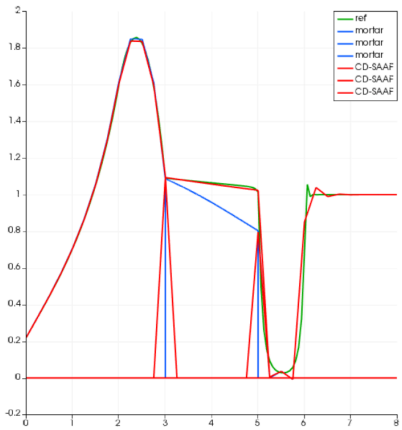

(a) Line plot for $y = 0.5$ cm.

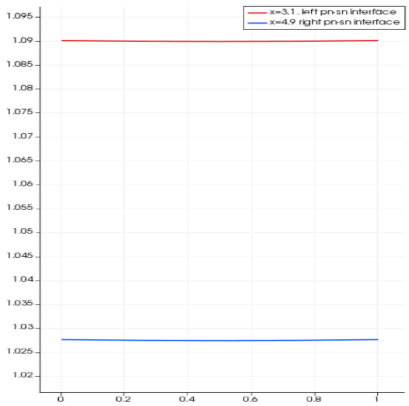

(b) Line plots along y direction around S_N-P_N interfaces.

Figure 9.8: Line plots for quasi 1D modified Reed's problem.

Poison problem

The "poison" problem is an eigenvalue problem characterized by a strong absorber in the middle of a 2D domain and thin fuel meat surrounding the poison. With the presence of the strong absorber, CFEM-SAAF-S_{16} needs a lot of refinement to get a converged k_{eff}. With 9 layers of uniform refinement[2], CFEM-SAAF-S_{16} gives a k_{eff} of 0.89880. We see slow convergence when increasing refinement layers in Table 9.1.

Table 9.1: k_{eff} results for CFEM-SAAF-S_{16} with different layers of uniform refinements.

Refinement layers	5	6	7	8	9
k_{eff}	0.89675	0.89723	0.89779	0.89856	0.89880

However, with setting an interface between the two materials, S_{16}-S_{16} gives 0.89878 (see Table 9.2) with merely five layers of uniform refinement. The trade off is the slight increase of DoFs from the interface.

[2]The total DoFs is over 150 million with CFEM-SAAF-S_{16}.

Table 9.2: k_{eff} results for SAAF-S_{16} in absorber coupled with different angular schemes in fuel meat, with 5 layers of uniform refinements.

Coupled schemes	S_{16}	P_1	P_2	P_3	P_4
k_{eff}	0.89878	0.89852	0.89882	0.89879	0.89879
Coupled schemes	P_5	P_6	P_7	P_8	P_9
k_{eff}	0.89879	0.89879	0.89879	0.89879	0.89879

Table 9.3: KAIST-3A group structure.

Group number	Energy ranges [eV]
0	$1.353 \times 10^6 - 2 \times 10^7$
1	$9.119 \times 10^3 - 1.353 \times 10^6$
2	$3.928 - 9.119 \times 10^3$
3	$0.6251 - 3.928$
4	$0.1457 - 0.6251$
5	$0.05692 - 0.1457$
6	$0 - 0.05692$

More importantly, with using P_N schemes in fuel instead, we gain comparable k_{eff} value with merely P_2 in the fuel, which is a big saving in sense of total DoFs. This is the whole purpose of developing S_N-P_N coupling that we aim to gain reasonable accuracy with small amount of DoFs.

2D KAIST-3A test

Last but not least, the 2D KAIST3A small full-core PWR problem[71], is used as a real-world test. The configuration and initial meshing (i.e. without any spatial refinement) are shown in Figures 9.9a and 9.9b, respectively. The group structure is listed in Table 9.3. Different orders of P_N are assigned to the reflector (dark green), while S_8 are used otherwise. The main purpose is to show coupling low order P_N with high order S_N would not sacrifice the accuracy.

Table 9.4 listed a comparison between S_8-P_N with three layers of uniform refinements.

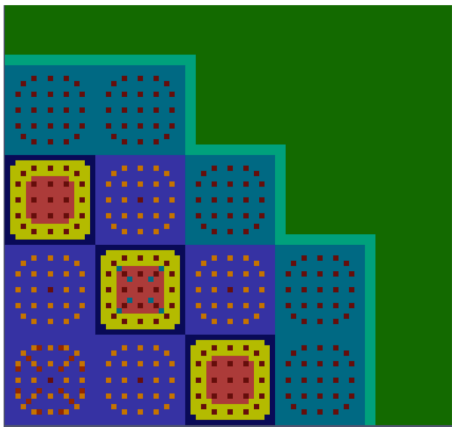

(a) Configuration of 2D KAIST-3A problem.

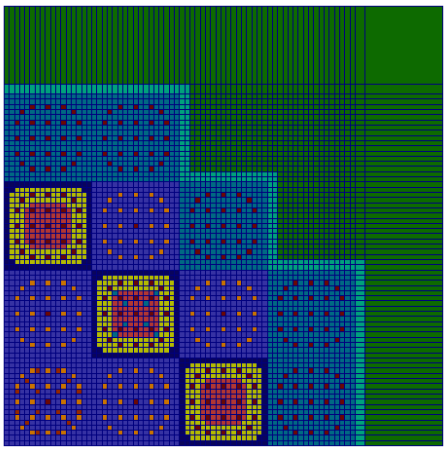

(b) KAIST-3A problem starting mesh.

Figure 9.9: KAIST-3A geometry and meshing.

Table 9.4: k_{eff} comparisons between CD-SAAF-S_8-P_N and CFEM-SAAF-S_8 with 3 layers of uniform refinements. The reference k_{eff} from CFEM-SAAF-S_8 with 4 layers of uniform refinements is 0.96877.

Schemes	S_8	S_8-P_1	S_8-P_3	S_8-P_5	S_8-P_7
k_{eff}	0.96858	0.96843	0.96860	0.96859	0.96859
$k_{\text{eff}} - k_{\text{ref}}$ [pcm]	-19	-34	-17	-18	-18

A reference solution is from CFEM-SAAF-S_8 with 4 layers of uniform refinements[3].

Figures 9.10 and 9.11 present comparisons between S_8 and S_8-P_1 for fast and thermal groups, respectively. With using P_1 in reflector, the maximum thermal scalar flux differs from CFEM-SAAF-S_8 by less then 0.1%. What is more important, as demonstrated in the quasi-1D modified Reed's problem, no instability is induced around the interface between high order S_8 and the low order P_1. By increasing the P_N order from 1 to 3, the k_{eff} is comparably accurate as CFEM-SAAF-S_8 with the same layers of refinements.

[3]The reference scalar fluxes for all groups from CFEM-SAAF-S_8 with 4 layers of uniform refinements are presented in Appendix C.

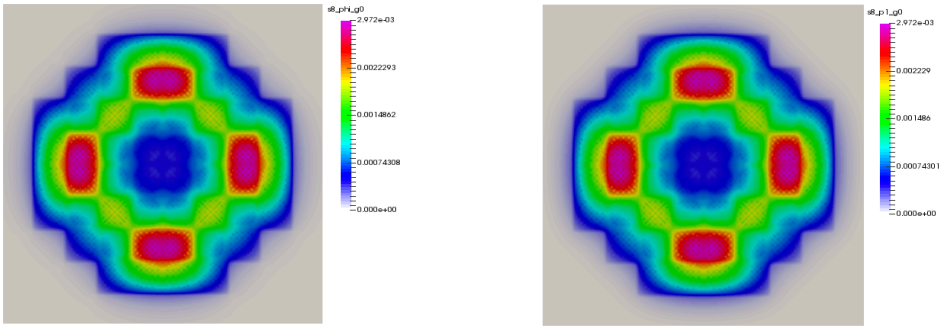

(a) CFEM-SAAF-S_8. (b) CD-SAAF-S_8-P_1.

Figure 9.10: Comparison for fast fluxes (g=0).

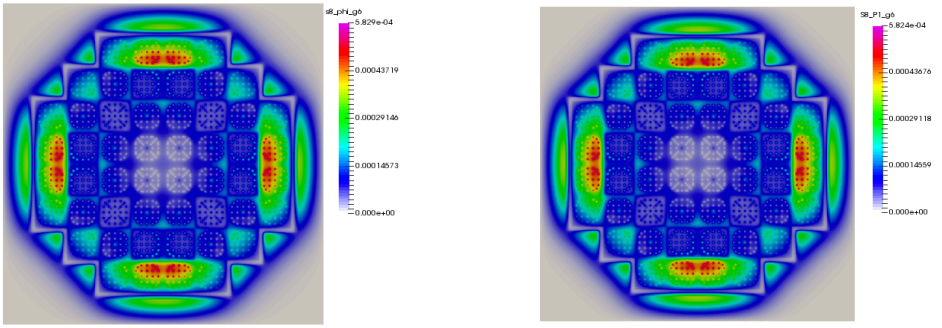

(a) CFEM-SAAF-S_8. (b) CD-SAAF-S_8-P_1.

Figure 9.11: Comparison for thermal fluxes (g=6).

10. CONCLUSIONS AND RECOMMENDATIONS

10.1 Concluding Remarks

10.1.1 Nonlinear filtering with residual indicated viscosity

By analyzing the least-squares residual in moment variable space, we developed a nonlinear transient P_N closure. The TP_N closure essentially is a modified diffusive closure with flux limiters added to the total cross section. Testing with 1D problems shows plausible accuracy. In 2D applications, however, TP_N shows to be sensitive to the coefficients. But it does provide a nonlinear viscosity which we applied to the nonlinear filtered P_N method in this dissertation.

10.1.2 Nonlinear filtered P_N methods

We applied the viscosity realized in development of TP_N method to the filtered P_N method. Unlike the TP_N method, NFP_N shows the robustness in a wide range of multi-D test problems for time-dependent linear transport.

We also developed another NFP_N formulation in which the viscosity shares a similar form of the viscosity in Larsen's flux limited diffusion. For both forms, we gave a proof for the asymptotic preservations. We further provide a fully implicit scheme for TRT applications. Tests on the Marshak problem demonstrated the method efficacies and numerically proves that both formulations preserve the thick diffusion limit.

10.1.3 Relaxed L_1 method for solving neutron transport in near-void situations

We have provided a nonlinear relaxed L_1 method solving neutron transport equation effectively accurately in void and near-void situations. By defining a L_1 norm of transport residual in finite element space, we derived a L_1 finite element method. Besides, to be compatible with the L_1 method, we derived a L_1 boundary condition. The resulting

method delivers effectively non-oscillatory results in void and near-void problems where least-squares can produce oscillations and negativity. Also, we showed the consistent RL_1 boundary condition is necessary to obtain reasonable results on the incident boundary.

10.1.4 Contiguous discontinuous finite element methods for solving neutronics

CDLS method

By breaking the regular least-squares method into subdomain-wise definitions where within each subdomain total cross section is nonzero constant. We provided a proof for the obtainment of subdomain-wise and global conservation in heterogeneous system. The developed interface condition fixed the non-conservative issue existing in ordinary least-squares methods. In an iron-water shielding problem, it shows a second order spatial convergence but with much lower error magnitude compared with CFEM-LSTE and CFEM-SAAF. Overall, the CDLS method is very promising for non-void neutron transport calculations.

CD-SAAF method

We also applied the CD methodology to the $1/\sigma_{\mathrm{t}}$- weighted least-squares finite element and through a lengthy derivation, we found the resemblance to CFEM-SAAF within each subdomain and a upwinding flux on the interfaces. Thusly, we call the resulting method “CD-SAAF". We naturally exploited the discontinuity by applying different angular discretization schemes on different sides of an interface. It turns out for k-eigenvalue calculations, such S_N-P_N coupling scheme can deliver comparable accuracy with CFEM-SAAF-S_N while using much less degrees of freedom. And the scheme has been implemented in the MOOSE based application Rattlesnake in INL[69].

10.2 Recommendations

10.2.1 NFP$_N$ formulations

The NFP$_N$ formulations developed in this work are successful in the sense of inferring part of the viscosity nonlinearly based on the solution. Nevertheless, there are two issues remain. The first one is a principle to find a proper c_N. We found that c_N is rather problem-dependent. Further, larger c_N would always ensure the simulation running yet adding inappropriately large angular diffusion. An attractive direction for for future exploration is then find a solution dependent method to determine c_N such that c_N will be tuned automatically as well as ν_l.

10.2.2 Efficient solving technique for RL$_1$ method

Despite the easily understandable formulation of RL$_1$, the solving efficiency is not ideal. On the other hand, though one might derive a Newton-like algorithm for solving in L$_1$ norm, correctly formulating the Jacobian would be quite complex, exhausting and of poor understandability. Part of the reason for the solving inefficiency is that the nonlinear iteration is executed only when the linear iteration is converged. One possibility to overcome the shortcoming is to use Jacobian-free Newton Krylov method (JFNK)[72]. In such a case, the source iteration solving is evolved with the nonlinear solve, without explicitly giving the Jacobian, which is necessary for Newton's method.

10.2.3 Conservative treatment for CDLS in void

In void, as proved by Section 8, CDLS is not globally conservative. In near void situation, though CDLS is conservative, it is not clear if the σ_{t} weighted interface condition is appropriate in the sense of not degrading the preconditioning and linear solving process. An appropriate treatment in void and near-void is then necessary.

10.2.4 Efficient k-eigenvalue calculations with CDLS in highly heterogeneous problems

CDLS is of value due to the preservation of conservation and high accuracy. However, difficulty arises from implementation perspective. In order to have conservation preserved, constant cross sections within each subdomain is requested. In real-world reactor calculations, such a setting can be troublesome. Without homogenization, every single material within a fuel pin requests an individual subdomain. Even with homogenization, one still have to cautiously set up subdomains. An example is the KAIST-3A test that one needs at least 10 individual subdomains with the presence of 10 different homogenized pins. Effects of using less subdomains needs further research.

10.2.5 Acceleration techniques for CD-SAAF k-eigenvalue calculations

For large-scale full-core calculations, acceleration techniques like nonlinear diffusion acceleration (NDA) is necessary to speed up convergence for k-eigenvalue calculations[58]. For CD-SAAF, since discontinuity is only imposed on predefined interfaces, it might be not proper to use CFEM-NDA. Implementation of consistent NDA is necessary but supposed to be relatively trivial in Rattlesnake since coupling between diffusion has been successfully developed.

REFERENCES

[1] W. Zheng and R. G. McClarren, "Moment closures based on minimizing the residual of the {PN} angular expansion in radiation transport," Journal of Computational Physics, vol. 314, pp. 682 – 699, 2016.

[2] J. E. Morel and J. M. McGhee, "A Hybrid Collocation-Galerkin-SN method for Solving the Boltzmann Transport Equation," Nuclear Science and Engineering, vol. 101, no. 1, pp. 72–87, 1999.

[3] J. C. Stone, Adaptive Discrete-Ordinates Algorithms and Strategies. PhD thesis, Texas A&M University, 2007.

[4] T. A. Brunner, "Forms of Approximate Radiation Transport," Tech. Rep. SAND2002-1778, Sandia National Laboratory, 2002.

[5] T. A. Brunner and J. P. Holloway, "Two-dimensional time dependent Riemann solvers for neutron transport," Journal of Computational Physics, vol. 210, no. 1, pp. 386 – 399, 2005.

[6] T. A. Brunner, Riemann Solvers for Time-Dependent Transport based on the Maximum Entropy and Spherical Harmonics Closures. PhD thesis, University of Michigan, 2000.

[7] R. G. McClarren, Spherical Harmonics Method for Thermal Radiation Transport. PhD thesis, University of Michigan, 2007.

[8] R. G. McClarren and R. B. Lowrie, "The effects of slope limiting on asymptotic-preserving numerical methods for hyperbolic conservation laws," Journal of Computational Physics, vol. 227, no. 23, pp. 9711 – 9726, 2008.

[9] R. McClarren, J. P. Holloway, T. Brunner, and T. Mehlhorn, "Implicit riemann solvers for the pn equations," in Computational Methods in Transport, pp. 457–467, Springer Berlin Heidelberg, 2006.

[10] R. G. McClarren, J. P. Holloway, and T. A. Brunner, "A p1 benchmark for time dependent thermal radiative transfer," Tech. Rep. LA-UR-07-1203, Los Alamos National Laboratory (LANL), 2007.

[11] R. G. McClarren, J. P. Holloway, T. A. Brunner, and T. A. Mehlhorn, "A quasilinear implicit riemann solver for the time-dependent p n equations," Nuclear science and engineering, vol. 155, no. 2, pp. 290–299, 2007.

[12] R. G. McClarren, J. P. Holloway, and T. A. Brunner, "On solutions to the p n equations for thermal radiative transfer," Journal of Computational Physics, vol. 227, no. 5, pp. 2864–2885, 2008.

[13] T. A. Brunner, R. McClarren, and J. P. Holloway, "Establishing an asymptotic diffusion limit for riemann solvers on the time-dependent pn equations," Tech. Rep. SAND2005-0947C, Sandia National Laboratories, 2005.

[14] C. D. Hauck and R. G. McClarren SIAM J. Sci. Comput, vol. 32, no. 5, pp. 2603–2626, 2010.

[15] C. D. Hauck, "High-order entropy-based closures for linear transport in slab geometry," Commun. Math. Sci, vol. 9, no. 1, pp. 187–205, 2011.

[16] T. A. Brunner and J. P. Holloway, "One-Dimensional Riemann Solvers and the Maximum Entropy Closure," Journal of Quantitative Spectroscopy& Radiative Transfer, vol. 69, pp. 543–566, 2001.

[17] R. G. McClarren and C. D. Hauck, "Simulating radiative transfer with filtered spherical harmonics," Physics Letters A, vol. 374, no. 22, pp. 2290 – 2296, 2010.

[18] V. M. Laboure, R. G. McClarren, and C. D. Hauck, "Implicit filtered {PN} for high-energy density thermal radiation transport using discontinuous galerkin finite elements," Journal of Computational Physics, vol. 321, pp. 624 – 643, 2016.

[19] V. M. Laboure, Improved Fully-Implicit Spherical Harmonics Methods for First and Second Order Forms of the Transport Equation using Galerkin Finite Element. PhD thesis, Texas A&M University, 2016.

[20] M. Frank, C. D. Hauck, and K. Küpper, "Diffusion, P_1, and other approximate forms of radiation transport," Communication in Mathematical Sciences, vol. 14, no. 5, pp. 1443–1465, 2016.

[21] D. Radice, E. Abdikamalov, L. Rezzolla, and C. D. Ott, "A new spherical harmonics scheme for multi-dimensional radiation transport i. static matter configurations," Journal of Computational Physics, vol. 242, pp. 648 – 669, 2013.

[22] G. L. Olson, "Spherical Harmonic Solutions of the Radiation Transport Equation Using Angle-dependent Artificial Scattering to Decrease Oscillations," Tech. Rep. LA-UR-12-22927, Los Alamos National Laboratory, Los Alamos, NM, 2012.

[23] C. J. Gesh, Finite Element Methods for Second Order Forms of the Transport Equation. PhD thesis, Texas A&M University, 1999.

[24] C. J. Gesh and M. L. Adams, "Finite Element Solutions of Second-order Forms of the Transport Equation at the Interface Between Diffusive and Non-Diffusive Regions," in M&C 2001, 2001. Salt Lake City, Utah, United States.

[25] J. E. Morel, "A Self-Adjoint Angular Flux Equation," Nuclear Science and Engineering, vol. 132, no. 3, pp. 312–325, 1989.

[26] J. Hansen, J. Peterson, J. Morel, J. E. Ragusa, and Y. Wang, "A Least-Squares Transport Equation Compatible with Voids," Journal of Computational and Theoretical

Transport, vol. 43, pp. 374–401, Feb. 2015.

[27] P. G. Maginot, J. E. Morel, and J. C. Ragusa, "A non-negative moment-preserving spatial discretization scheme for the linearized boltzmann transport equation in 1-d and 2-d cartesian geometries," Journal of Computational Physics, vol. 231, no. 20, pp. 6801 – 6826, 2012.

[28] "Non-oscillatory and non-diffusive solution of convection problems by the iteratively reweighted least-square finite element method," Journal of Computational Physics, vol. 105, pp. 108 – 121, 1993.

[29] W. Zheng and R. G. McClarren, "On Variable Selection and Effective Estimations of Interactive and Quadratic Sensitivity Coefficients: A Collection of Regularized Regression Techniques," in M&C2015, 2015. Nashville, TN, United States.

[30] J. L. Guermond, "A finite element technique for solving first order pdes in l_p," SIAM J. Numer. Anal, vol. 42, no. 2, pp. 714–737, 2004.

[31] W. Zheng and R. G. McClarren, "Emulation-Based Calibration for Parameters in Parameterized Phonon Spectrum of ZrHx in TRIGA Reactor Simulations," Nuclear science and engineering, vol. 183, no. 1, pp. 78–95, 2016.

[32] W. Zheng and R. G. McClarren, "Physics-Based Uncertainty Quantification for ZrHx Thermal Scattering Law," in ANS Winter Meeting 2013, vol. 109, pp. 743–745.

[33] W. Zheng, "Physics-based uncertainty quantification for zrhx thermal scattering law," Master's thesis, Texas A&M University, December 2013.

[34] W. Zheng and R. G. McClarren, "Effective Physics-Based Uncertainty Quantification for ZrHx Thermal Neutron Scattering in TRIGA Reactors," in PHYSOR 2014 International Conference, vol. 109, pp. 743–745.

[35] G. I. Bell and S. Glasstone, Nuclear Reactor Theory. Princeton, NJ: Krieger Pub Co, 3rd ed., 1985.

[36] W. Zheng and R. G. McClarren, "Semi-analytic benchmark for multi-group free-gas legendre moments and the application of gauss quadrature in generating thermal scattering legendre moments," Annals of Nuclear Energy, vol. 85, pp. 1131 – 1140, 2015.

[37] R. E. MacFarlane and D. W. Muir, "The NJOY Nuclear Data Processing System Version 91," Tech. Rep. LA-12740-M, Los Alamos National Laboratory, 1994.

[38] R. E. MacFarlane, D. W. Muir, R. M. Boicourt, and A. C. Kahler, "The NJOY Nuclear Data Processing System, Version 2012," Tech. Rep. LA-UR-12-27079, Los Alamos National Laboratory, 2012.

[39] Y. Azmy and E. Sartori, Nuclear Reactor Physics. Palookaville, USA: Spinger, 2nd ed., 2007.

[40] W. M. Stacey, Nuclear Computational Science: A Centry in Review. New York, USA: Wiley-VCH Verlag GmbH & Co. KGaA, 2010.

[41] J. E. Morel, B. T. Adams, T. Noh, J. M. McGhee, T. M. Evans, and T. J. Urbatsch, "Spatial discretizations for self-adjoint forms of the radiative transfer equations," Journal of Computational Physics, vol. 214, no. 1, pp. 12 – 40, 2006.

[42] Ya. B. Zeldovich and Yu. P. Raizer, Physics of shock waves and high-temperature hydrodynamic phenomena. New York, USA: Academic Press, 1966.

[43] C. D. Hauck and R. G. McClarren, "A Collision-Based Hybrid Method for Time-Dependent, Linear, Kinetic Transport Equations," MULTISCALE MODEL. SIMUL., vol. 11, no. 4, pp. 1197–1227, 2013.

[44] T. A. Brunner and J. P. Holloway, "One-dimensional Riemann solvers and the maximum entropy closure," Journal of Quantitative Spectroscopy and Radiative Transfer, vol. 69, no. 5, pp. 543 – 566, 2001.

[45] M. Schäfer, M. Frank, and C. D. Levermore, "Diffusive Corrections to PN Approximations," Multiscale Modeling & Simulation, vol. 9, no. 1, pp. 1–28, 2011.

[46] K. S. Oh and J. P. Holloway, "A Quasi-static Closure for 3rd Order Spherical Harmonics Time-Dependent Radiation Transport in 2-D," in M& C 2009, 2009.

[47] J. E. Morel, "Diffusion-limit asymptotics of the transport equation, the $P_{1/3}$ equations, and two flux-limited diffusion theories," Journal of Quantitative Spectroscopy and Radiative Transfer, vol. 65, no. 5, pp. 769–778, 2000.

[48] R. G. McClarren and T. K. Lane, "A Flux-Limited Diffusion Method for Simulating Radiative Shocks," in ANS Winter Meeting 2012, vol. 107, pp. 557–559, ANS, 2012. San Diego, CA, November.

[49] C. K. Garrett and C. D. Hauck, "A Comparison of Moment Closures for Linear Kinetic Transport Equations: The Line Source Benchmark," Transport Theory and Statistical Physics, vol. 42, no. 6-7, pp. 203–235, 2013.

[50] B. Cockburn and C.-W. Shu, "The Local Discontinuous Galerkin finite element method for convection-diffusion systems," SIAM J. Numer. Anal., vol. 35, pp. 2440–2463, 1998.

[51] MATLAB, version 7.10.0 (R2010a). Natick, Massachusetts: The MathWorks Inc., 2010.

[52] W. Bangerth, T. Heister, L. Heltai, G. Kanschat, M. Kronbichler, M. Maier, B. Turcksin, and T. D. Young, "The `deal.II` library, version 8.2," Archive of Numerical Software, vol. 3, 2015.

[53] B. D. Ganapol, R. S. Baker, J. A. Dahl, and R. E. Alcouffe, "Homogeneous infinite media time-dependent analytical benchmarks," Tech. Rep. LA-UR–01-1854, Los Alamos National Laboratory, 2001.

[54] W. Reed, "New difference schemes for the neutron transport equation," Nucl. Sci. Eng. 46: No. 2, 309-14, 1971.

[55] R. G. McClarren, "Theoretical Aspects of the Simplified P_n Equations," Transport Theory and Statistical Physics, vol. 39, no. 2-4, pp. 73–109, 2011.

[56] C. Ahrens and S. Merton, "An Improved Filtered Spherical Harmonic Method for Transport Calculations," in M& C 2013, 2013.

[57] Y. Zhang, Even-parity S_N Adjoint Method Including SP_N Model Error and Iterative Efficiency. PhD thesis, Texas A&M University, 2014.

[58] J. R. Peterson, H. R. Hammer, J. E. Morel, J. C. Ragusa, and Y. Wang, "Conservative Nonlinear Diffusion Acceleration Applied to the Unweighted Least-squares Transport Equation in MOOSE," in M&C2015, 2015. Nashville, TN, United States.

[59] W. Zheng and R. G. McClarren, "Non-oscillatory Reweighted Least Square Finite Element Method for S_N Transport," in ANS Winter Meeting 2015, vol. 113, pp. 688–691.

[60] W. Zheng and R. G. McClarren, "Non-oscillatory Reweighted Least Square Finite Element for Solving P_N Transport," in ANS Winter Meeting 2015, vol. 113, pp. 692–695.

[61] P. Maginot, J. Morel, and R. J. E.an, "A positive non-linear closure for the sn equations with linear-discontinous spatial differencing," 2009. Saratoga Springs, New York, United States.

[62] "On the numerical solution of conservation laws by minimizing residuals," Journal of Computational Physics, vol. 113, no. 2, pp. 304 – 308, 1994.

[63] R. E. Alcouffe, "Diffusion Synthetic Acceleration Methods for Diamond-Differenced Discrete-Ordinates Equations," Nuclear Science and Engineering, vol. 64, pp. 344–355, 1977.

[64] R. T. Ackroyd, J. G. Issa, and N. S. Rivait, "Treatment of Voids in Finite Element Transport Methods," Prog. Nucl. Energy, vol. 1 and 2, pp. 85–89, 1986.

[65] C. Drumm, "Spherical harmonics (pn) methods in the sceptre radiation transport code," in M&C 2015, 2015. Nashville, TN, United States.

[66] Y. Wang, H. Zhang, and R. C. Martineau, "Diffusion Acceleration Schemes for Self-Adjoint Angular Flux Formulation with a Void Treatment," Nuclear Science and Engineering, vol. 176, no. 2, pp. 201–225, 2014.

[67] C. L. Castrianni and M. L. Adams, "A Nonlinear Corner-Balance Spatial Discretization for Transport on Arbitrary Grids," Nuclear Science and Engineering, vol. 128, no. 3, pp. 278–296, 1998.

[68] S. Schunert, Y. Wang, M. D. DeHart, and R. C. Martineau, "Hybrid P_N-S_N Calculations with SAAF for the Multiscale Transport Capability in Rattlesnake," in PHYSOR 2016.

[69] Y. Wang, S. Schunert, M. DeHart, R. Matineau, and W. Zheng, "Hybrid P_N-S_N With Lagrange Multiplier and Upwinding for the Multiscale Transport Capability in Rattlesnake," Progress in Nuclear Energy, 2016. submitted on Sep.

[70] Y. Wang, Adaptive Mesh Refinement SOlution Techniques for the Multigroup S_N Transport Equation Using a Higher-order Discontinuous Finite Element Method. PhD thesis, Texas A&M University, 2009.

[71] N. Z. Cho, "Benchmark Problem 3A: MOX Fuel-Loaded Small PWR Core (MOX Fuel with Zoning) (7 Group Homogenized Cells)." http://nurapt.kaist.ac.kr/benchmark/kaist_ben3a.pdf. Accessed: 2016-10-08.

[72] "Jacobian-free newtonkrylov methods: a survey of approaches and applications," Journal of Computational Physics, vol. 193, no. 2, pp. 357 – 397, 2004.

[73] P. Roe, "Approximate riemann solvers, parameter vectors, and difference schemes," Journal of Computational Physics, vol. 43, no. 2, pp. 357 – 372, 1981.

APPENDIX A

DISCONTINUOUS FINITE ELEMENT DISCRETIZATION FOR P_N EQUATIONS

A.1 P_N angular discretization

The spherical harmonics expansion is expressed as:

$$\psi(\vec{\Omega}) = \sum_{l \leq N, m} \phi_l^m Y_l^m(\vec{\Omega}) \tag{A.1}$$

For DFEM-P_N, orthonormal spherical harmonics are used, namely:

$$\int_{4\pi} d\Omega \; \bar{Y}_{l'}^{m'}(\vec{\Omega}) Y_l^m(\vec{\Omega}) = \delta_{ll'}\delta_{mm'} \tag{A.2}$$

The spherical harmonics can be either complex or real-valued.

Introduce the truncated P_N expansion and perform the integration $\int_{4\pi} d\Omega \; \bar{Y}_l^m(\vec{\Omega})(\cdot)$ to the transport equation[1], one would gain

$$\frac{1}{c}\frac{\partial \vec{\phi}}{\partial t} + \sum_{\chi=x,y,z} \nabla_\chi \mathbf{A}_\chi \vec{\phi} + (\mathbf{\Sigma}_\mathrm{t} - \mathbf{S})\,\vec{\phi} = \vec{Q}, \tag{A.3}$$

where

$$\mathbf{A}_\chi = \int_{4\pi} d\Omega \; \vec{e}_\chi \cdot \vec{\Omega} \vec{Y} \vec{Y}^\top, \quad \vec{Y} = \left(Y_0^0, \cdots, Y_N^N\right)^\top \tag{A.4}$$

$$\vec{Q} = \left(\frac{Q}{\sqrt{4\pi}}, 0, \cdots, 0\right)^\top \tag{A.5}$$

[1] $\bar{Y}_l^m$ represents the conjugate spherical harmonics

$$\mathbf{\Sigma}_{\mathrm{t}} = \mathrm{diag}(\sigma_{\mathrm{t}}, \sigma_{\mathrm{t}}\mathbf{I}_{\mathrm{b}_1}, \cdots, \sigma_{\mathrm{t}}\mathbf{I}_{\mathrm{b}_N}), \tag{A.6}$$

$$\mathbf{S} = \mathrm{diag}(\sigma_0, \sigma_1\mathbf{I}_{\mathrm{b}_1}, \cdots, \sigma_{\mathrm{t}} - \sigma_N\mathbf{I}_{\mathrm{b}_N}), \tag{A.7}$$

and $\mathbf{I}_{\mathrm{b_i}}$ represents identity matrix for the block of $l = \mathrm{i}$. Eq. (A.7) can be easily proved by utilizing Eq. (2.36). For 3D calculations, there are $(N+1)(N+2)$ moments. For 2D calculations, by dropping the y-axis dependence, all the moments are real and there are only $(N+1)(N+2)/2$ relevant moments[6].

A.1.1 Complex-valued form

The complex-valued spherical harmonics[35, 7, 5, 6] is expressed as

$$Y_l^m(\vec{\Omega}) = (-1)^m \sqrt{\frac{2l+1}{4\pi}\frac{(l-m)!}{(l+m)!}} P_l^m(\mu) e^{im\mu} \tag{A.8}$$

where the associated Legendre polynomial P_l^m is defined as:

$$P_l^m(\mu) = \begin{cases} \frac{(1-\mu^2)^{m/2}}{2^l l!}\frac{d^{l+m}}{d\mu^{l+m}}(\mu^2-1)^l, & 0 \le m \le l \\ P_l^m = \frac{(l-|m|)!}{(l+|m|)!}P_l^{|m|}, & -l \le m < 0 \end{cases} \tag{A.9}$$

Testing the transport equation with $\bar{y}_l^m$, we approach the 3D complex-valued P_N equations:

$$\begin{aligned} &\frac{1}{c}\frac{\partial \phi_l^m}{\partial t} + \frac{1}{2}\frac{\partial}{\partial x}\left(-C_{l-1}^{m-1}\phi_{l-1}^{m-1} + D_{l+1}^{m-1}\phi_{l+1}^{m-1} + E_{l-1}^{m+1}\phi_{l-1}^{m+1} - F_{l+1}^{m+1}\phi_{l+1}^{m+1}\right) \\ &+ \frac{1}{2}i\frac{\partial}{\partial y}\left(C_{l-1}^{m-1}\phi_{l-1}^{m-1} - D_{l+1}^{m-1}\phi_{l+1}^{m-1} + E_{l-1}^{m+1}\phi_{l-1}^{m+1} - F_{l+1}^{m+1}\phi_{l+1}^{m+1}\right) \\ &+ \frac{\partial}{\partial z}\left(A_{l-1}^m\phi_{l-1}^m + B_{l+1}^m\phi_{l+1}^m\right) + \sigma_{\mathrm{t}}\phi_l^m = \sigma_{\mathrm{s}}\phi_0^0\delta_{l0}\delta_{m0} + \frac{Q}{\sqrt{4\pi}} \end{aligned} \tag{A.10}$$

$$
\begin{aligned}
A_l^m &= \frac{(l-m+1)(l+m+1)}{(2l+3)(2l+1)} \qquad & B_l^m &\frac{(l-m)(l+m)}{(2l+1)(2l-1)} \\
C_l^m &= \frac{(l+m+1)(l+m+2)}{(2l+3)(2l+1)} \qquad & D_l^m &\frac{(l-m)(l-m-1)}{(2l+1)(2l-1)} \\
E_l^m &= \frac{(l-m+1)(l-m+2)}{(2l+3)(2l+1)} \qquad & F_l^m &\frac{(l+m)(l+m-1)}{(2l+1)(2l-1)}
\end{aligned} \tag{A.11}
$$

In 2D calculations, by dropping the y-axis dependence and recognizing all the imaginary parts of the moments are zero, we can have the equations for $m \neq 0$:

$$
\begin{aligned}
&\frac{1}{c}\frac{\partial \phi_l^m}{\partial t} + \frac{1}{2}\frac{\partial}{\partial x}\left(-C_{l-1}^{m-1}\phi_{l-1}^{m-1} + D_{l+1}^{m-1}\phi_{l+1}^{m-1} + E_{l-1}^{m+1}\phi_{l-1}^{m+1} - F_{l+1}^{m+1}\phi_{l+1}^{m+1}\right) \\
&+ \frac{\partial}{\partial z}\left(A_{l-1}^m\phi_{l-1}^m + B_{l+1}^m\phi_{l+1}^m\right) + \sigma_{\mathrm{t}}\phi_l^m = 0,
\end{aligned} \tag{A.12}
$$

and the equation for $m = 0$:

$$
\begin{aligned}
&\frac{1}{c}\frac{\partial \phi_l^0}{\partial t} + \frac{\partial}{\partial x}\left(E_{l-1}^1\phi_{l-1}^1 - F_{l+1}^1\phi_{l+1}^1\right) \\
&+ \frac{\partial}{\partial z}\left(A_{l-1}^0\phi_{l-1}^0 + B_{l+1}^0\phi_{l+1}^0\right) + \sigma_{\mathrm{t}}\phi_l^0 = \sigma_{\mathrm{s}}\phi_0^0\delta_{l0} + \frac{Q}{\sqrt{4\pi}}\delta_{l0}.
\end{aligned} \tag{A.13}
$$

A.1.2 Real-valued form

By defining the constant $\mathcal{C}_l^m = \sqrt{\frac{2l+1}{4\pi}\frac{(l-m)!}{(l+m)!}}$

$$
Y_l^m(\vec{\Omega}) = \begin{cases}
\sqrt{2}\mathcal{C}_l^m P_l^m(\mu)\cos(m\varphi), & 0 < m \leq l \leq N \\
\mathcal{C}_l^0 P_l^0(\mu), & 0 \leq l \leq N, \quad m = 0 \\
\sqrt{2}\mathcal{C}_l^{|m|} P_l^{|m|}(\mu)\sin(|m|\varphi), & 0 < -m \leq l \leq N,
\end{cases} \tag{A.14}
$$

one could either perform analytic integration to get the coefficients in Eq. (A.3) as in Section A.1.1 (see [20] for details), or construct an angular quadrature to accurately integrate as described in [21].

A.2 Weak Formulation

Discretizing P_N equation with DFEM leads to a weak form composed as the following: finding $\vec{\phi} \in \mathcal{V}$, such that $\forall \vec{v} \in \mathcal{V}$, the following holds

$$a(\vec{v}, \vec{\phi}) = a^{\text{vol}}(\vec{v}, \vec{\phi}) + a^{\text{edge}}(\vec{v}, \vec{\phi}) + a^{\text{boundary}}(\vec{v}, \vec{\phi}) = 0 \tag{A.15}$$

A.2.1 Volumetric weak forms

$$a^{\text{vol}}(\vec{v}, \vec{\phi}) = \int_{\mathcal{D}} d\vec{r} \left(-\sum_{\chi} \nabla_{\chi} \vec{v}^{\top} \mathbf{A}_{\chi} \vec{\phi} + \vec{v}^{\top} \left(\mathbf{\Sigma}_{\text{t}} - \mathbf{S} \right) \vec{\phi} - \vec{v}^{\top} \vec{Q} \right) \tag{A.16}$$

A.2.2 Interior edge weak form using Riemann solver

When assembling the edge weak forms, we visit once per edge. The interface flux is specified with upwinding flux. Thereby:

$$a^{\text{edge}}(\vec{v}, \vec{\phi}) = \sum_{\mathcal{E} \in \mathcal{F}_{\text{int}}} \sum_{\chi} \int_{\mathcal{E}} ds \ |\vec{e}_{\chi} \cdot \vec{n}| \left[\!\left[\vec{v}^{\top} \right]\!\right] \left(\mathbf{A}_{\chi} \left\{ \vec{\phi} \right\} + \frac{|\mathcal{A}_{\chi}|}{2} \left[\!\left[\vec{\phi} \right]\!\right] \right), \tag{A.17}$$

where

$$\left[\!\left[\vec{\phi} \right]\!\right] = \vec{\phi}^{+} - \vec{\phi}^{-} \quad \text{and} \quad \left\{ \vec{\phi} \right\} = \frac{\vec{\phi}^{+} + \vec{\phi}^{-}}{2} \tag{A.18}$$

and $\vec{\phi}^{\pm}$ are the upwind/downwind fluxes[2]. $|\mathcal{A}_{\chi}|$ is the dissipation matrix prescribed by the eigenstructure of streaming matrix $\mathbf{A}_{\chi}$. There are two typical ways of formulating the dissipation matrix. One is to use Roe matrix[73], which solve exactly for the Riemann

[2]Note the upwinding definition is the ad hoc definition, differing from those in Section 9 with the same notations.

problem of P_N[7, 6]. However, Roe matrix is complex and not sparse, degrading the implicit solves. Alternatively, a Lax-Fridrichs numerical flux, which is a diagonal matrix with the maximum eigenvalue of $\mathbf{A}_\chi$ can be used. In fact, as the maximum eigenvalues of $\mathbf{A}_\chi$ for all P_N orders have the limit of 1, an identity matrix is used in this dissertation as suggested in [18].

A.2.3 Boundary weak form with ghost cells

Ghost cell[7, 5, 6, 46] formulation is used to impose incident boundary condition. By assuming the boundary information is isotropic over the whole 4π solid angle, one could then calculate the boundary moments in a straightforward way:

$$\vec{\phi}_{\mathrm{b}} = \left(\sqrt{4\pi}\psi^{\mathrm{inc}}, 0, \cdots, 0\right) \tag{A.19}$$

Therefore, the weak form can be specified by splitting boundary into two types. One type is exterior boundary is on the upwind side, i.e. $\vec{e}_\chi \cdot \vec{n} < 0$ and the other wind is exterior boundary on the downwind side, i.e. $\vec{e}_\chi \cdot \vec{n} < 0$. Thereby, the weak form writes as:

$$\begin{aligned} a^{\mathrm{boundary}}(\vec{v}, \vec{\phi}) = \sum_{\chi} \int_{\partial\mathcal{D}} ds \Bigg(& - \sum_{\vec{e}_\chi \cdot \vec{n} > 0} \frac{|\vec{e}_\chi \cdot \vec{n}|}{2} \vec{v}^\top \left(\mathbf{A}_\chi \left(\vec{\phi}_{\mathrm{b}} + \vec{\phi} \right) + |\mathcal{A}_\chi| \left(\vec{\phi}_{\mathrm{b}} - \vec{\phi} \right) \right) \\ & + \sum_{\vec{e}_\chi \cdot \vec{n} < 0} \frac{|\vec{e}_\chi \cdot \vec{n}|}{2} \vec{v}^\top \left(\mathbf{A}_\chi \left(\vec{\phi}_{\mathrm{b}} + \vec{\phi} \right) + |\mathcal{A}_\chi| \left(\vec{\phi} - \vec{\phi}_{\mathrm{b}} \right) \right) \Bigg) \end{aligned} \tag{A.20}$$

Though the ghost cells some inaccurately presumes isotropy on boundary condition, the Riemann solver adjust the amount of information necessary to transmit into the interior so it is still accurate. In case more legit boundary condition is desired, [18] presents a Marshak boundary condition and can be used instead.

APPENDIX B

P_N ANGULAR DISCRETIZATION OF SELF-ADJOINT ANGULAR FLUX EQUATION

B.1 Introduction

Due to the fact SAAF-P_N is engaged in Section 9, we introduce the SAAF-P_N angular scheme combined with CFEM formulation. Note that SAAF-P_N involved in this work is the source-iteration compatible form of SAAF. When solving this form of SAAF with P_N, the system is not symmetric positive definite. However, compared with the other form of SAAF, this form avoid the singularity in pure scatterer.

Different from the spherical harmonics introduced in APPENDIX A, the spherical harmonics in this appendix is orthogonal but non-orthonormal, following the convention of Rattlesnake[68, 69]. However, it possesses the property that the corresponding zeroth moment is equal to scalar flux without any scaling.

The final aim of this appendix is to provide brief but clear way of constituting the SAAF-P_N formulation.

B.2 Weak Formulation

B.2.1 Non-orthonormal P_N Expansion

Since the zeroth moment is different from the one from using orthonormal spherical harmonics, we use capital case of ϕ_l^m to represent the moment from using non-orthonormal spherical harmonics. Denote the non-orthonormal spherical harmonics by $R_l^m(\vec{\Omega})$, then relationship to real-valued orthonormal basis is:

$$R_l^m(\vec{\Omega}) = \frac{1}{\sqrt{4\pi}} Y_l^m(\vec{\Omega}) \tag{B.1}$$

Then the P_N projected angular flux can be reconstructed as:

$$\psi(\vec{\Omega}) = \sum_{l \leq N, m} R_l^m(\vec{\Omega}) lm \Phi_l^m, \tag{B.2}$$

Differing from Appendix A, here we attain the following equity:

$$\Phi_0^0 = \phi. \tag{B.3}$$

We further let $\vec{R}(\vec{\Omega}) = \left(R_0^0(\vec{\Omega}), \cdots, R_N^N(\vec{\Omega})\right)$, then Eq. (B.2) can be rewritten as:

$$\psi(\vec{\Omega}) = \vec{R}^\top(\vec{\Omega})\vec{\Phi} \tag{B.4}$$

B.2.2 P_N projection

Let us re-arrange the integration in Eq. (6.15) as:

$$\begin{aligned}
&\int_{\mathcal{D}} d\vec{r} \int_{4\pi} d\Omega \left(\vec{\Omega} \cdot \nabla v \frac{\vec{\Omega} \cdot \nabla \psi - \mathcal{S}\psi}{\sigma_{\mathrm{t}}} + v\left(\sigma_{\mathrm{t}}\psi - \mathcal{S}\psi\right)\right) + \int_{\partial\mathcal{D}} ds \int_{\vec{n}\cdot\vec{\Omega}>0} d\Omega\, \vec{n}\cdot\vec{\Omega} v\psi \\
&= \int_{\mathcal{D}} d\vec{r} \int_{4\pi} d\Omega \left(v\frac{Q}{4\pi} + \vec{\Omega}\cdot\nabla v \frac{Q}{4\pi\sigma_{\mathrm{t}}}\right) + \int_{\partial\mathcal{D}} ds \int_{\vec{n}\cdot\vec{\Omega}<0} d\Omega \left|\vec{n}\cdot\vec{\Omega}\right| v\psi^{\mathrm{inc}}
\end{aligned} \tag{B.5}$$

Before proceeding, we will define the diagonal normalization matrix:

$$\mathbf{N} = \int_{4\pi} d\Omega\, \vec{R}(\vec{\Omega})\vec{R}^\top(\vec{\Omega}) = \frac{1}{4\pi}\mathbf{I} \tag{B.6}$$

where $\mathbf{I}$ is an identity matrix. Introduce the P_N expansion to v and ψ, we will be able to transform the weak form to the following formulation: find $\phi \in \mathcal{V}$ such that $\forall v \in \mathcal{V}$ the

following equation holds:

$$\int_{\mathcal{D}} d\vec{r}\ \left(\sum_{\chi}\sum_{\gamma} \nabla_{\chi}\vec{v}^{\top}\frac{1}{\sigma_{\mathrm{t}}}\mathbf{T}_{\chi,\gamma}\nabla_{\gamma}\vec{\Phi} + \vec{v}^{\top}\left(\mathbf{\Sigma}_{\mathrm{t}} - \mathbf{S}\right)\mathbf{N}\vec{\Phi} - \sum_{\chi}\nabla_{\chi}\vec{v}^{\top}\mathbf{N}\mathbf{A}_{\chi}\frac{1}{\sigma_{\mathrm{t}}}\mathbf{S}\vec{\Phi}\right) \tag{B.7}$$
$$+ \int_{\partial\mathcal{D}} ds\ \vec{v}^{\top}\mathbf{L}^{+}\vec{\Phi} = \int_{\mathcal{D}} d\vec{r}\ \left(\vec{v}^{\top}\vec{\mathcal{Q}} + \sum_{\chi}\nabla_{\chi}\vec{v}^{\top}\frac{1}{\sigma_{\mathrm{t}}}\mathbf{A}_{\chi}\vec{\mathcal{Q}}\right) + \int_{\partial\mathcal{D}} ds\ \vec{v}^{\top}\vec{\mathcal{J}}_{\mathrm{inc}},$$

where

$$\mathbf{T}_{\chi,\gamma} = \int_{4\pi} d\Omega\ \Omega_{\chi}\Omega_{\gamma}\vec{R}(\vec{\Omega})\vec{R}^{\top}(\vec{\Omega}), \quad \chi,\gamma = x,y,z, \tag{B.8a}$$

$$\vec{\mathcal{Q}} = \int_{4\pi} d\Omega\ \vec{R}(\vec{\Omega})\frac{Q}{4\pi}, \tag{B.8b}$$

$$\mathbf{L}^{+} = \int_{\vec{n}\cdot\vec{\Omega}>0} d\Omega\ \left|\vec{n}\cdot\vec{\Omega}\right| \vec{R}(\vec{\Omega})\vec{R}^{\top}(\vec{\Omega}), \tag{B.8c}$$

$$\vec{\mathcal{J}}_{\mathrm{inc}} = \int_{\vec{n}\cdot\vec{\Omega}<0} d\Omega\ \left|\vec{n}\cdot\vec{\Omega}\right| \vec{R}(\vec{\Omega})\psi^{\mathrm{inc}}(\vec{\Omega}). \tag{B.8d}$$

Angular integrals in Eq. (B.8) can be accurately obtained by using angular quadratures.

APPENDIX C

KAIST-3A REFERENCE SOLUTION WITH 4 UNIFORM REFINEMENTS

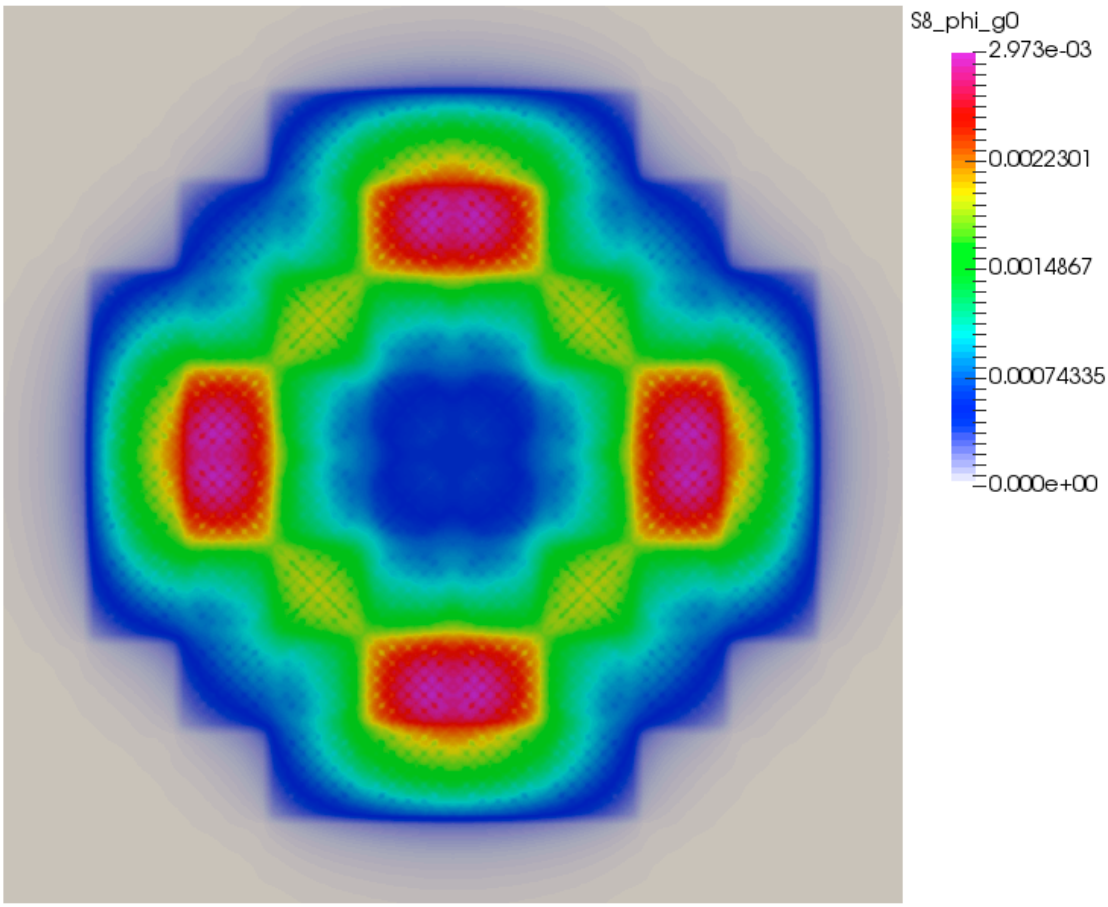

Figure C.1: ϕ for the zeroth group.

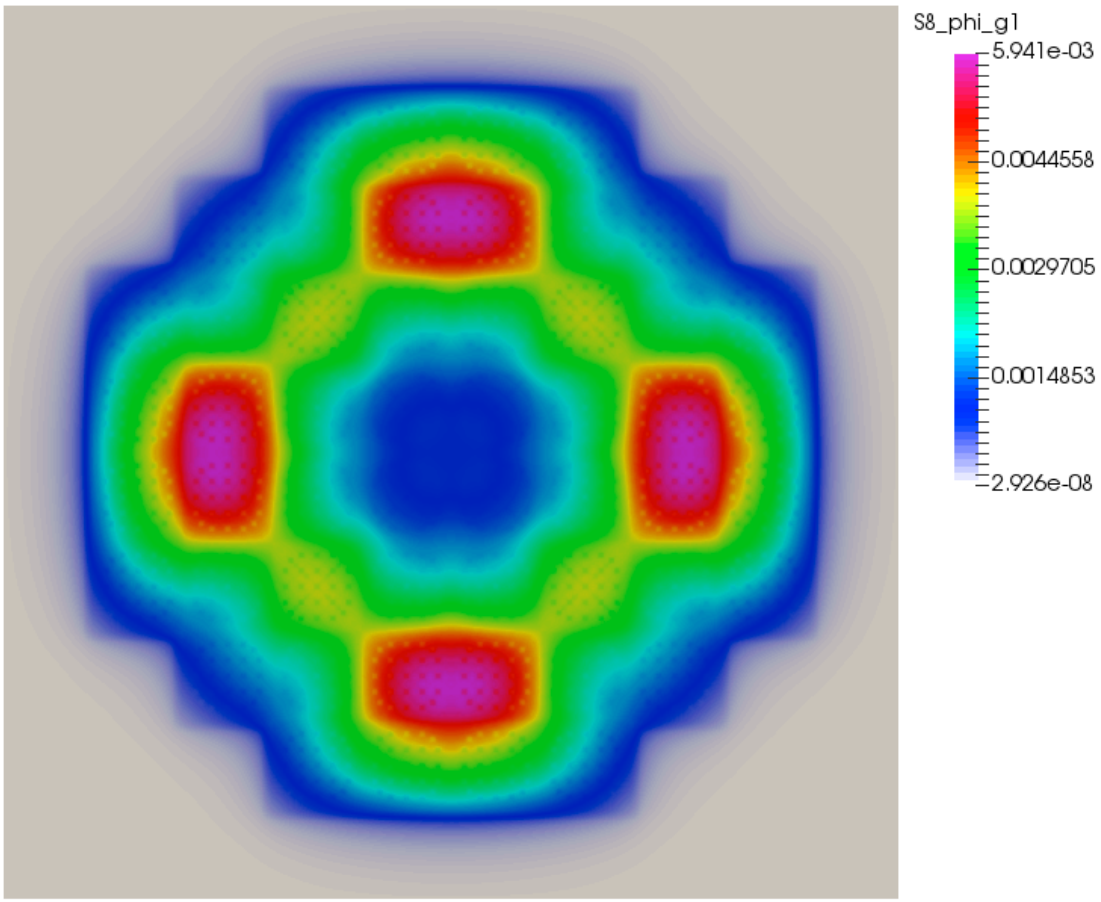

Figure C.2: ϕ for the first group.

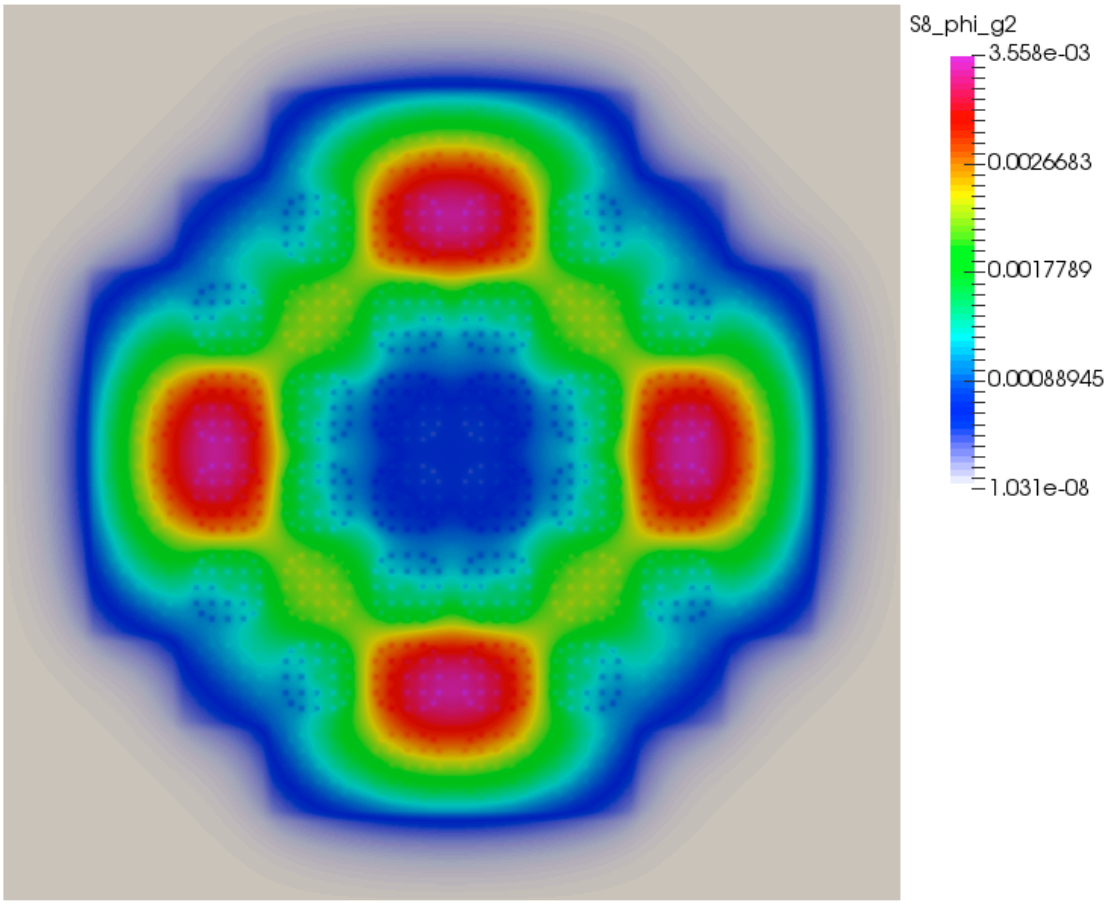

Figure C.3: ϕ for the second group.

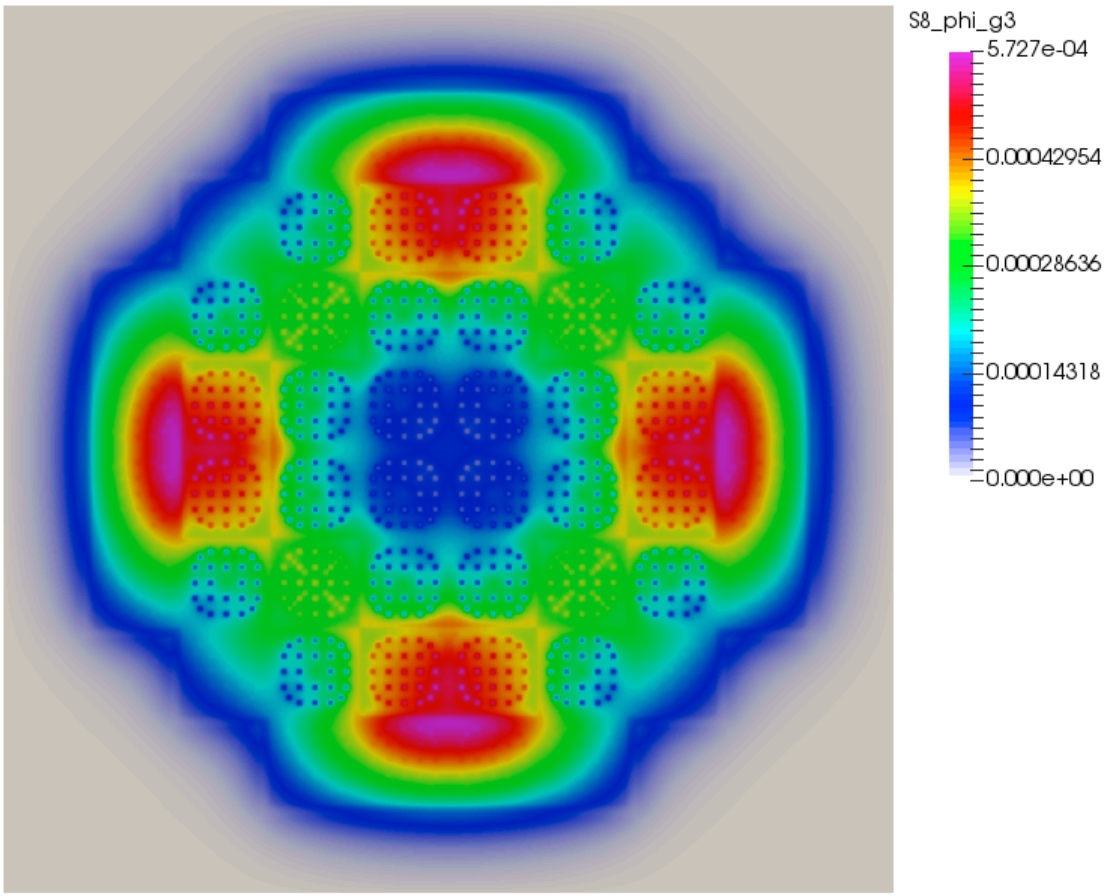

Figure C.4: ϕ for the third group.

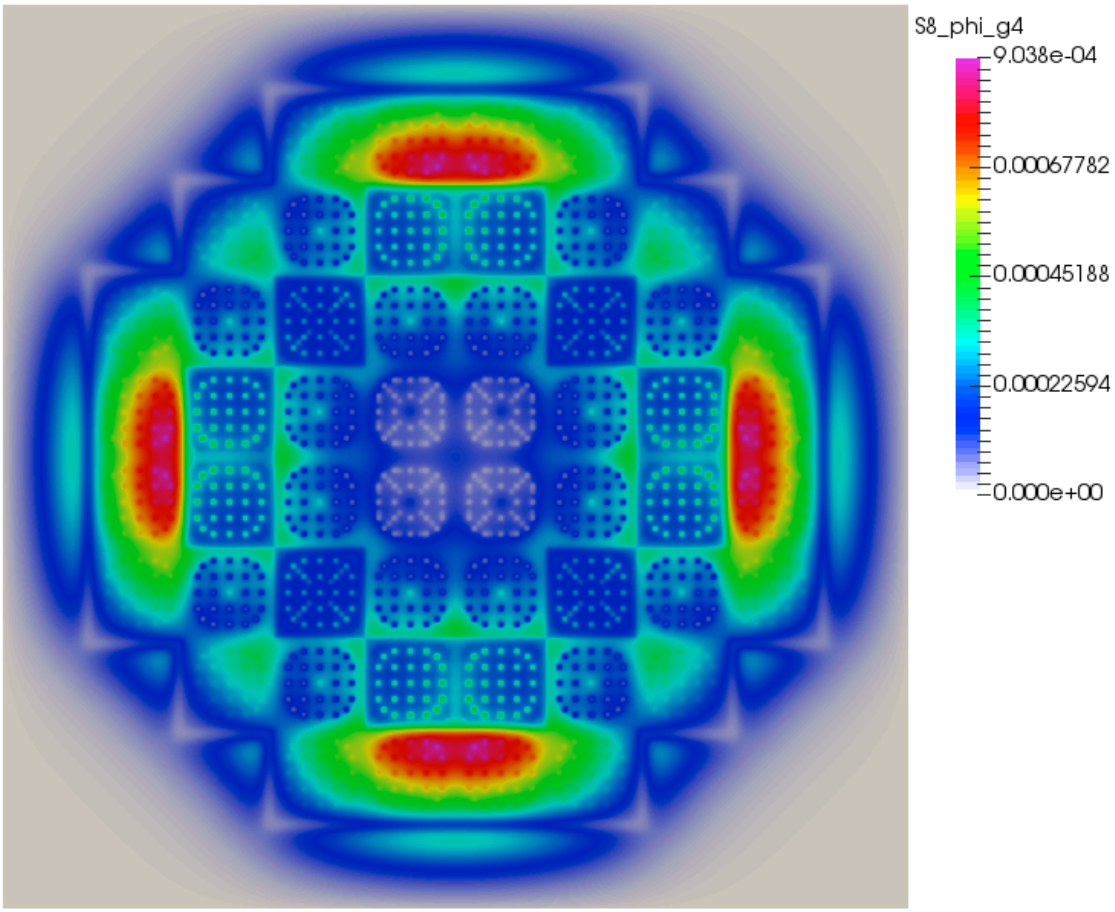

Figure C.5: ϕ for the fourth group.

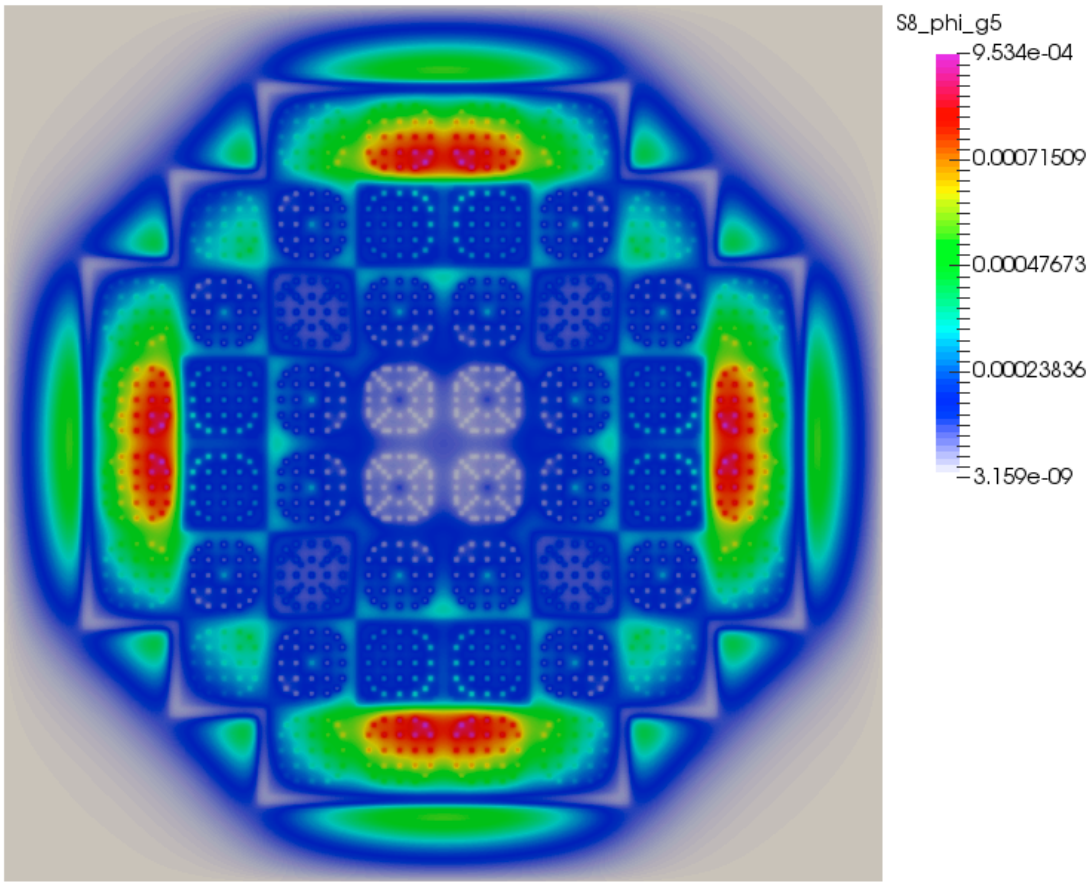

Figure C.6: ϕ for the fifth group.

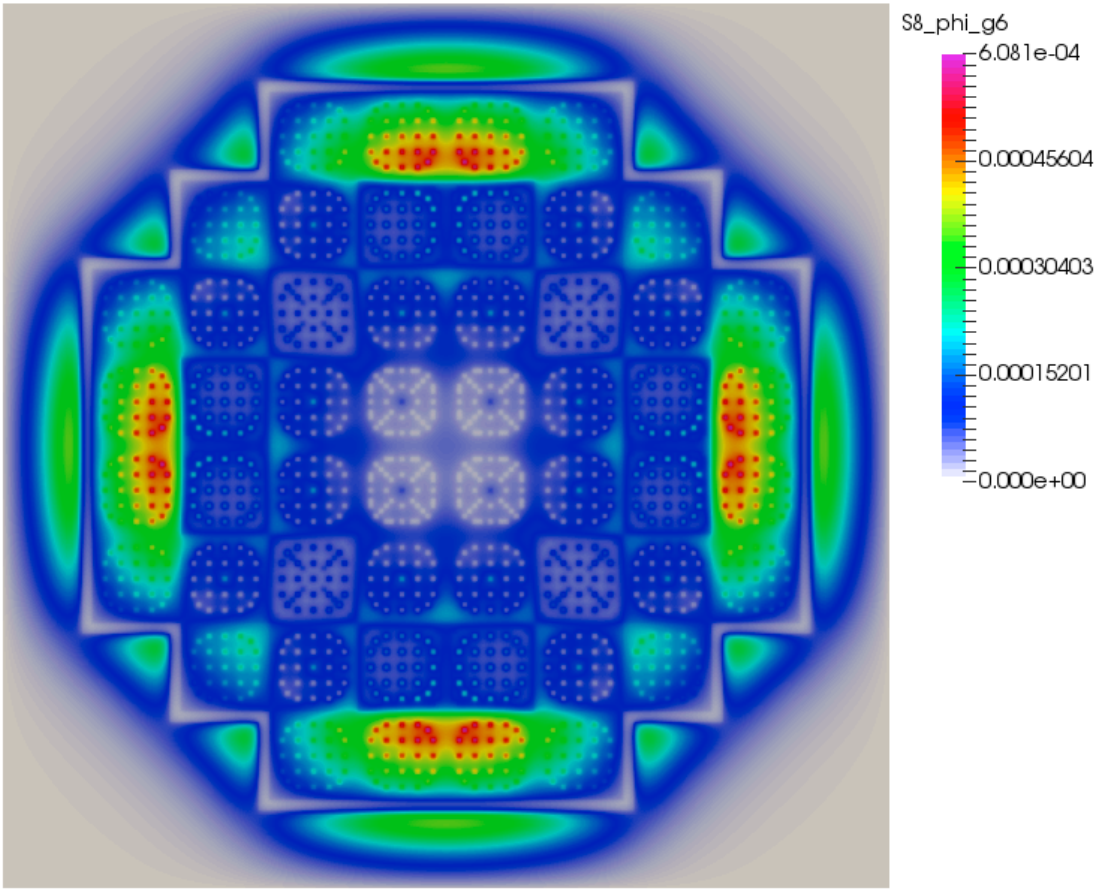

Figure C.7: ϕ for the sixth group.

APPENDIX D

CHECKERBOARD ERROR PLOTS

D.1 Checkerboard problem solution errors at $t = 3.2$ s

Based on S_{50} reference, we plot the errors in Figure D.1 from multiple methods presented in Section 4. It can be seen that while being accurate in the source region, S_N solutions present noticeably large errors in away from the source. Yet, besides the negativities, P_N presents relatively large errors around the central source region. NFP_N, on the other hand, decrease the P_N error around the source region while attains comparable accuracy with P_N away from the source.

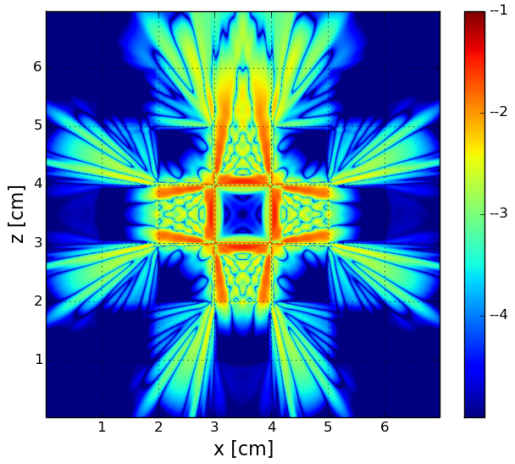

(a) S_8 vs. S_{50}

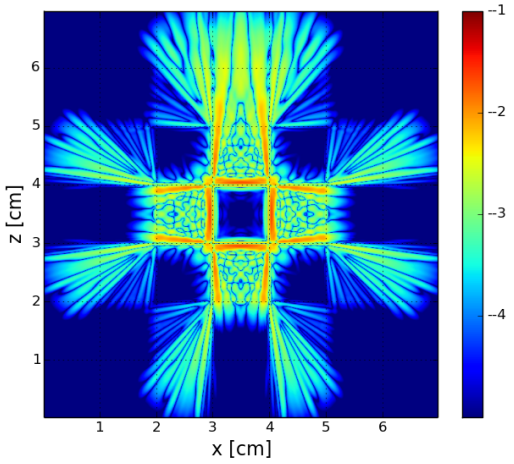

(b) S_{12} vs. S_{50}

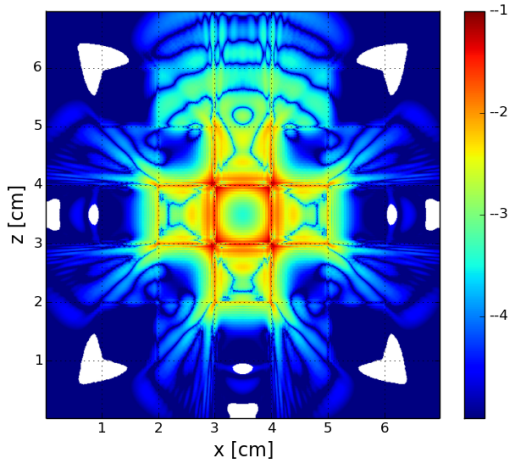

(c) P_7 vs. S_{50}

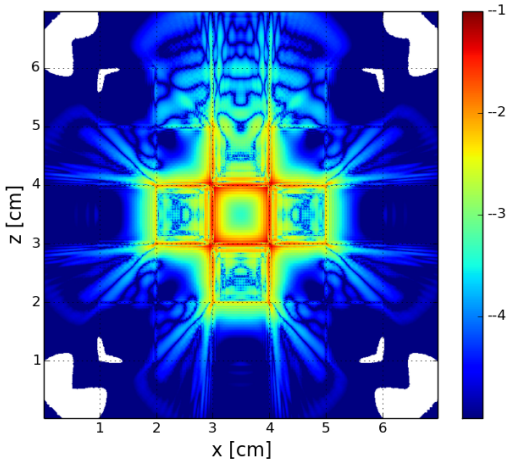

(d) P_{11} vs. S_{50}

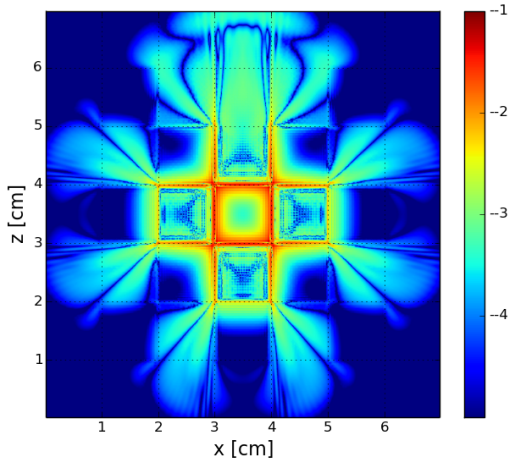

(e) NFP_7 vs. S_{50}

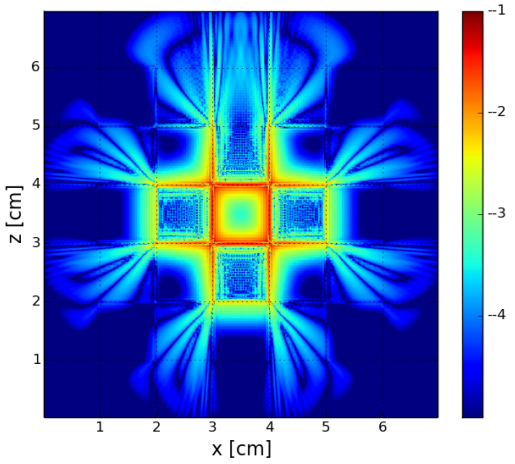

(f) NFP_{11} vs. S_{50}

Figure D.1: Solution errors based on S_{50} reference at $t = 3.2$ s.

APPENDIX E

SIMPLIFIED HOHLRAUM PROBLEM

E.1 NFP_{17} line-out plots

This section presents line-out plots for NFP_{17} in simplified Hohlraum problem.

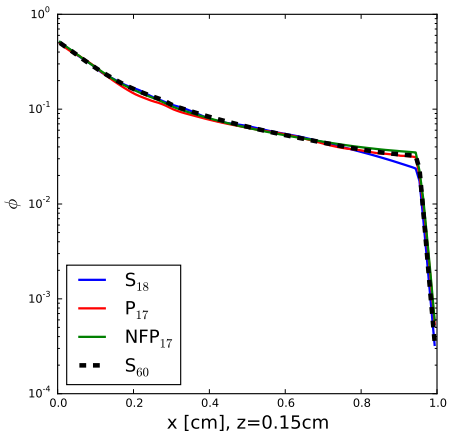

(a) Solutions along $z = 0.15$ cm

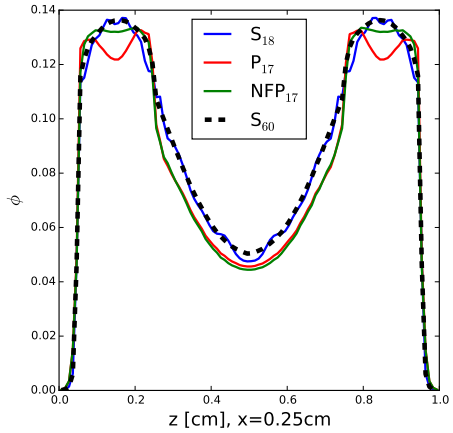

(b) Solutions along $x = 0.25$ cm

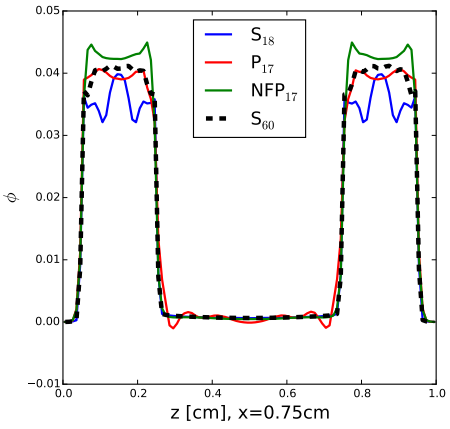

(c) Solutions along $x = 0.75$ cm

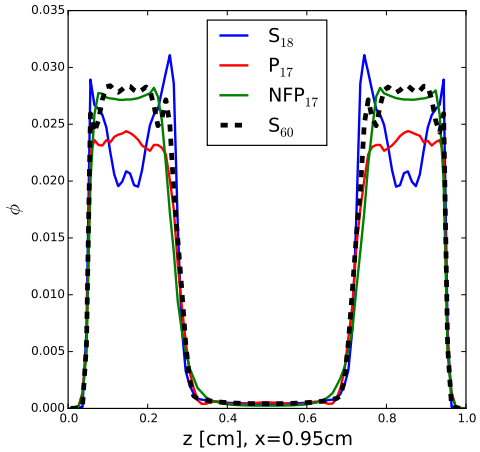

(d) Solutions along $x = 0.95$ cm

Figure E.1: Line-out plots for Hohlraum problem.